



**HAL**  
open science

# Design of a MEMS microphone based on a new device architecture

Samer Dagher

► **To cite this version:**

Samer Dagher. Design of a MEMS microphone based on a new device architecture. Acoustics [physics.class-ph]. Le Mans Université, 2020. English. NNT : 2020LEMA1028 . tel-04757483

**HAL Id: tel-04757483**

**<https://theses.hal.science/tel-04757483v1>**

Submitted on 29 Oct 2024

**HAL** is a multi-disciplinary open access archive for the deposit and dissemination of scientific research documents, whether they are published or not. The documents may come from teaching and research institutions in France or abroad, or from public or private research centers.

L'archive ouverte pluridisciplinaire **HAL**, est destinée au dépôt et à la diffusion de documents scientifiques de niveau recherche, publiés ou non, émanant des établissements d'enseignement et de recherche français ou étrangers, des laboratoires publics ou privés.

# Thèse de doctorat de

LE MANS UNIVERSITE  
Comue Université Bretagne Loire

ECOLE DOCTORALE N° 602  
Sciences pour l'Ingénieur  
Spécialité : Acoustique

Par

**Samer DAGHER**

**Design of a MEMS microphone based on a new device architecture**

Thèse présentée et soutenue au Mans, le 27 Octobre 2020

Unité de recherche : LAUM UMR CNRS 6613 et CEA Leti

Thèse N° : 2020LEMA1028

## Rapporteurs avant soutenance :

Thérèse LEBLOIS      Professeur, Université de Bourgogne Franche-Comté  
Dominique CERTON    Professeur, Université de Tours

## Composition du Jury :

*Attention, en cas d'absence d'un des membres du Jury le jour de la soutenance, la composition du jury doit être revue pour s'assurer qu'elle est conforme et devra être répercutée sur la couverture de thèse*

Président :	Skandar BASROUR	Professeur, Université Grenoble Alpes
Examineurs :	Thérèse LEBLOIS	Professeur, Université de Bourgogne Franche-Comté
	Dominique CERTON	Professeur, Université de Tours
	Cécile GUIANVARC'H	Maître de conférence, <i>HDR</i> , CNAM Paris
Dir. de thèse :	Stéphane DURAND	Maître de conférence, <i>HDR</i> , Université du Mans

## Invité(s)

Loïc JOET      Ingénieur de recherche, CEA



# Table of Contents

<b>TABLE OF CONTENTS</b> .....	I
<b>ABSTRACT</b> .....	III
<b>CHAPTER 1 INTRODUCTION</b> .....	1
<b>1.1. On the origins of MEMS microphones</b> .....	1
<b>1.2. Market and trends</b> .....	3
<b>1.3. State of the art</b> .....	5
1.3.1. Capacitive MEMS microphones .....	5
1.3.2. Piezoelectric MEMS microphones .....	12
<b>1.4. Next generation MEMS microphones</b> .....	18
1.4.1. Dual-Membrane Vacuum microphones.....	18
1.4.2. Air-to-Vacuum Transmission Microphone.....	19
<b>CHAPTER 2 MICROPHONE MODELING</b> .....	21
<b>2.1. Air-to-vacuum transmission mechanism</b> .....	21
2.1.1 Hinge Robustness .....	22
2.1.2. Hinge stiffness.....	26
<b>2.2. Microphone model</b> .....	32
2.2.1. Electrostatic transduction.....	32
2.2.2. Acoustic Sensing .....	34
2.2.3. Back Volume Impedance .....	39
2.2.4. Lumped Elements Model.....	39
<b>2.3. Microphone Noise</b> .....	46
2.3.1. Noise sources .....	46
2.3.2. Noise analysis .....	48
<b>CHAPTER 3 MICROPHONE DESIGN AND FABRICATION</b> .....	50
<b>3.1. Device Fabrication</b> .....	50
3.1.1. Process flow .....	50
3.1.2. Critical dimensions and risks.....	55
3.1.3. Process adaptation .....	58
<b>3.2. Achievable performance</b> .....	61



3.2.1.	Cut-off frequency .....	61
3.2.2.	Noise Level.....	62
3.2.3.	Linearity .....	64
3.2.4.	Resonance Frequency .....	69
3.2.5.	Sensitivity.....	69
<b>3.3.</b>	<b>Microphone Design Process .....</b>	<b>71</b>
3.3.1.	Initial design parameters .....	71
3.3.2.	AVATRAM Dimensions .....	74
3.3.3.	Electrode Design .....	76
3.3.4.	Final Structure .....	78
3.3.5.	Final Devices .....	80
<b>CHAPTER 4</b>	<b>RESULTS AND DISCUSSION.....</b>	<b>82</b>
<b>4.1.</b>	<b>First fabrication batch .....</b>	<b>82</b>
4.1.1.	Fabrication results .....	82
4.1.2.	Device characterization .....	85
<b>4.2.</b>	<b>Second fabrication batch.....</b>	<b>98</b>
<b>CHAPTER 5</b>	<b>CONCLUDING REMARKS .....</b>	<b>103</b>
<b>APPENDICES</b>	<b>.....</b>	<b>105</b>
<b>Appendix A.</b>	<b>Main microphone specifications .....</b>	<b>105</b>
<b>Appendix B.</b>	<b>Acoustic impedance of small rectangular cavities .....</b>	<b>108</b>
<b>Appendix C.</b>	<b>Electronic Readout Circuit .....</b>	<b>116</b>
<i>BIBLIOGRAPHY</i>	<i>.....</i>	<i>119</i>
<i>LIST OF ACRONYMS</i>	<i>.....</i>	<i>125</i>
<i>RESUME</i>	<i>.....</i>	<i>126</i>

# *Abstract*

In recent years, **MEMS** (micro-electromechanical system) microphones have become a key component in a wide range of consumer electronic devices. The need to improve upon existing applications, such as voice pickup for phone calls, as well as the development of new ones, like the widespread use of speech recognition systems, have propelled the ever increasing demand for higher performance microphones. This has driven the optimization of the current technology to its limits, as the large majority of commercial **MEMS** microphones are based on variations of a simple condenser design: a deformable membrane, facing a perforated and fixed counter-electrode (backplate), and sitting on top of a cavity maintained at atmospheric pressure, commonly referred to as Back Volume (**BV**). In this design, the capacitive transduction is performed in air, leading to unavoidable squeeze-film damping and acoustical resistance due to the presence of the backplate, which become the dominant noise sources in the device. Limited by these noise sources, the signal-to-noise ratio (**SNR**), representative of the overall performance of the microphone, can only be improved at the cost of a larger chip and **BV** size. Although several other design changes and improvements have been proposed, they have had little to no success in increasing the **SNR** without increasing the size of the device. Alternatively, designs based on piezoelectric transduction seem to promise a higher performance as they do not incorporate a backplate. However, their performance is found to be limited by the intrinsic losses of currently available piezoelectric materials.

This present work proposes a new approach for reducing the viscous damping losses, and improving the performance of capacitive **MEMS** microphones, by separating the backplate from the membrane and performing the transduction in vacuum. In this new design, the device is separated into two parts: a rigid piston that harvests the acoustic sound pressure in air, mechanically connected to a capacitive transducer encapsulated in a vacuum cavity. This separation drastically reduces the acoustic noise sources in the device and allows a high capacitive density, which significantly improves the **SNR** of the microphone without necessarily increasing its size. The connection between both elements is ensured by an innovative mechanical hinge, capable of transferring a mechanical motion between two separate atmospheres. In this study, the mechanical hinge is first designed to be robust enough to withstand the effects of atmospheric pressure and possible high pressure overshoots, while remaining flexible enough to transfer the mechanical motion. An analytical model of the microphone is then developed, detailing the theory of operation of the device, and the achievable performance levels and size limitations are discussed. The final devices are designed based on the theoretical framework of the analytical model, taking into account the critical

dimensions set by the two-wafer fabrication process. These devices have been successfully fabricated, and the encountered fabrication problems have been analyzed and corrected. Furthermore, the first wafer-level experimental results prove the viability of this new device concept. The transfer of the force from the piston in air to the encapsulated transducer was proven, and the acoustic response of the devices was successfully measured with a sensitivity reaching  $6 \pm 0.5\text{fF/Pa}$ . With this first proof of concept, this new design paves the way for ultra-high performance **MEMS** microphones.

# Chapter 1 Introduction

## 1.1. On the origins of MEMS microphones

Although the beginnings of microphone development can be arguably traced back to the race for the invention of the telephone in the 1870's, the closest ancestor of modern day **MEMS** microphones is perhaps found in the first condenser microphone invented by E.C. Wentz of Bell Labs in 1917 [1]. Mainly composed of a thin steel diaphragm stretched in front of a conductive plate on top of a closed volume, this microphone set the foundations for all future condenser microphone designs: any deflection of the flexible diaphragm due to an incoming sound wave changes the air-gap between the two highly polarized electrodes, thus leading to a detectable variation of capacitance [2]. At the time of Wentz's invention, the idea of such an electrostatic transducer was not a new concept [3]. However, the use of the condenser microphone only became practical with the recent development of vacuum-tube amplifiers, necessary to reach good device sensitivities [4].

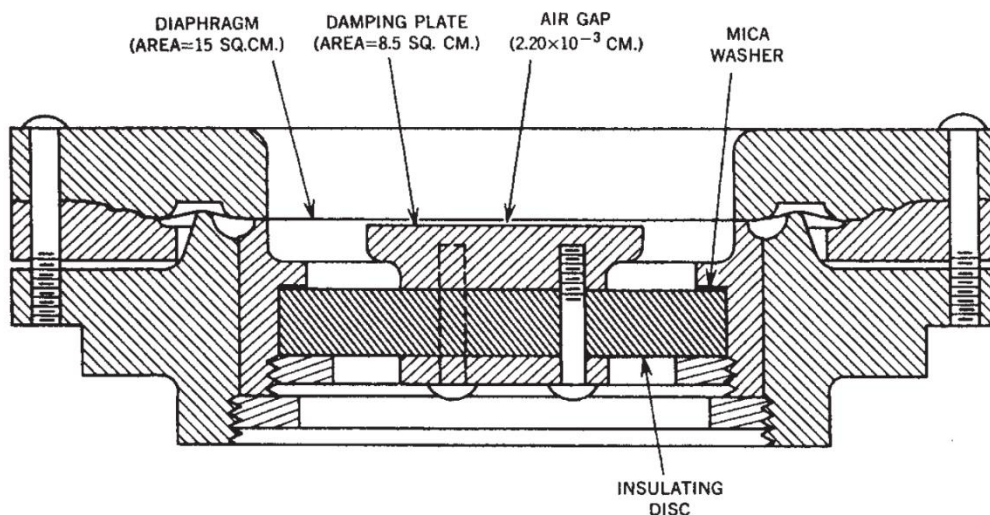


Figure 1.1: E.C Wentz microphone [1].

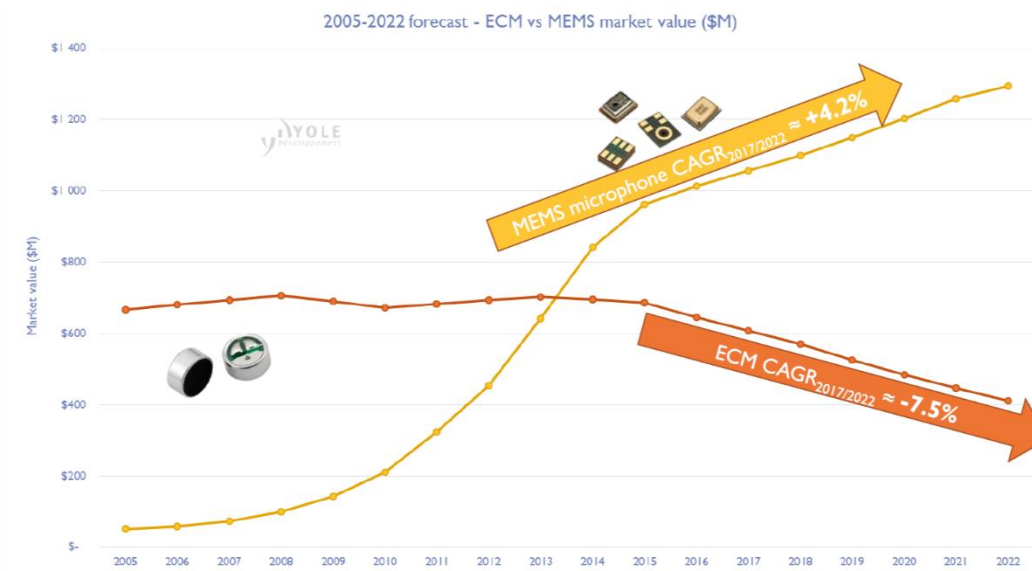
Despite their excellent stability and flat frequency responses in the audible range, condenser microphones of the time still required very high polarization amplitudes (200 V to 300 V) due to their low capacitances and high impedances. G. Sessler and J. West remedied this inconvenience with their invention of the foil Electret Condenser Microphone (**ECM**) in 1962, in which they replaced the steel diaphragm by a metallized electret foil [5]. Electrets, known as charge preserving materials,

had been used for microphone applications since the beginning of the 20<sup>th</sup> century. Yet, due to their poor electrical stability and large-scale sensitivity fluctuations, early thick wax electret microphones failed to become a commercial success. By using thin films of Mylar and Teflon, Sessler and West successfully dispensed with external DC polarization: the effective polarization amplitude of their first “self-biasing” microphone reached up to 200 V [6]. Furthermore, in addition to their high sensitivity and lower cost, **ECMs** were less sensitive to structure-borne noise because of the low mass of their diaphragms. This prompted Sony to start producing and using them for portable tape recorders in 1968, marking the start of the exponential growth of the **ECMs**’ market [7]. Nevertheless, even though they dominated the high volume microphone market for almost half a century, the long reign of **ECMs** was not to last.

In his 1982 paper entitled “Silicon as a mechanical material”, K. Petersen discussed the growing scientific and commercial interests in using silicon not only for microelectronics but also for the development of integrated, cheap and high-performance sensors and transducers [8]. Despite the fact that Petersen makes no mention of microphones in his paper, it was only a year later that the first micro-fabricated microphones were announced: one based on the piezoelectric effect, and the other on the electret condenser principle [9], [10]. It then took 20 years of research and development for the first commercial **MEMS** microphones to hit the market, with the introduction of the SiSonic **MEMS** microphone from Knowles in 2002. Originally, due to their higher performance and smaller size, they were mainly considered for hearing aid applications [11]. The focus later shifted to commercial applications with the growth of the mobile handset market in the 2000’s. Ever since, the market for **MEMS** microphones has been growing rapidly, greatly benefiting from the boom of consumer electronics: in 2014, **MEMS** dethroned **ECMs** as the highest selling microphone technology.

## 1.2. Market and trends

Since 2003, **MEMS** microphones have made their way to almost all markets and applications. From high volume portable electronics to low volume medical and military applications, **MEMS** have become the go to microphones, selling over 5 billion units worldwide in 2017, for a total revenue of around \$1B [12]. According to Yole développement, this market is projected to continue growing to reach an estimated value of around \$1.3B in 2022 [13]. Historically, the commercial success of **MEMS** microphones has been mainly due to the consumer electronics market. More precisely, the demand for **MEMS** microphones has increased rapidly with the steady increase of the number of microphones per mobile phone. The evolution of the number of microphones in the Apple iPhone is a telling example: from two **MEMS** microphones in the 2010 iPhone 4, the number doubled in four years with the iPhone 6s. This increase in demand has also been accompanied by more demanding requirements of higher performance levels and smaller device sizes. It is therefore no wonder that research and development in **MEMS** microphones has been largely influenced by trends in this market.

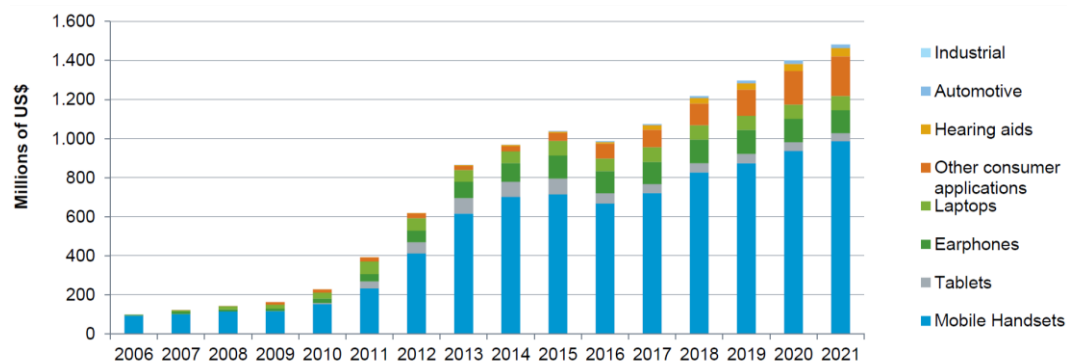


**Figure 1.2: 2005 - 2022 forecast markets of ECMs and MEMS microphones. In 2014, MEMS microphones surpassed ECMs in market value, and they are expected to grow with a Compound Annual Growth Rate (CAGR) of 4.2% [13].**

During the last decade, mobile phones have come to play an increasingly important role in daily life. No longer limited to their original intended use, smartphones are now also used to take photos, videos, as well as consume and share content on social media and the web. Artificial Intelligence (AI) has also been introduced to nearly every smartphone in the form of a virtual personal assistant, the likes of Siri and Alexa, which can be prompted and accessed by voice commands. Thus, with the addition of burgeoning Internet Of Things (IOT) applications, the consumer market has been the source of the main drivers for increasing the performance levels (Appendix A) of **MEMS** microphones:

- High fidelity sound transduction to improve the quality of phone calls and the sound quality of videos and content shared on social media
- Low output distortion to improve the accuracy of signal processing algorithms for **AI** and **IOT** applications

In terms of performance parameters, these demands for higher performance are mainly answered by an increase in Signal-to-Noise Ratio (**SNR**) and Acoustic Overload Point (**AOP**). On one hand, the **SNR** is a general indicator of performance, determining the quality of the microphone’s output based on its noise level. Since the latter is equivalent to the lowest accurately measurable signal, a higher **SNR** means a better signal quality even for low sound levels. This becomes more critical when considering that sound pressure halves for every doubling of the distance: improving a microphone’s **SNR** not only improves its signal quality but also increases its capturing range. On the other hand, the **AOP** indicates the sound pressure level for which the maximum acceptable signal distortion is reached. Increasing the **AOP** therefore increases the range of sound pressures that the microphone transduces accurately and with high fidelity, which, combined with a high **SNR**, improves the accuracy of speech recognition, ambient noise cancellation and wind noise rejection systems. A high **AOP** also means that the microphone can handle very high sound levels, which is essential when recording in extremely loud environments.



**Figure 1.3: 2006 - 2022 MEMS microphone market by fields of application [12].**

Research and development of **MEMS** microphones has strived to meet the performance requirements of the market while keeping a small device form factor. In this endeavor, all transduction methods have been considered, and until recently, performance levels have been met, albeit at a higher device cost. However, as it shall be detailed in the next section, device optimization seems to have reached its limits: any further increase in performance will only be possible at the cost of a greater increase in die and packaging size. As these devices are fabricated in batch on silicon wafers, any increase in size will reduce the number of microphones per wafer, thereby further increasing device cost. Thus, a breakthrough in **MEMS** microphones technology has long been awaited.

## 1.3. State of the art

As it can be inferred by their name, **MEMS** microphones can be divided into three main parts: a pressure sensitive mechanical element, a transducer converting the mechanical energy to the electrical domain, and a signal amplifying Readout Electronic Circuit (**ROEC**). Each element plays an important role in the sensing chain. However, it is the chosen transduction method that has the largest impact on the design and eventual performance of the microphone. In the race for higher performance and smaller device size, a plethora of microphone designs has been proposed, and each design has been judged according to its advantages and drawbacks. Piezoresistive and Field Effect Transistor microphones have been quickly disqualified given their limitation in terms of high intrinsic noise levels, whereas the development of optical microphones has lagged behind possibly due to onerous requirements in terms of light-source and packaging [14], [15]. The following will therefore focus on capacitive and piezoelectric microphones, which have been the only technologies to reach both performance requirements and commercial success.

### 1.3.1. Capacitive MEMS microphones

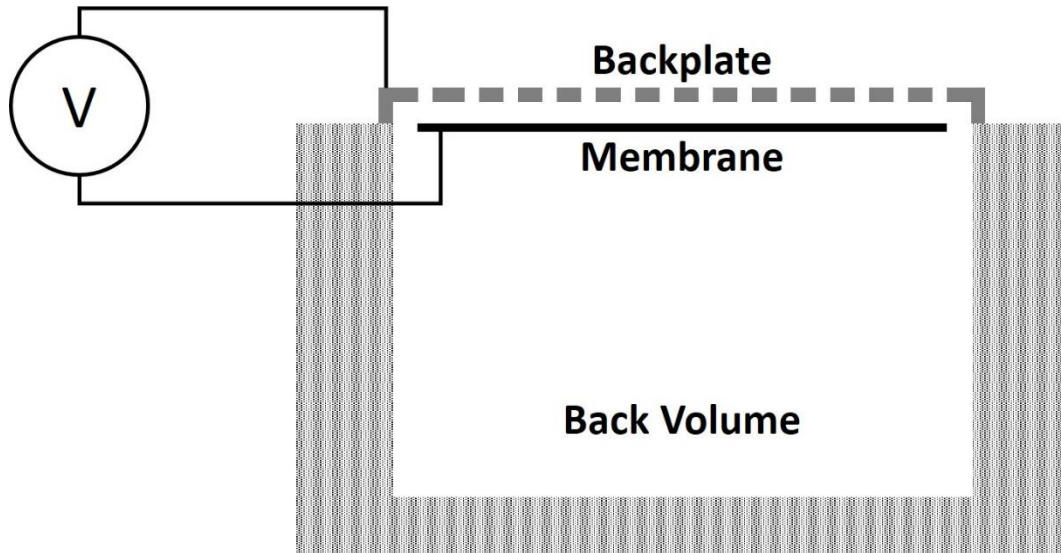
#### General concept

The vast majority of **MEMS** microphones currently on the market are based on a simple condenser design, not unlike Wente's original invention. As such, the fundamentals of capacitive sensing for microphone applications have become quite well known. Generally, when two conductive plates are polarized, the capacitance between the electrodes is given as [16]:

$$C = \varepsilon_0 \varepsilon_r \frac{A}{g_0} [\text{F}] , \quad (1.1)$$

where  $A$  is the electrodes' overlap area,  $g_0$  the gap separating the electrodes, and  $\varepsilon_0$  and  $\varepsilon_r$  are dielectric constants. Any variation of either the overlap surface or the gap between the electrodes can thus lead to a measurable change in the capacitance of the two plates. Gap variation has been historically privileged for microphone applications, due to the simplicity and efficiency of its design. When a flexible membrane or diaphragm is stretched on top of a cavity maintained at atmospheric pressure (commonly called a Back Volume) via small perforations, it can be deflected by the pressure difference generated by an incoming sound wave. A capacitor can then be easily formed by adding a fixed counter-electrode or backplate (**Figure 1.4**). Thus, the movement of the membrane, and therefore the sound generated pressure difference, can be directly transduced through changes in the gap between the two electrodes.





**Figure 1.4: Simplified schematic of simple condenser design MEMS microphones.**

The first micromachined microphones based on this concept were mostly of the electret type, a consequence of large capacitance gaps, which imposed the requirement of high polarization amplitudes [17], [18]. This changed in the early 90's, partly because of the poor quality of thin film electrets, but mostly due to the development of more advanced fabrication processes [11]. In fact, wafer-to-wafer bonding and sacrificial layer etching techniques made much smaller capacitance gaps possible, removing the need for a high voltage polarization [19], [20]. However, these first capacitive microphones were plagued by low sensitivities and much reduced frequency responses [21]. This is a direct consequence of the narrower gaps, which lead to very high squeeze-film damping between the diaphragm and the backplate. Bergqvist et al. solved this problem in 1991 through the use of a highly perforated backplate which greatly decreased the damping between the electrodes [22]. The use of acoustic holes extended the microphone's frequency response to 20 kHz. The sensitivity of the microphone can be approximated by [23]:

$$S \approx \frac{U_0}{g_0} C_m \text{ [V/Pa]}, \quad (1.2)$$

where  $U_0$  is the polarization voltage amplitude and  $C_m$  the mechanical compliance of the membrane. Defined as the ratio of the average deflection to the applied sound pressure (in  $m/Pa$ ), the compliance of the membrane is proportional to the square of the membrane's radius, and inversely proportional to the membrane's intrinsic stress and thickness. It can easily be deduced from **equation (1.2)** that the microphone's sensitivity can be simply increased with a more compliant membrane. However this can be hindered by the push towards smaller devices, given that a smaller membrane will exhibit a much lower compliance. Furthermore, any increase in the membrane's compliance means a decrease of stiffness, leading to a decrease in the resonance frequency and therefore in the **Bandwidth (BW)** of the device. It will also lead to a lower applicable polarization amplitude for a given capacitance gap, since the pull-in voltage is proportional to the square root of the

membrane's stiffness. A more compliant membrane will also reduce the deflection amplitude at which the acceptable device nonlinearity is reached for a given gap, decreasing the **AOP** of the device. In the light of these counteracting consequences on device performance, the necessity of finely optimizing the mechanical compliance of the membrane becomes evident.

Scheeper et al. improved upon the perforated backplate design by studying the effects of the compliances of both the diaphragm and the backplate on the microphone's bandwidth and sensitivity [24]. By reducing the thickness of the diaphragm from  $1\ \mu\text{m}$  to  $0.24\ \mu\text{m}$ , they were able to improve the device sensitivity, albeit at the cost of a much-reduced bandwidth. The resonance frequency of the device was then found to be proportional to the number of holes in the backplate, and inversely proportional to the sum of the mechanical sensitivities of both the backplate and the diaphragm. Thus, when coupled with a high acoustic hole density (40% of the backplate's area), a higher backplate stiffness led to a higher resonance frequency, and therefore extended the frequency response from  $2\ \text{kHz}$  to  $14\ \text{kHz}$ . The stiffer backplate also increased the pull-in voltage thereby increasing the applicable polarization and the device sensitivity.

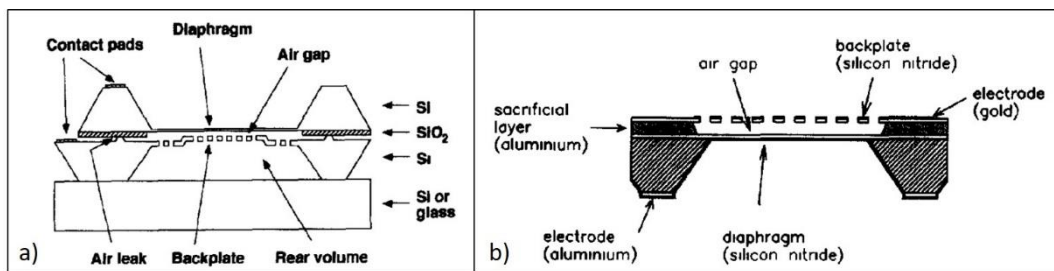


Figure 1.5: Microphone design improvements proposed by Bergqvist et al. (a) and Scheeper et al. (b)

Reducing the thickness of the membrane can however be counterproductive, as the intrinsic stress in the resulting thin-film can become very high [25]. Besides changing the material itself, the stress can be reduced through purely technological efforts such as adjusting the fabrication process parameters [26], [27]. However, the effectiveness of this method alone remains limited compared to the other proposed solutions: corrugated diaphragms and spring-supported diaphragms. Corrugations can relieve the residual stress in the diaphragm as well as reduce overall stiffness. The resulting mechanical compliance highly depends on the number and depth of the corrugations, which can be optimized through Finite Element Modeling (**FEM**) [28]–[32]. As for spring-supported diaphragms, the residual stress is released through flexible structures all around the structure [33]–[36]. This change in the boundary conditions can also greatly increase the mechanical compliance depending on the chosen spring design. These spring structures can however become areas of stress concentration under high pressures, which has led some industrials to prefer a more robust corrugated clamped membrane [37], [38].

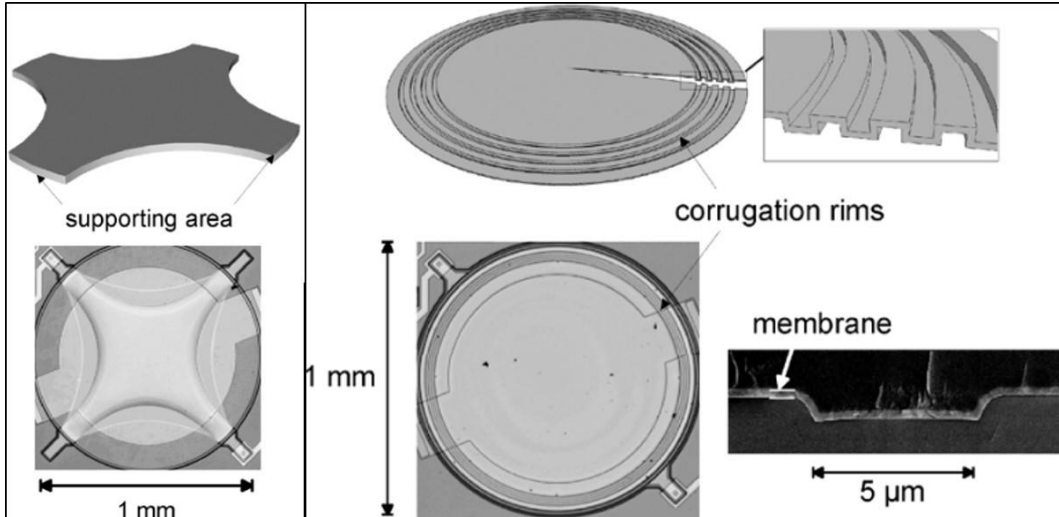


Figure 1.6: Examples of a spring supported diaphragm (left) and corrugated diaphragm (right) adapted from [37].

As we have shown, the sensitivity of capacitive **MEMS** microphones can be improved by several ways: increasing the size of the diaphragm, increasing the polarization voltage, reducing the air gap or reducing the membrane's thickness and relieving its residual stress. However, as the requirements for smaller size and higher performance become more demanding, the benefits taken from these improvements become limited when the noise of the device is also considered. The noise of early capacitive **MEMS** microphones was dominated by the noise of the signal amplifying circuitry connected to it [24]. In this case, the **SNR** of the device could only be improved by increasing its sensitivity to mask the circuitry noise. With the development of more performing **ROEC**, the noise contribution of the **MEMS** sensor became more and more important, reaching more than half of the total device noise [38], [39]. Analyzing and reducing the noise sources within the **MEMS** sensor is therefore necessary in order to improve its **SNR**.

## MEMS microphone noise and the backplate tradeoff

According to the Fluctuation-Dissipation theorem, the presence of any dissipation mechanism within a certain system leads to a fluctuating force acting on the system [40]. Any resistance within the system will then lead to fluctuations and therefore to added noise [41]. Nyquist's relation, commonly used for quantifying the Johnson electrical resistance noise, gives the spectral density of the resulting fluctuating force. For an electroacoustic transducer such as a microphone, the main damping mechanisms are found to be related to acoustical resistances, losses due to air viscosity. The spectral density of the fluctuating pressure, i.e. of the resulting noise, can then also be derived from Nyquist's relation:

$$P = \sqrt{4k_B T R_{ac}} [Pa/\sqrt{Hz}], \quad (1.3)$$

where  $k_B$  is Boltzmann's constant,  $T$  is the absolute temperature and  $R_{ac}$  is the acoustic resistance. The noise of microphones based on the simple condenser design is dominated by two main sources, the first of which is the resistance due to

squeeze-film damping. Taking place between the membrane and the backplate, these losses have been approximated by [42]:

$$R_g = \frac{12\mu l}{n\pi g_0^3} B(A_h)$$

$$B(A) = \frac{1}{4} \ln\left(\frac{1}{A_h}\right) - \frac{3}{8} + \frac{1}{2} A_h - \frac{1}{8} A_h^2, \quad (1.4)$$

where  $\mu$  is the air viscosity,  $l$  the backplate's thickness,  $n$  the number of holes,  $g$  the air gap and  $A_h$  the surface fraction occupied by the holes. The second is the resistance due to the viscous flow losses through the perforations of radius  $r$  that maintain the Back Volume (**BV**) at atmospheric pressure:

$$R_h = \frac{8\mu l}{n\pi r^4} \quad (1.5)$$


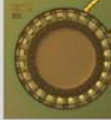
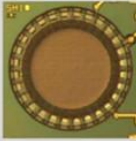
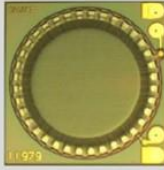

It is evident from the equations that the noise can be significantly reduced by either increasing the air gap between the two electrodes or by increasing the number and size of the perforation holes in the backplate. However, this will bring about a considerable loss in the active capacitance of the device, decreasing its sensitivity. To counter these penalties, according to **equation (1.2)**, a constant sensitivity can be maintained by either increasing the polarization amplitude, or, more preferably, by increasing the size of the electrodes in order to compensate for the lost active capacitance. It is for this reason that, in recent years, the increase in microphone **SNR** has been accompanied by an increase in die size (**Figure 1.7**) [38]. What is more, this evident consequence of maintaining the sensitivity hides another requirement concerning the size of the device: an increase in the size of the **BV**.


As explained in **Appendix B**, the **BV** exhibits an acoustic compliance, which can be simply understood as the volume of air that the cavity can accommodate per applied pressure (in  $m^3/Pa$ ). The **BV** therefore reacts to the movement of the membrane, since the membrane is displacing air into the cavity. When the effect of the **BV** is considered, the device sensitivity can be approximated by [43]:

$$S \approx \frac{U_0}{g_0} \frac{C_m \cdot V}{C_m \cdot A \cdot \rho \cdot c^2 + V}, \quad (1.6)$$

where  $\rho$  is the density of air,  $c$  is the speed of sound in air and  $V$  the size of the **BV**. For very small **BVs**, the sensitivity of the device becomes mainly determined by size of the cavity. For the smaller a **BV** is, the smaller the volume that it can accommodate, and therefore the stronger it will oppose the movement of the membrane and reduce the sensitivity.

Consequently, the dominant noise sources in the device, both due to the presence of the backplate, result in a tradeoff: any increase in the **SNR** of the **MEMS** sensor while maintaining a high sensitivity will come at the cost of a much larger overall device size. This means that reaching the required high performance parameters is only possible by increasing the overall size and the cost of devices. This, unsurprisingly, goes against current market trends.

Die Size	0.64 mm <sup>2</sup>	0.81 mm <sup>2</sup>	1.0 mm <sup>2</sup>	1.44 mm <sup>2</sup>	1.96 mm <sup>2</sup>
Sample					
Diameter	0.5 mm	0.6 mm	0.7 mm	0.9 mm	1.1 mm
Package Backvolume	1.1 mm <sup>3</sup>	1.1 mm <sup>3</sup>	1.1 mm <sup>3</sup>	3.0 mm <sup>3</sup>	3.0 mm <sup>3</sup>
SNR	59 dB	60 dB	61 dB	64 dB	66 dB



Dual Infineon MEMS Microphone Evolution

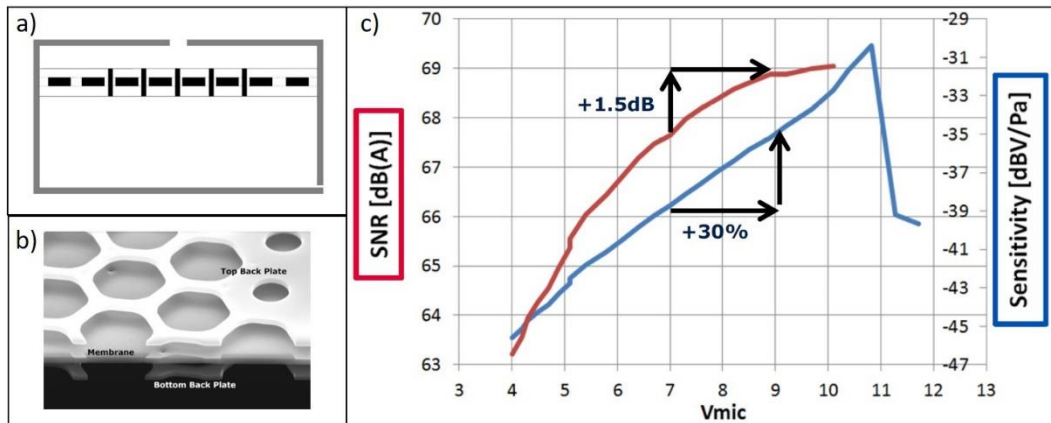
Figure 1.7: Table showing the increased die and BV sizes with increasing SNR (adapted from [38] and [13]).

## Overcoming the backplate hurdle

Increasing the signal of a device without enlarging it remains possible by simply sandwiching the membrane between two perforated counter-electrodes. This idea finds its roots in a 1996 design, originally proposed for increasing the sensitivity of microphones targeting hearing aid applications [44]. A perforated backplate is hermetically encapsulated between two diaphragms, which are interconnected by pillars in their central area in order to reduce their sensitivity to static pressure changes (**Figure 1.8.a**). Due to its relatively complicated fabrication process and stability issues, work on this dual diaphragm microphone was later discontinued in favor of a dual perforated backplates design [45]. Multiple dual backplate microphones were then developed in an effort to benefit from the advantages of this design [46]–[48].

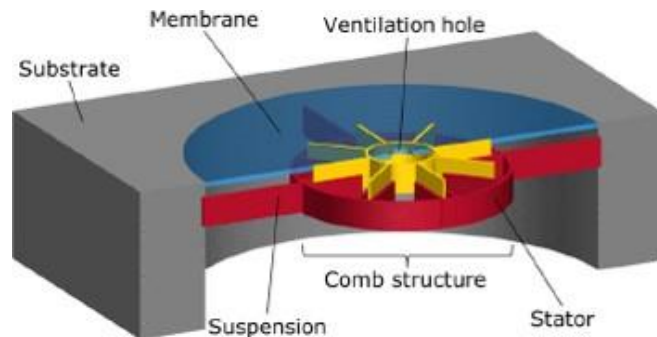
Due to counteracting nonlinear electrostatic forces, the differential configuration of the two backplates increases the linearity of the **MEMS** sensor. It also cancels second order harmonics and common mode noise in the **ROEC**, which reduces its overall distortion and noise [49]. Concerning the noise of the **MEMS** sensor, it is evident that, despite doubling the sensitivity, the addition of a second perforated electrode will also add a second noise source to the device. This may seem counterproductive, since the objective is to reduce the noise and increase the **SNR**. However, the balancing of electrostatic forces between the electrodes increases their pull-in voltage, making a higher polarization amplitude possible [50]. The dual backplate design can therefore be used to increase the **AOP** and the **SNR** of the device without necessarily increasing its size. However, as it can be seen in **Figure 1.8.c**, the increase in **SNR** is found to still be limited, as the polarization amplitude

cannot be increased infinitely. Hence, this design cannot be considered as a permanent solution.



**Figure 1.8:** Dual Diaphragm microphone design (a) (adapted from [44]); SEM cross-section of a Dual Backplate microphone (b) and a graph showing the increase of SNR and sensitivity in Dual Backplate microphones due to higher applicable polarization amplitude (c) (adapted from [49]).

Alternatively, an answer to the limitations imposed by the need for a backplate might be found in a complete change of the initial simple condenser design. Recently, backplate-less microphones have been proposed, based on surface variation capacitance change between moving and fixed electrodes [51]–[54]. Although most of these designs fail to meet modern requirements for sensitivity, **SNR** and **BW**, a notable exception is found in the star-comb microphone concept proposed in 2017 [55]. This device is composed of an interdigitated comb structure, with one set of comb fingers connected to a circular membrane and the other set fixed to the substrate to form the stator (**Figure 1.9**). This is a promising design as it substitutes the squeeze-film damping and the viscous losses in the perforation holes with slide-film damping [56]. As it will be detailed in the next chapter, this type of damping is inherently lower than the other damping mechanisms. As such, the theoretical acoustic **SNR** of the **MEMS** sensor was found at  $73\text{ dB(A)}$ . However, this result was obtained without the consideration of the **ROEC** noise, which will substantially reduce the overall **SNR** of the device. Furthermore, the sensitivity of  $-44.5\text{ dBV/Pa}$  is still lacking compared to current requirements.



**Figure 1.9:** Schematic of the star-comb microphone design, showing the clamped circular membrane (bleu), connected to the movable set of comb-fingers (yellow). The stator (red) forms the set of fixed comb-fingers.

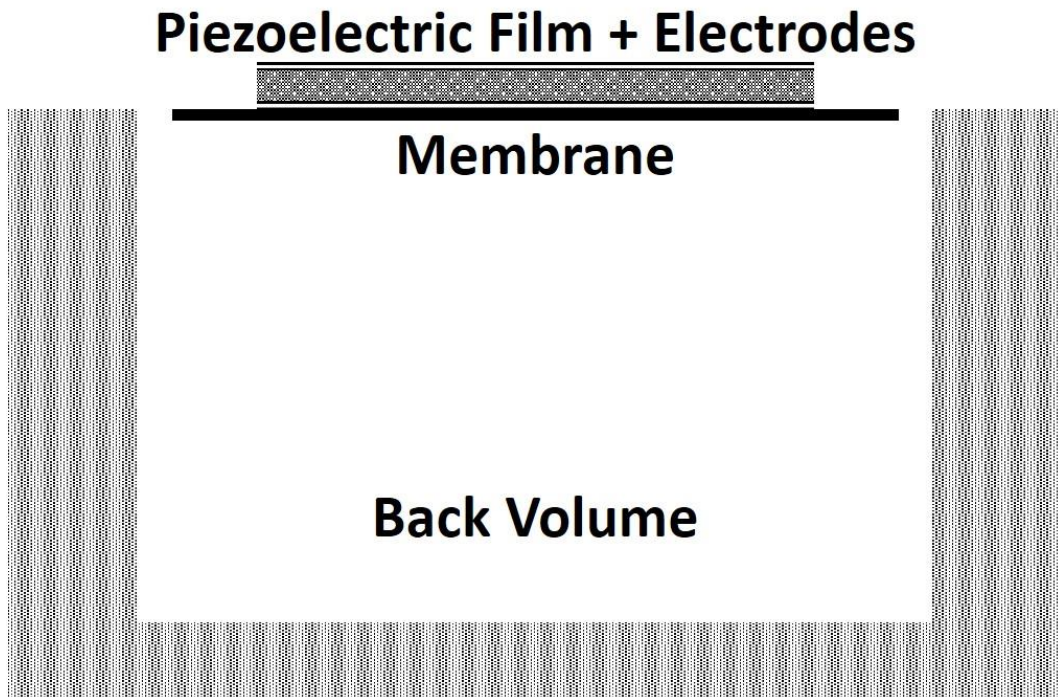


Hence, a higher performance capacitive microphone design that resolves the backplate issues is yet to be found.

### 1.3.2. Piezoelectric MEMS microphones

#### General concept

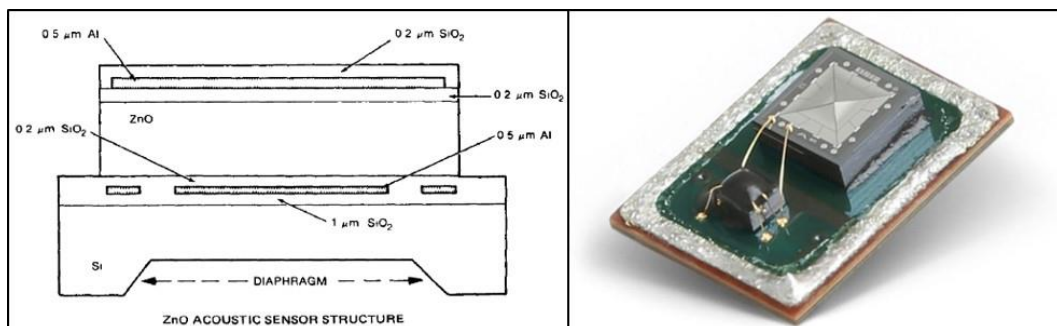
Ever since their discovery by the brothers Curie, piezoelectric materials have been the substance of keen scientific interest due to their remarkable electromechanical properties. When an applied force strains a piezoelectric material, it leads to a measurable distribution of charges on its surfaces. This is called the direct piezoelectric effect, as it is reciprocal; when the material is subjected to an external electrical polarization, it undergoes a mechanical deformation. This is commonly called the indirect or reverse piezoelectric effect. It straightforwardly follows that the direct piezoelectric effect can be used for **MEMS** sensors, such as accelerometers or microphones. Concerning the latter, the most common and simple method is to deposit the piezoelectric material on a flexible membrane or diaphragm sitting on top of a **BV** (**Figure 1.10**) [15]. The deformation of the membrane, due to an impinging sound wave, will strain the piezoelectric material, leading to a detectable release of charges. Therefore, the piezoelectric sensor does not require external polarization, which is one of its main advantages. Sensing electrodes sandwich the piezoelectric material to efficiently retrieve the generated signal. Thus, the performance of a piezoelectric microphone will mainly depend on three factors: the properties of the piezoelectric material, the placement of the electrodes, and the conversion efficiency of sound pressure to piezoelectric material strain.



**Figure 1.10: Simplified schematic of a simple piezoelectric MEMS microphone.**

It is perhaps because of the simplicity of this design and the high compatibility of the chosen piezoelectric material with microfabrication processes that the first **MEMS** microphone was based on piezoelectric transduction. With a  $5\ \mu\text{m}$  thick ZnO (Zinc Oxide) layer on top of a  $30\ \mu\text{m}$  thick circular diaphragm, this first embodiment had a sensitivity of  $0.25\ \text{mV}/\text{Pa}$ , very low compared to electret microphones [9]. It was soon followed by a multitude of microphones based on ZnO and other materials such as PZT (Lead Zirconate Titanate) and AlN (Aluminum Nitride) [57]–[60]. With either low sensitivities (between  $0.085$  and  $0.920\ \text{mV}/\text{Pa}$ ) or high noise levels (higher than  $50\ \text{dB}(A)$ ), the performance of these microphones was still lacking compared to capacitive **MEMS** microphones of the time. Piezoelectric microphones failed to meet the required performance levels, and were therefore not considered for consumer applications.

However, in recent years, an interest in these microphones was rekindled by a new design with a notable improvement in performance [61]. Based on bimorph cantilevers instead of a single diaphragm, this design increases the harvested mechanical strain in the piezoelectric layers and significantly reduces residual stress, which was frequently cited as a detrimental factor for piezoelectric microphone sensitivity [62]. The performance was further increased through the optimization of the fabrication process of AlN, which exhibits better overall piezoelectric material properties than ZnO or PZT [63]. This prototype led to the first commercialization of piezoelectric **MEMS** microphones with the founding of a startup, Vesper. These microphones have a strong selling point given their various advantages, such as low power consumption, as well as water and dust resistance. The company currently offers microphones with a sensitivity of  $-38\ \text{dBV}/\text{Pa}$  and an **SNR** of around  $62\ \text{dB}(A)$  for a **BW** of  $20\ \text{kHz}$  [64]. However, when it comes to further improving device performance in terms of **SNR**, even with the most optimized mechanical design the performance will be limited by a noise source intrinsic to the piezoelectric material itself.



**Figure 1.11: Structure of the first piezoelectric microphone (left) (adapted from [9]) and an uncapped piezoelectric microphone from Vesper (right).**

## Fundamental piezoelectric noise limitation

When a piezoelectric material is sandwiched between two electrodes, it does not form an ideal capacitor. It is rather modeled by a lossy capacitor, i.e. a capacitor and a resistor [65], [66]. The resistor reflects the active losses in the material and is given as:



$$R_{pze} = \frac{1}{\omega C_{pze} \tan(\delta)}, \quad (1.7)$$

where  $\omega$  is the radial frequency,  $C_{pze}$  is the capacitance and  $\tan(\delta)$  is the loss angle.  $\tan(\delta)$  is the dissipation factor of the piezoelectric material, and is therefore a property of the material itself. This dielectric-loss will be a noise source present in all piezoelectric microphones, regardless of mechanical design. In fact, in their 2017 paper, Yao et al. showed that when the architecture of the microphone is abstracted, a theoretical maximum achievable **SNR** could be identified when the dielectric-loss is considered to be the only noise source [67]. For a given material, this **SNR** is then found to be only a function of the size of the microphone's **BV**. This result can be demonstrated by following a similar yet simpler approach.

Considering the schematic shown in **Figure 1.10**, the capacitance  $C_{pze}$  of the piezoelectric film of width  $w_{pze}$ , length  $l_{pze}$  and thickness  $t_{pze}$  is:

$$C_{pze} = \epsilon_r \epsilon_0 \frac{l_{pze} w_{pze}}{t_{pze}}, \quad (1.8)$$

where  $\epsilon_0$  and  $\epsilon_r$  are the vacuum and relative permittivity respectively. Considering the simple case of a negligible electric field generated across the piezoelectric material, for an in-plane strain  $\epsilon_{pze} = \delta l / l_{pze}$ , the out-of-plane electric displacement  $D_{pze}$  is given as [16]:

$$D_{pze} = e_{31} \frac{\delta l}{l_{pze}}, \quad (1.9)$$

where  $e_{31}$  is the piezoelectric coupling coefficient in the 3-1 deformation geometry (**Figure 1.12**), which is the most commonly used direction for piezoelectric coupling as it is the easiest to apply for transducers, even though it is not the most efficient. The total number of generated charges  $Q_{pze}$  can then be obtained:

$$Q_{pze} = e_{31} l_{pze} w_{pze} \frac{\delta l}{l_{pze}}. \quad (1.10)$$

The electrical energy generated by the strain applied to the piezoelectric film can then be simply derived from the equation of potential energy of a capacitor using **equations (1.8) and (1.10)**:

$$W_{elec} = \frac{1}{2} \frac{Q^2}{C} = \frac{1}{2} \frac{e_{31}^2}{\epsilon_r \epsilon_0} \frac{w_{pze} t_{pze}}{l_{pze}} (\delta l)^2. \quad (1.11)$$

Furthermore, under the applied mechanical strain, the piezoelectric film can be assimilated to a spring, exhibiting an opposing in-plane spring stiffness  $k_{pze}$ :

$$k_{pze} = E_{pze} \frac{w_{pze} t_{pze}}{l_{pze}}, \quad (1.12)$$

where  $E_{pze}$  is the Young's modulus of the piezoelectric material. Consequently, the stored mechanical energy in the material can be written as:

$$W_{mech} = \frac{1}{2} k_{pze} (\delta l)^2 = \frac{1}{2} E_{pze} \frac{w_{pze} t_{pze}}{l_{pze}} (\delta l)^2. \quad (1.13)$$

The electrical energy can now be expressed in terms of mechanical energy:

$$W_{elec} = \frac{e_{31}^2}{\epsilon_r \epsilon_0 E_{pze}} W_{mech}. \quad (1.14)$$

Ideally, given the chosen deformation geometry, in order to have the highest conversion efficiency, the entire mechanical force generated by an incoming soundwave should be applied in plane on the piezoelectric film. This means that, when an incoming sound wave displaces the diaphragm, all of the mechanical energy should be transferred to the piezoelectric film. Although this is not a realistic scenario, this consideration gives a maximum to the obtainable electrical energy. Thus, for the highest conversion efficiency, the stored mechanical energy should be equal to the energy harvested from the incoming sound wave. At an applied acoustic pressure difference  $\Delta P$ , the out-of-plane displacement  $dz_{mech}$  of the diaphragm of surface  $S$  and stiffness  $k_{mech}$  can be approximated by:

$$dz_{mech} = \frac{\Delta P \cdot S}{k_{mech} + k_{acou}}, \quad (1.15)$$

where  $k_{acou} = S^2/C_{BV}$  is the acoustic stiffness added to take into account the compliance  $C_{BV}$  of the **BV**. The stored mechanical energy due to this displacement is then written as:

$$W_{mech} = \frac{1}{2} k_{mech} dz^2 = \frac{1}{2} k_{mech} \left( \frac{\Delta P \cdot S}{k_{mech} + k_{acou}} \right)^2. \quad (1.16)$$

According to Littrell et al., in order to maximize this harvested energy, the compliance of the **BV** and the compliance of the diaphragm should be matched [68]. Otherwise, the energy will be limited by the smaller compliance, and advantage is not fully taken of the bigger one. Thus, the harvested energy is maximized when  $k_{acou} = k_{mech}$  and:

$$W_{mech} = \frac{(\Delta P)^2 C_{BV}}{8}. \quad (1.17)$$

Having thus found the maximum harvested mechanical energy, the maximum electrical energy can be expressed by injecting this expression into equation (1.14):

$$W_{elec} = \frac{e_{31}^2}{\epsilon_r \epsilon_0 E_{pze}} \frac{(\Delta P)^2 C_{BV}}{8}. \quad (1.18)$$

Hence, in an ideal case, the generated electrical energy depends solely on the size of the **BV** and on the properties of the piezoelectric material. Moreover, the signal current generated by a harmonic actuation at a frequency  $\omega_{sig}$  is:

$$i_{sig} = Q_{pze} \omega_{sig} = \sqrt{2W_{elec} C_{pze}} \omega_{sig}. \quad (1.19)$$

Meanwhile, the noise current generated by the dielectric-loss resistance is given by Nyquist's relation:

$$i_{noise} = \sqrt{\frac{4k_B T}{R_{pze}}} = \sqrt{4k_B T \tan(\delta) C_{pze} \omega}. \quad (1.20)$$

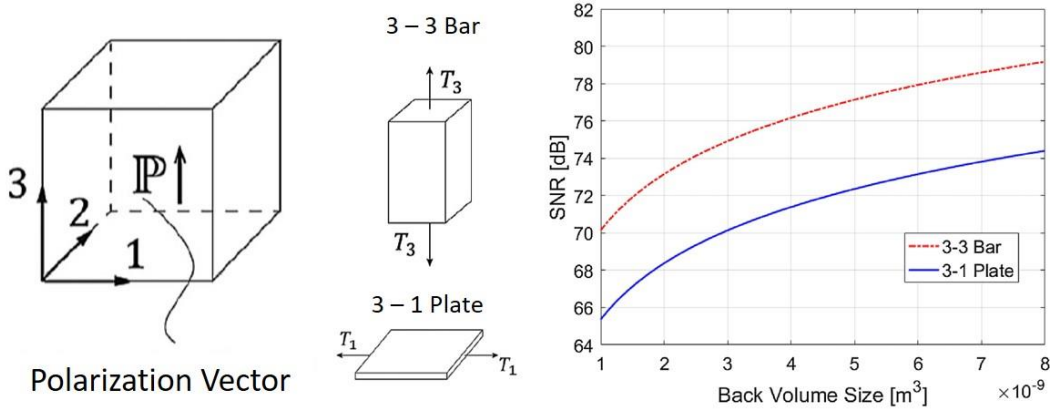
We can now finally find the highest achievable theoretical **SNR** of an ideal piezoelectric microphone where the only noise source is the one due to the dielectric loss:

$$SNR_{pze} = \frac{i_{sig}}{\int_{BW} i_{noise}}. \quad (1.21)$$

For an actuation of  $1 Pa$  at  $1 kHz$  over a **BW** of  $20 kHz$ , the A-weighted **SNR** depends only on the properties of the piezoelectric material and the size of the **BV**:

$$SNR_{pze} = 0.11 \sqrt{\frac{e_{31}^2}{\epsilon_r \epsilon_0 E_{pze} k_B T} \frac{C_{BV}}{8} \frac{\pi}{\tan(\delta)}}. \quad (1.22)$$

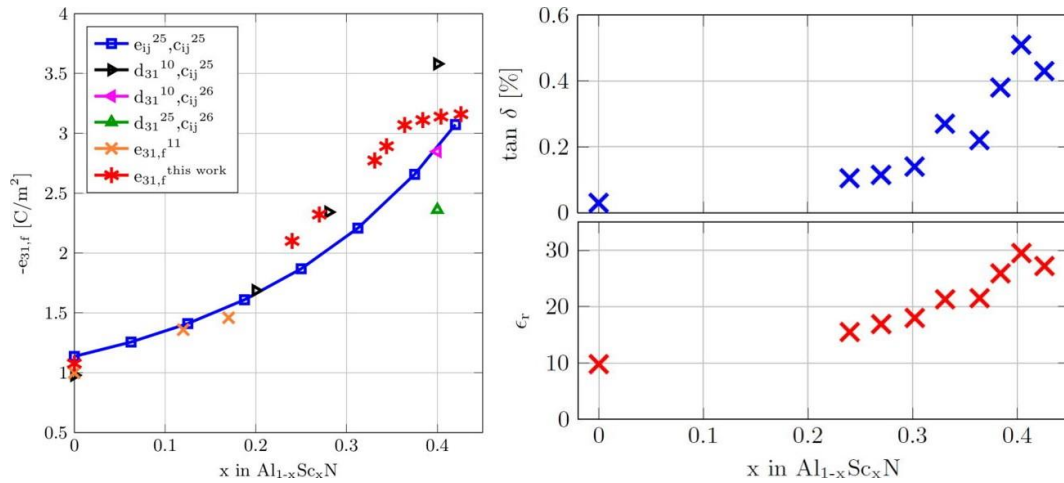
Consequently, it directly follows from this expression that there exists a fundamental noise limit to all piezoelectric microphones, one that cannot be surpassed by any design optimization. **Figure 1.12** shows the variation of the highest achievable **SNR** as a function of **BV** size for AlN, which is currently considered to have the best all-round piezoelectric properties. For a **BV** of  $3 mm^3$  the **SNR** is limited to  $70 dB(A)$ , even prior to the consideration of all other noise sources. The situation could be improved by adopting a 3-3 deformation geometry. However, this is rather unachievable, as it would greatly complicate the mechanical design. Thus, improving the performance of piezoelectric microphones without increasing their overall size is only possible with better piezoelectric material properties: a lower  $\tan(\delta)$ , a lower relative permittivity, and a higher coupling coefficient.



**Figure 1.12: Graph showing the variation of the highest achievable SNR as a function of BV size for AlN in two deformation geometries. The values are calculated for  $\tan(\delta) = 0.002$ ,  $\frac{e_{33}^2}{\epsilon_r \epsilon_0 E_{pze}} = 0.110$  and  $\frac{e_{31}^2}{\epsilon_r \epsilon_0 E_{pze}} = 0.037$  for the 3-3 Bar and 3-1 Plate geometries respectively (adapted from [67]).**

Research is ongoing to find new and better performing piezoelectric materials. However, even if it can outperform current options, any new material would still require years of research and development in order to reach the level of

technological maturity that is required for large-scale production. A more practical and timesaving approach is to try to improve upon the properties of the materials for which the fabrication processes are already well developed. A candidate that stands out in this endeavor is Scandium doped AlN (ScAlN). It has been shown that the piezoelectric properties of AlN can be enhanced by partial substitution of Al with Sc [69]. Although this presents a promising solution for the current limitation in microphone applications, the enhancement in piezoelectric coupling coefficient is however marred by an important increase in the material's  $\tan(\delta)$  dissipation factor and relative permittivity (**Figure 1.13**) [70]. Taking for example ScAlN doped at 40%, the high coupling coefficient of  $3.2C/m^2$  is opposed by a high  $\tan(\delta) = 0.5\%$  and a high relative permittivity  $\epsilon_r = 29$ . Considering that the Young's modulus decreases to around  $250GPa$  after the doping process [69], for a  $3mm^3$  **BV** and under normal conditions of temperature and pressure, **equation (1.22)** gives the highest achievable **SNR** a  $59dB(A)$ . Thus, the effects of the increase in  $\tan(\delta)$  and relative permittivity should be weighed against the enhancements of Sc doping. In this respect, more research is still required as reports on the dielectric loss of ScAlN at high Sc content are still scarce.



**Figure 1.13: Graphs displaying the influence of Scandium doping in AlN on coupling coefficient (left), dissipation factor and relative permittivity (right) (adapted from [70]).**

## 1.4. Next generation MEMS microphones

**Table 1.1** gives a sample of the devices currently offered by major MEMS microphones manufacturers on the market. These microphones are based on the previously detailed designs, and, as such, the compromises made to reach certain performance levels can be noticed. For example, the microphone offered by InvenSense stands out as the one with the highest SNR of 74 dB(A), though as the cost of a much lower AOP and larger BV. The next breakthrough in MEMS microphones needs to surpass these compromises. In fact, the presented limitations for both capacitive and piezoelectric MEMS microphones have been known for a while, foreseen by ongoing work towards finding a breakthrough in either technology. As we have previously mentioned, the development of new piezoelectric materials that would be better suited for high performance applications is ongoing. While this is a promising route, it can prove rather lengthy and unpredictable. However, recently proposed designs concerning the capacitive technology seem to offer a more easily attainable and straightforward solution. These new devices are still under development, and are yet to make their way to the largescale consumer market.

Microphone	Sensitivity (mV/Pa)	SNR (dB(A))	AOP (dB SPL)	BW (kHz)	Package Size (mm <sup>3</sup> )
Knowles [71]	18.5	70	130	13	19
InvenSense [72]	25	74	123	20	62
Infineon [73]	<i>N.A</i>	69	130	20	14.4
Vesper [64]	12.5	62	127	20	12.2

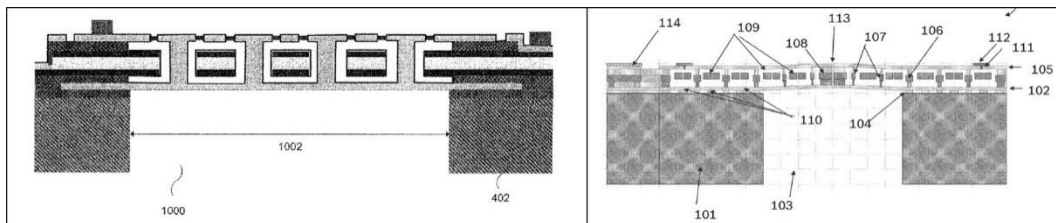
**Table 1.1:** Performance parameters of commercial microphones currently offered by major manufacturers. The Infineon microphone has a digital output with a  $-36$  dBFS sensitivity; the other microphones all have analog outputs.

### 1.4.1. Dual-Membrane Vacuum (DMV) microphones

When considering that the main noise sources in capacitive microphones are due to air damping, the idea of performing the transduction in vacuum comes quickly to mind. However, as it is always the case, what seems to be a simple idea in theory, proves to be much more challenging in practice. The reason resides in the fact that the main function of a microphone is to measure a difference of pressure. Therefore, it cannot be completely sealed off from the surrounding atmosphere. The idea then would be to have a capacitive transducer secluded from, yet still acoustically coupled to its surroundings. This has been previously achieved by the dual diaphragm microphone, which was originally proposed for increasing device

sensitivity by increasing its active capacitance: two interconnected diaphragms encapsulating a fixed electrode (**Figure 1.8.a**). In this configuration, the diaphragms couple the transduction to the surrounding acoustic changes while sealing off the transducer itself. However, at the time, the transducer was still filled with air.

Designs similar to this previous idea have been recently proposed, albeit with a major differentiating point: the fixed electrode is encapsulated in vacuum. This answers to both the acoustic coupling and the noise problems. On one hand, by keeping the dual diaphragm structure, the device is connected to outside pressure changes. On the other hand, the rarefied atmosphere between the electrodes means there is little viscous resistance, and the **MEMS** sensor noise is therefore drastically reduced. **Figure 1.14** shows two designs, one proposed by Infineon (left) and the other by Robert Bosch (right)[74], [75]. Aside from some differences, both design share the same dual-diaphragm structure and concept. No scientific reports have yet been published concerning these designs, a fact most probably due to company confidentiality. It is therefore still early to judge in detail the full potential of this idea. We do however note that, beside possible issues due to the complicated fabrication process, these devices do not put an end to all compromises. As the compliances of the **BV** and the membranes are still coupled, device performance can still be limited by small **BV** sizes. Nevertheless, these devices do deliver on their promise of a lower noise level. Some press articles have recently reported on a new Infineon microphone based on this design with an **SNR** reaching up to  $75\text{ dB}(A)$  [76].

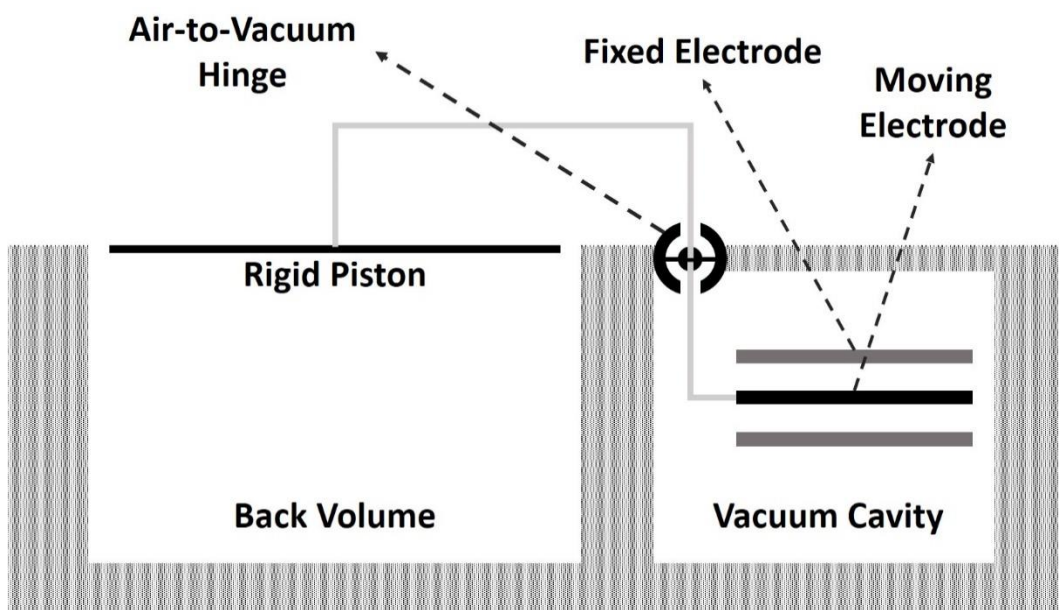


**Figure 1.14: The dual-diaphragm vacuum microphones proposed by Infineon (left) and Robert Bosch (right) (adapted from [74] and [75]).**

## 1.4.2. Air-to-Vacuum Transmission Microphone

The present research project offers a new solution to the limitations of capacitive **MEMS** microphones in the shape of a novel mechanical hinge capable of transferring a force between two separate atmospheres [77]. The microphone is thus separated into two parts connected by the hinge. A rigid piston sitting on top of a **BV** harvests the acoustic signal in air while capacitive electrodes perform the transduction in vacuum (**Figure 1.15**). The hinge forms an airtight seal between the surrounding atmosphere and the vacuum cavity, while ensuring the mechanical coupling of the capacitive transducer to the pressure variations of its surroundings.

The major advantage of this device resides in this separation, as the two parts, acoustic and electric, can be optimized separately, with no need for compromise. On one hand, since it is used for the sole purpose of harvesting the acoustic energy, the size of the piston can be reduced, reducing the total size of the device. This also makes smaller **BVs** possible. The removal of the backplates also removes the dominant acoustic noise sources in the device. On the other hand, in the vacuum cavity, acoustic holes in the backplate are no longer needed and the capacitance gap can be made smaller. This increases the capacitive density of the electrodes, thereby reducing the size of the transducer. In the following, the structure and design of the Air-to-Vacuum Transmission hinge Mechanism (**AVATRAM**), as well as its effect on device performance will be explained in **Chapter 2**. The fabrication process and the final designs are detailed in **Chapter 3**. Finally, first wafer-level experimental results are discussed in **Chapter 4** before ending with concluding remarks.



**Figure 1.15: Simplified schematic of the Air-to-Vacuum Transmission microphone.**

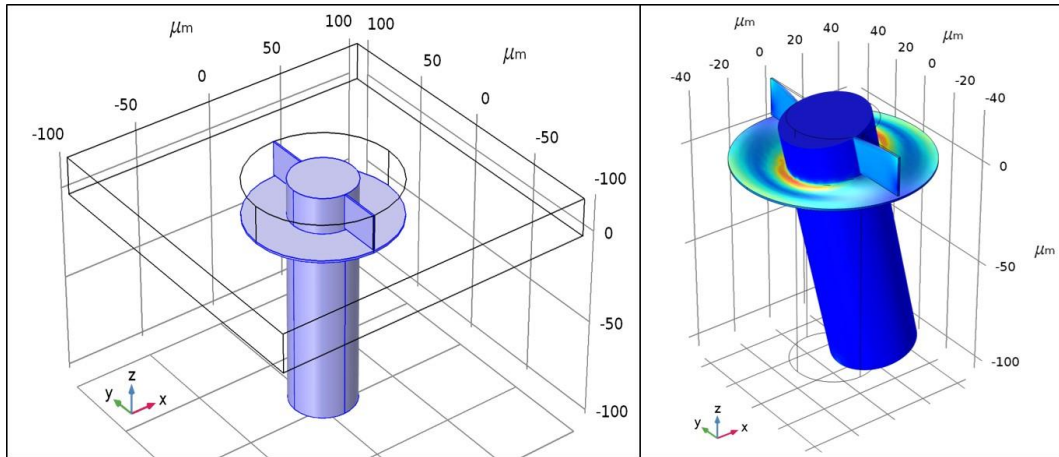
# Chapter 2 Microphone modeling

The governing concept of this new microphone design is the separation of the device into a pressure harvesting piston in air and a capacitive transducer sitting in vacuum. The transmission of the force from one atmosphere to the other is a central element on which the performance of the device hinges, both literally and figuratively. As such, the following chapter will start by the design of the Air-to-Vacuum Transmission Mechanism (**AVATRAM**) before moving on to modeling the operation of the device.

## 2.1. Air-to-vacuum transmission mechanism

The transmission hinge is designed to meet demanding and contradictory requirements imposed by the new device concept. It needs to ensure the airtightness of the cavity, be robust enough to withstand the effects of ambient pressure and of any potential pressure overshoot, while remaining flexible enough to transfer the mechanical motion. To meet these requirements, the hinge is composed of a rigid cylindrical pillar placed between the surrounding atmosphere and the vacuum cavity (**Figure 2.1**). A thin plate encircles the pillar and forms a flexible and airtight seal between the two atmospheres. Finally, on its vacuum side, two narrow torsion blades hold the pillar. On one hand, their thickness provides a high flexion stiffness, drastically reducing the pillar's out-of-plane translation. On the other hand, their small width offers a low torsion stiffness, which allows the force to still be transferred by rotating the pillar around the y-axis, despite the limitation of any out-of-plane movement. By carefully dimensioning the combination of these elements, the design of the hinge can be optimized to reach the set requirements. The main variables used in this section are summarized in **Table 2.1**.

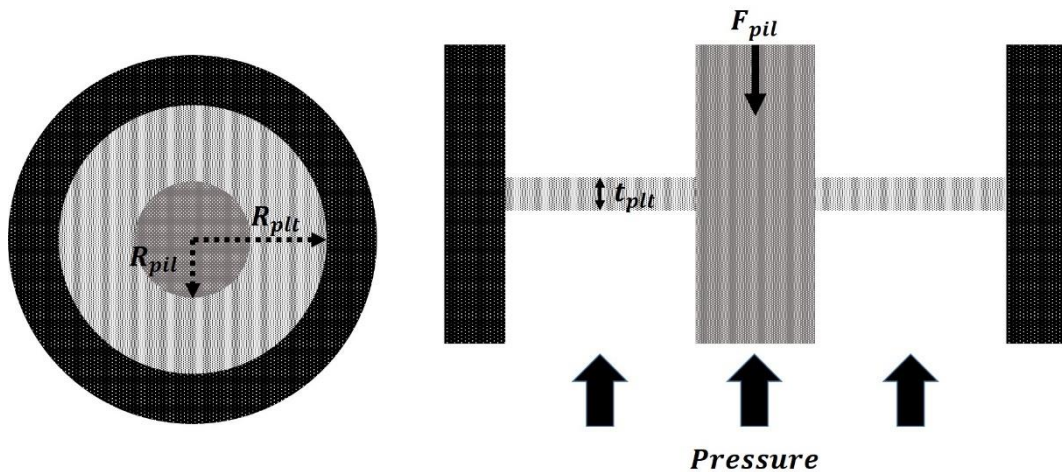




**Figure 2.1: 3D schematic of the AVATRAM (left) and simulation result showing the deformation of the structure during operation (right).**

## 2.1.1 Hinge Robustness

On its airside, the hinge is constantly subjected to the pressure of its surroundings. The hinge should therefore not only be able to withstand the effects of atmospheric pressure, but also those of possible pressure overshoots that may accidentally take place. Any applied pressure  $P$  can be considered to be uniformly applied on the airside of the hinge given its microscale. This pressure will result in a force pushing the pillar towards the vacuum cavity. The two torsion blades are then put in place to counter this effect by applying an opposing force  $F_{pil}$  to the pillar (**Figure 2.2**). For the sake of clarity, the blades have been omitted from **Figure 2.2**.



**Figure 2.2: Top and sectional schematics of the AVATRAM without torsion blades.**

In his Theory of Plates and Shells, Timoshenko proves that the bending of a circular plate subjected to a uniformly applied load in this configuration is governed by the following differential equation [78]:

$$\frac{d^3 z_{plt}}{dr^3} + \frac{1}{r} \frac{d^2 z_{plt}}{dr^2} - \frac{1}{r^2} \frac{dz_{plt}}{dr} = \frac{Q_s}{D}, \quad (2.1)$$

$z_{plt}$  being the plate's out-of-plane deflection, its vertical deformation at a given radial distance  $r$  from the center.  $D$  is the plate's flexural rigidity, given as function of its Young's modulus  $E$ , its Poisson's ratio  $\nu$ , and its thickness  $t_{plt}$ :

$$D = \frac{E}{12(1-\nu^2)} t_{plt}^3. \quad (2.2)$$

$Q_s$  is defined as the shearing force per unit length. In this case, the circular plate is symmetrically loaded and  $Q_s$  can be simply calculated by dividing the load distributed within the circle of radius  $r$  by  $2\pi r$ . As the plate is subjected to the uniformly applied pressure  $P$  and the opposing force  $F_{pil}$ ,  $Q_s$  is written:

$$Q_s = -\frac{1}{2}Pr + \frac{F_{pil}}{2\pi r}. \quad (2.3)$$

Furthermore, the differential equation can be reworked to a simpler form to solve by using the following mathematical identity:

$$\frac{d^3 z_{plt}}{dr^3} + \frac{1}{r} \frac{d^2 z_{plt}}{dr^2} - \frac{1}{r^2} \frac{dz_{plt}}{dr} = \frac{d}{dr} \left[ \frac{1}{r} \frac{d}{dr} \left[ r \frac{dz_{plt}}{dr} \right] \right]. \quad (2.4)$$

The plate's deformation is thus the result of a triple integration, and the three constants of this operation are to be found using the three following boundary conditions:

- The plate of radius  $R_{plt}$  is clamped at the pillar of radius  $R_{pil}$  and at its edge:

$$\frac{dz_{plt}}{dr} = 0 \text{ for } r = R_{pil} \text{ and } r = R_{plt}$$

- The plate is anchored at its edge:

$$z_{plt} = 0 \text{ for } r = R_{plt}$$

With these conditions, the triple integration leads to the following displacement:

$$z_{plt}(r) = \frac{\pi R_{plt}^2}{k_m} P [r_r^4 - 2(1 + \alpha^2)r_r^2 + (1 + 2\alpha^2) + 4\alpha^2 \ln r_r] - \frac{4}{k_m} F_{pil} \left[ 2r_r^2 \ln r_r + 1 - r_r^2 + \frac{2\alpha^2}{1-\alpha^2} \cdot \ln(\alpha) \cdot (r_r^2 - 1 - 2 \ln r_r) \right], \quad (2.5)$$

with:

- $k_m = \frac{16\pi E}{3(1-\nu^2)} \frac{t_{plt}^3}{R_{plt}^2}$
- $r_r = \frac{r}{R_{plt}}$
- $\alpha = \frac{R_{pil}}{R_{plt}}, \alpha \in ]0,1[.$

Furthermore, this result also gives the pillar's vertical displacement  $z_{pil}$  found for  $r = R_{pil}$  and  $r_r = \alpha$ :

$$z_{pil} = \eta_P \frac{\pi R_{plt}^2 P}{k_m} - 4\eta_f \frac{F_{pil}}{k_m}, \quad (2.6)$$

where:

- $\eta_P = [1 - \alpha^4 + 4\alpha^2 \ln \alpha]$
- $\eta_f = \left[1 - \alpha^2 - \frac{4\alpha^2}{1-\alpha^2} (\ln \alpha)^2\right]$

This parameter can later be useful to make sure that for given  $F_{pil}$  and  $P$ , the pillar's vertical movement remains very small. However, the key parameter to study for the hinge's robustness is the plate's constraint, i.e. the applied shear stress on the plate, which, as shown by Timoshenko, can be derived from its deformation:

$$\sigma(r) = \frac{E}{1-\nu^2} \frac{t_{plt}}{2} \frac{d^2 z_{plt}}{dr^2}, \quad (2.7)$$

resulting in the following expression of the stress as a function of  $r_r = r/R_{plt}$ :

$$\sigma(r_r) = \frac{1}{2} \frac{E}{1-\nu^2} \frac{t_{plt}}{R_{plt}^2} \left( 4 \frac{\pi R_{plt}^2 P}{k_m} \left[ 3r_r^2 - 1 - \alpha^2 - \frac{\alpha^2}{r_r^2} \right] - \frac{16}{k_m} F_{pil} \left[ 1 + \ln(r_r) + \frac{\alpha^2}{1-\alpha^2} \left( 1 + \frac{1}{r_r^2} \right) \ln(\alpha) \right] \right). \quad (2.8)$$

The plate will exhibit the highest stress at its clamping points, for  $r = R_{pil}$  and  $r = R_{plt}$ :

$$\begin{aligned} \sigma(\alpha) &= -\frac{3}{4} \frac{1}{\pi t_{plt}^2} \left( \pi R_{plt}^2 P [1 - \alpha^2] - 2F_{pil} \left[ -\frac{2}{1-\alpha^2} \ln(\alpha) - 1 \right] \right) \\ \sigma(1) &= \frac{3}{4} \frac{1}{\pi t_{plt}^2} \left( \pi R_{plt}^2 P [1 - \alpha^2] - 2F_{pil} \left[ 1 + \frac{2\alpha^2 \ln(\alpha)}{1-\alpha^2} \right] \right). \end{aligned} \quad (2.9)$$

To make sure it is sufficiently robust, the structure should be designed in such a way that, for a maximum applied pressure  $P_{max}$ , the stress does not surpass the plate's yield strength  $\sigma_{max}$ :

$$-\sigma_{max} < \sigma(\alpha) < \sigma_{max} \quad \text{and} \quad -\sigma_{max} < \sigma(1) < \sigma_{max}.$$

With these conditions, it is possible to find theoretical operational limits for the force applied to the pillar. It can then be easily verified that the upper limit ( $F_{upper}$ ) of  $F_{pil}$  is found from  $\sigma(\alpha) < \sigma_{max}$ , while the lower limit ( $F_{lower}$ ) is obtained from  $\sigma(1) < \sigma_{max}$ :

$$\begin{aligned} F_{upper} &= \frac{C_1 + \pi R_{plt}^2 P_{max} [1 - \alpha^2]}{2 \cdot f_{up}(\alpha)} \\ F_{lower} &= \frac{\pi R_{plt}^2 P_{max} [1 - \alpha^2] - C_1}{2 \cdot f_{low}(\alpha)}, \end{aligned} \quad (2.10)$$

where:

- $C_1 = \frac{\sigma_{max} 4\pi t_{plt}^2}{3}$

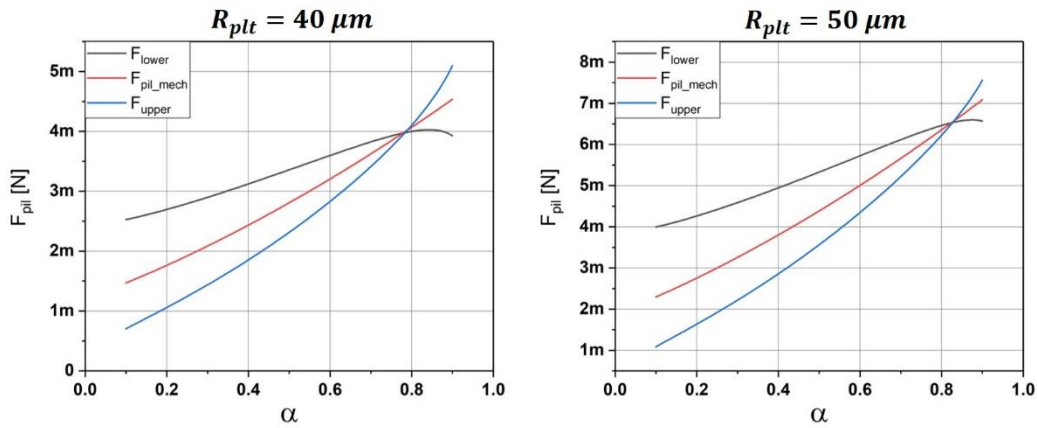
- $f_{up}(\alpha) = \frac{-2 \ln(\alpha)}{1-\alpha^2} - 1$
- $f_{low}(\alpha) = 1 + \frac{2\alpha^2 \ln(\alpha)}{1-\alpha^2}$

Consequently, in order for a hinge with plate thickness  $t_{plt}$  and radius  $R_{plt}$  to meet the robustness criteria at a given overpressure  $P_{max}$ , the pillar force must be within these theoretical limits for the chosen  $\alpha$ . However, in practice,  $F_{pil}$  is a spring force resulting from the flexural stiffness of the torsion blades opposing the out-of-plane displacement of the pillar. This means that the applicable pillar force is mechanically limited to one of a spring with infinite stiffness forcing a displacement that tends to 0. Therefore, a theoretical mechanical maximum for the pillar force can also be found by considering a pillar displacement that is sufficiently opposed to the point of becoming null. Applying this condition to **equation (2.6)**, the mechanical maximum of the pillar force  $F_{pil_{mech}}$  can be determined:

$$F_{pil_{mech}} = \frac{\eta_p}{4\eta_f} \pi R_{plt}^2 P . \quad (2.11)$$

Thus, based on the set limits of  $F_{lower} < F_{pil} < F_{upper}$  and  $F_{pil} < F_{pil_{mech}}$ , the torsion blades can be adequately designed to apply the required opposing force and ensure the robustness of the hinge.

As an example, **Figure 2.3** shows the variations of the upper, lower and  $F_{pil_{mech}}$  limits of the pillar force as a function of  $\alpha$  for a 250nm thick plate and a pressure overshoot of 10bars. Concerning the value of  $\sigma_{max}$ , although the yield strength of Silicon is 7 GPa, greatly varying measured values are reported in the literature [79]. As a practical approach in the MEMS design process, a maximum value of 1 GPa in von-Mises stress is commonly considered to make sure the yield strength is not reached [80]. However, for the design of the AVATRAM,  $\sigma_{max}$  was given an even lower value of 600 MPa, to ensure the robustness of the hinge and minimize the risks of fabrication variabilities. As a result, for a plate radius of 40  $\mu m$  and  $\alpha \in ]0; 0.78[$ , the lower limit of  $F_{pil}$  is higher than its upper limit and  $F_{pil_{mech}}$ , which



**Figure 2.3: Variations of the pillar force limits as functions of  $\alpha$  for  $t_{plt} = 250 \text{ nm}$  at different plate radii.**

means that no solutions exist for this interval. In other words, for the **AVATRAM** to withstand the effects of 10 bars of pressure, the  $R_{pil}/R_{plt}$  ratio must be higher than or equal to 0.78, so that  $F_{pil}$  can be chosen within its limits of validity. For a larger plate radius of  $50 \mu m$ , the limit of validity is found to be even higher, starting at 0.83 and reducing the validity domain of  $F_{pil}$ . This was expected, as a larger plate exhibits a lower out-of-plane stiffness, requiring a larger pillar to effectively counter the effect of the 10 bars of pressure. An increase in plate thickness at constant radius will of course lead to the opposite effect.

Finally, for any given  $(t_{plt}, R_{plt})$  couple, when the domain of validity of  $\alpha$  and the pillar force is determined, the right dimensions can be given to the torsion blades to ensure the structure's robustness. These dimensions will depend on the chosen  $F_{pil}$  and the subsequent pillar displacement  $z_{pil}$ , as the pillar force results from the blades' out-of-plane stiffness  $k_{torz}$ :

$$k_{torz} = \frac{F_{pil}}{z_{pil}}. \quad (2.12)$$

Thus, the blades should be given the right dimensions to exhibit the necessary out-of-plane stiffness, taking into account its resulting effect on the total stiffness of the hinge. In this respect, the lower limit of  $F_{pil}$  will be considered, as it corresponds to the lowest required stiffness, which, as shall be explained below, leads to a lower hinge stiffness.

## 2.1.2. Hinge stiffness

Having found the design considerations ensuring the robustness of the hinge, we can now move on to study their effects on its stiffness. The plate that encircles the pillar exhibits a very high in-plane stiffness, while the torsion blades have a high out-of-plane stiffness due to their considerable thickness. We can therefore rightfully consider that the pillar's axis of rotation lies very close to the intersection of their median planes (red dot on **Figure 2.4**). Moreover, given the symmetry of the structure, a simple 2D analysis can be sufficient to quantify its equivalent rotational stiffness ( $C_{avat}$ ).

If an external torque ( $\tau_{ext}$ ) brings about the rotation of the pillar around its axis, the movement will be opposed by the rotational stiffness of both the torsion blades  $C_{tor}$  and the plate  $C_{plt}$ . Furthermore, since the blades do not share the same center of rotation as the pillar, they will also undergo an in-plane deformation, soliciting their in-plane stiffness  $k_{torx}$ . Applying Newton's first law of rotation to the system at equilibrium gives:

$$-\tau_{ext} + (C_{tor} + C_{plt})\theta + k_{torx} \cdot \Delta x_{tor} \cdot d_{tor} = 0, \quad (2.13)$$

where  $\theta$  is the pillar's angle of rotation and  $d_{tor}$  is the distance between the centers of rotation of the blades and the pillar.  $\Delta x_{tor}$  is the torsion blades' deformation along the x-axis, which, when considering a small  $\theta$ , can be approximated by:

$$\Delta x_{tor} = d_{tor} \sin \theta = d_{tor} \theta . \quad (2.14)$$

Injecting this expression into **equation (2.13)**, we find:

$$-\tau_{ext} + (C_{tor} + C_{plt})\theta + k_{torX} \cdot d_{tor}^2 \cdot \theta = 0 . \quad (2.15)$$

The expression of the equivalent rotational stiffness of the **AVATRAM** can then be obtained:

$$C_{avat} = C_{tor} + C_{plt} + k_{torX} \cdot d_{tor}^2 . \quad (2.16)$$

It is clear from this expression that, for a given  $(t_{plt}, R_{plt})$  couple,  $C_{avat}$  is a function of two variables, the first being  $\alpha$ , as  $C_{plt}$  depends on the plate's geometry, and the second being the torsion blades' geometry giving  $C_{tor}$  and  $k_{torX}$ . Although at first glance this might seem to complicate the task of finding  $C_{avat}$ , the problem can be reduced to one of a single variable: the required  $k_{torZ}$ , based on which the blade geometry is determined, is set by the chosen pillar force (**equation (2.12)**), which itself is a function of  $\alpha$ . As we shall consequently proceed to show, by finding  $C_{tor}$  and  $k_{torX}$  as functions of  $k_{torZ}$ , the problem can be simplified and we can find  $C_{avat}$  as only a function of  $\alpha$ .

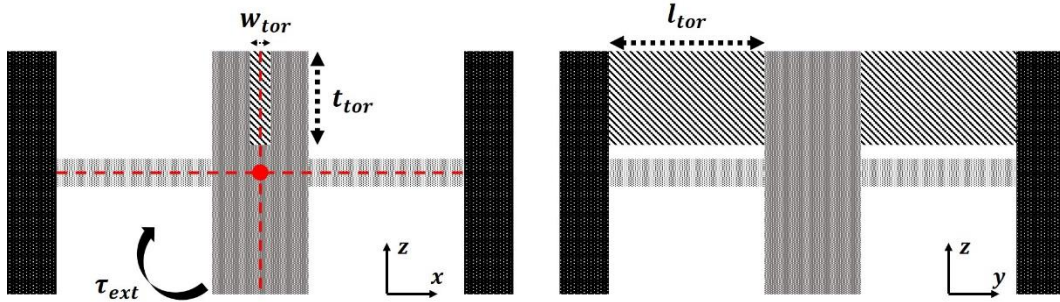
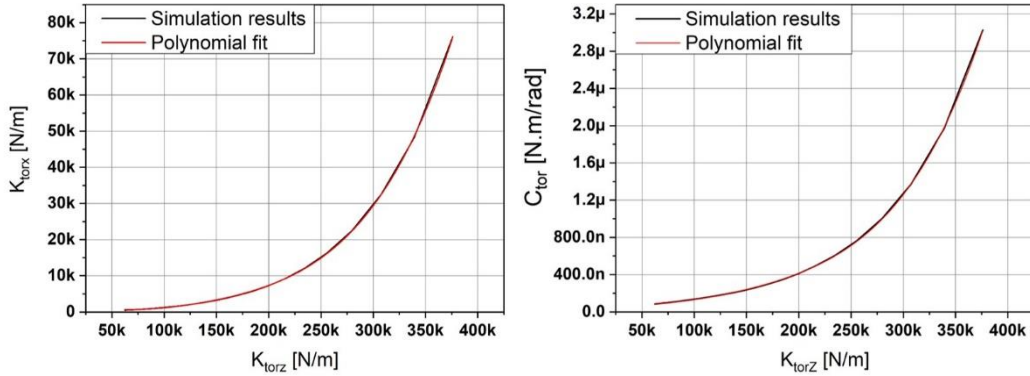


Figure 2.4: Sectional schematics of the AVATRAM with the torsion blades.

## Torsion blades' geometry

The dimensions given to the blades should serve to maximize the ratio of their out-of-plane stiffness to their torsional stiffness. As it will later be explained in **Chapter 3**, the polycrystalline Silicon blades have a thickness  $t_{tor}$  fixed at  $18 \mu\text{m}$  by the device fabrication process, leaving their width  $w_{tor}$  and their length  $l_{tor}$  as degrees of freedom. Considering that both  $C_{tor}$  and  $k_{torX}$  are proportional to  $w_{tor}^3$ , while  $k_{torZ}$  is proportional to  $w_{tor}$ , the ratio of angular rotation stiffness to out-of-plane stiffness can be minimized by giving the blades the smallest width possible. This is also fixed by the fabrication process at  $1 \mu\text{m}$ . The only remaining degree of freedom is therefore the blades' length, defining  $C_{tor}$ ,  $k_{torX}$  and  $k_{torZ}$  by the same variable  $l_{tor}$ . Furthermore, because of

their dependence on that same variable,  $C_{tor}$  and  $k_{torx}$  can be more conveniently represented as functions of  $k_{torz}$ . By doing so, for a given  $(t_{plt}, R_{plt})$  couple, the link to  $\alpha$  and the structure's robustness becomes more direct. Hence, as a first step, the three stiffness variables are found as functions of  $l_{tor}$  through finite element modeling of the two polycrystalline silicon blades. Finite element modeling using Comsol's Structural Mechanics module was preferred to analytical calculation because of its higher accuracy. As shown in **Figure 2.5**,  $C_{tor}$  and  $k_{torx}$  can then be quantified as functions of  $k_{torz}$ .



**Figure 2.5: Simulation results of the variations of  $K_{torx}$  and  $C_{tor}$  as functions of  $K_{torz}$ .**

## Plate Geometry

The rotational stiffness of the plate will depend on its geometry through the three variables  $R_{plt}$ ,  $t_{plt}$  and  $\alpha$ . For a given  $(t_{plt}, R_{plt})$  couple,  $C_{plt}$  can therefore also be found as a function of  $\alpha$  through **FEM** of monocrystalline anisotropic Silicon plate and pillar. **Figure 2.6** shows the variations of the plate's rotational stiffness for a  $(250 \text{ nm}, 45 \mu\text{m})$  couple, in keeping with the example given earlier to illustrate the robustness requirement. As expected, the stiffness is lowest for the smallest valid  $\alpha$ , as the flexible part of the plate is at its largest.



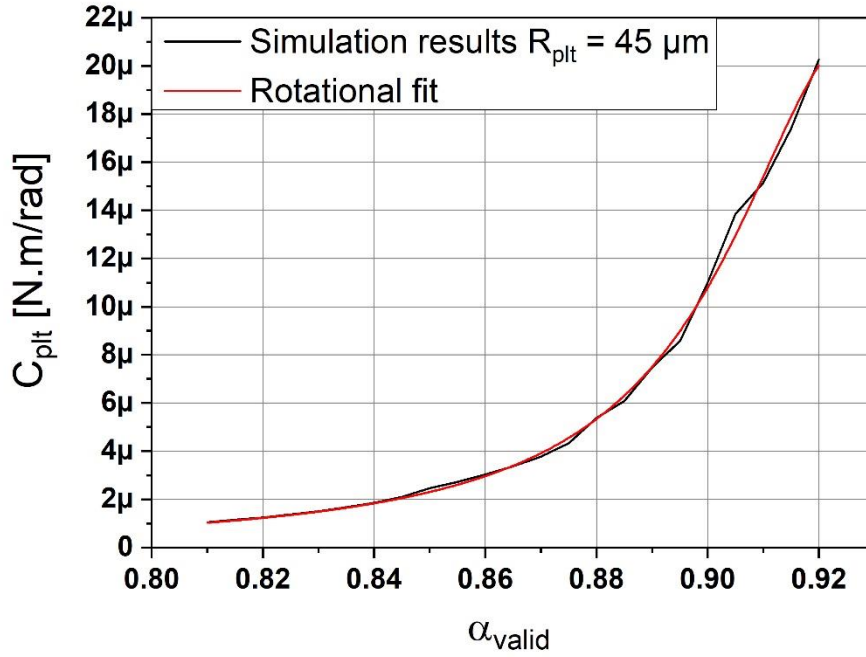


Figure 2.6: Variation of the plate's rotational stiffness as a function of  $\alpha$  in its domain of validity for  $t_{\text{plt}} = 250 \text{ nm}$  and  $R_{\text{plt}} = 45 \mu\text{m}$ .

## Equivalent rotational stiffness

Finding the equivalent rotational stiffness of the structure can now be divided into two steps. First, for each  $\alpha$  in the validity domain, the pillar force is chosen in accordance to the acceptable pillar displacement at the considered pressure overshoot. This will define the required  $k_{\text{torz}}$ , which will in turn set the length of the torsion blades as well as  $C_{\text{tor}}$  and  $k_{\text{torx}}$ . In the following calculations, the lower limit  $F_{\text{lower}}$  of the pillar force was chosen as it determines the lowest  $k_{\text{torz}}$  for the acceptable pillar displacement, which then leads to the lowest  $C_{\text{tor}}$ ,  $k_{\text{torx}}$  and  $C_{\text{avat}}$ . Second, the equivalent stiffness can then be calculated for each valid  $\alpha$  from the previously found values of  $C_{\text{tor}}$ ,  $k_{\text{torx}}$  and  $C_{\text{plt}}$ . This can be done for any given  $(t_{\text{plt}}, R_{\text{plt}})$  couple, as evidenced by **Figure 2.7**, which further shows that the structure can be designed to exhibit a very low rotational stiffness of only a few  $\mu\text{N} \cdot \text{m}/\text{rad}$ .

For a small plate thickness of  $250 \text{ nm}$ , the equivalent stiffness takes the shape of a bell, starting with an abrupt decrease very close to the start of the validity range, followed by an almost exponential increase with the increasing  $\alpha$ . This is explained by the fact that, at the very start of the validity range, the lower limit of  $F_{\text{pil}}$ , chosen for determining  $k_{\text{torz}}$ , is almost equal to the theoretical mechanical maximum of the pillar force  $F_{\text{pil}_{\text{mech}}}$  that would lead to no pillar displacement (**Figure 2.3**). Therefore, the pillar displacement resulting from the  $F_{\text{pil}}$  chosen in this region is very small and requires a very high out-of-plane stiffness. In turn, the torsion blade geometry exhibiting the necessary  $k_{\text{torz}}$  will also exhibit high  $C_{\text{tor}}$  and  $k_{\text{torx}}$  (**Figure 2.5**), thereby greatly increasing the equivalent rotational stiffness.



However, as  $\alpha$  increases, the lower limit of  $F_{pil}$  becomes lower than  $F_{pil_{mech}}$ , decreasing the blade stiffness to the point that  $C_{avat}$  becomes mostly determined by the rotational stiffness of the plate, and follows the trend of  $C_{plt}$  (**Figure 2.7**). Interestingly, this effect is not observed for higher plate thicknesses, as the stress at the plate's clamping points  $\sigma(1)$  and  $\sigma(\alpha)$  is inversely proportional to  $t_{plt}^2$ . Hence, throughout the validity range, the stress remains lower than  $\sigma_{max}$  for small pillar forces and low torsion blade stiffnesses. Nevertheless, all these results show that, no matter the considered  $(t_{plt}, R_{plt})$  couple, the **AVATRAM** can be designed to meet the requirements of robustness and flexibility.

#### AVATRAM VARIABLES

$R_{pil}$	Pillar radius
$R_{plt}$	Plate radius
$t_{plt}$	Plate thickness
$z_{pil}$	Pillar out-of-plane displacement
$F_{pil}$	Applied pillar force
$\alpha$	$R_{pil}/R_{plt}$
$l_{tor}$	Torsion blade length
$w_{tor}$	Torsion blade width
$t_{tor}$	Torsion blade thickness
$k_{torZ}$	Torsion blade stiffness z-direction
$k_{torX}$	Torsion blade stiffness x-direction
$d_{tor}$	Distance between the centers of rotation of the blades and the pillar
$C_{tor}$	Torsion blade rotational stiffness
$C_{plt}$	Plate rotational stiffness
$C_{avat}$	AVATRAM total rotational stiffness

Table 2.1: AVATRAM main variables.

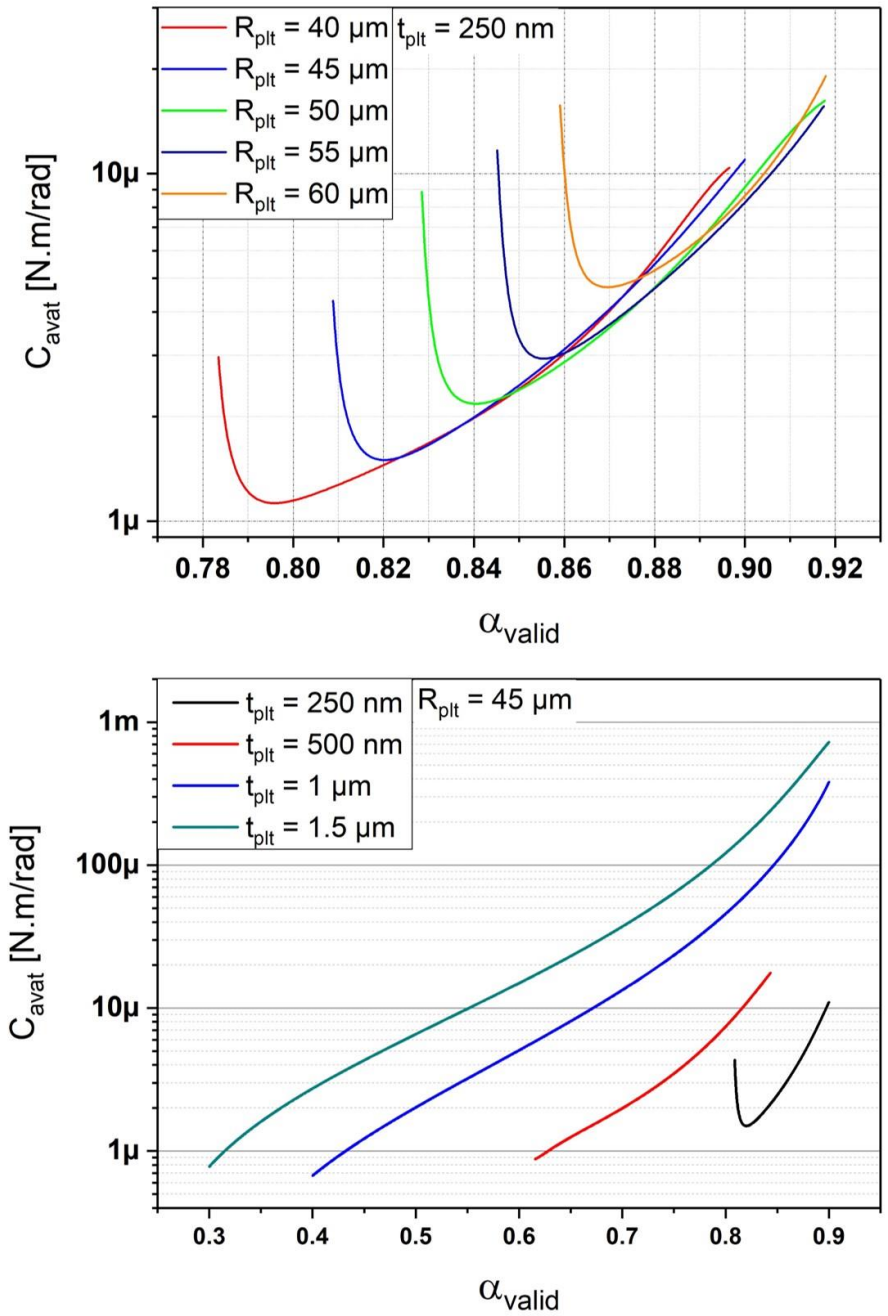


Figure 2.7: Variations of the AVATRAM's equivalent stiffness as a function of valid  $\alpha$  for different plate radii at  $t_{plt} = 250$  nm (top) and different plate thicknesses at  $R_{plt} = 45\ \mu\text{m}$  (bottom).

## 2.2. Microphone model

In this section, a lumped elements model is developed to study the properties of the microphone, given the complexity of its structure and the strong interdependence of different physics. The model describes the acoustic and mechanical properties of the device through equivalent circuit elements based on conjugate power variables. Generally, two conjugate power variables are defined, an *effort* and a *flow*. Each energy domain is represented by its own set of variables, to which a variable of *displacement* can also be associated (**Table 2.2**). As a result, different energy domains can be described by the same generalized circuit elements. In the following, the lumped elements model is developed by studying each part of the microphone structure separately before combining all elements into one equivalent circuit. We note that this is done based on an impedance analogy, where the impedance is defined as the ratio of the applied *effort* to the resulting *flow*. The main variables used in this section are summarized in **Table 2.4**.

Energy Domain	Effort	Flow	Displacement
<b>Mechanical Translation</b>	Force [ $N$ ]	Velocity [ $m/s$ ]	Position [ $m$ ]
<b>Mechanical Rotation</b>	Torque [ $N.m$ ]	Angular Velocity [ $rad/s$ ]	Angle [ $rad$ ]
<b>Electrical</b>	Voltage [ $V$ ]	Current [ $A$ ]	Charge [ $C$ ]
<b>Acoustic</b>	Pressure [ $Pa$ ]	Volumetric flow [ $m^3/s$ ]	Volume [ $m^3$ ]

Table 2.2: Conjugate power variables relative to each energy domain.

### 2.2.1. Electrostatic transduction

The microphone's electrostatic transducer is a simple structure composed of a movable electrode sandwiched between top and bottom counter-electrodes for differential operation, all sitting in a vacuum environment. Even though it is connected to the rotating **AVATRAM**, the assumption is made that the electrode moves in complete out-of-plane translation (**Figure 2.8**). With this initial hypothesis, the operation of the electrostatic transduction can be studied separately, which simplifies the study of the entire system. The details of how the translational

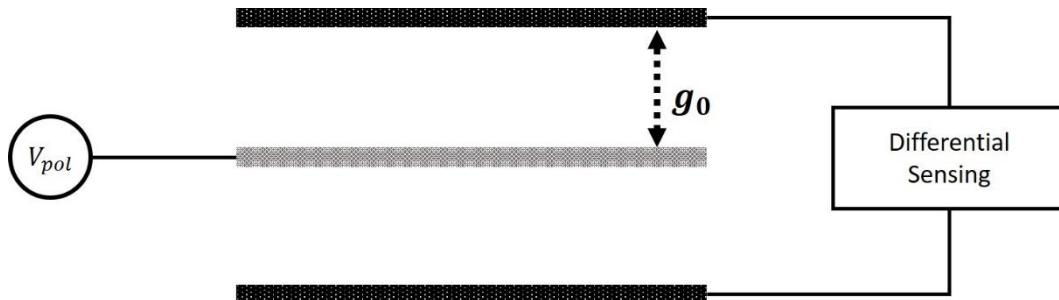


Figure 2.8: Simplified schematic of the differential capacitor.

movement of the electrode is mechanically decoupled from the rotational movement of the **AVATRAM** are discussed later in **Chapter 3**.

Under a fixed difference of potential  $U_{pol}$ , each side of the movable electrode forms a capacitor with the counter-electrode opposite to it, with a capacitance  $C_{el}$  and a stored potential energy  $E_{el} = C_{el}U_{pol}^2/2$ . It therefore follows that any variation of this energy due to a gap variation  $dg$  of the electrode leads to the following electrostatic force:

$$F_e = \frac{1}{2} \frac{dC}{dg} U_{pol}^2 . \quad (2.17)$$

The capacitance resulting from the gap change is then written:

$$C = \varepsilon_0 \frac{A_{el}}{g_0 + dg} = C_{el} \frac{1}{1 + \frac{dg}{g_0}} , \quad (2.18)$$

where  $g_0$  is the initial gap and  $A_{el}$  is the overlap surface of the electrodes. For a very small gap variation, the expression can be expanded to a second order Maclaurin series:

$$C \approx \varepsilon_0 \frac{A_{el}}{g_0} \left( 1 - \frac{dg}{g_0} + \left( \frac{dg}{g_0} \right)^2 \right) = C_{el} \left( 1 - \frac{dg}{g_0} + \left( \frac{dg}{g_0} \right)^2 \right) . \quad (2.19)$$

Differentiating  $C$  by  $dg$  and injecting the resulting expression into **equation (2.17)**, we find the first orders of the electrostatic force:

$$F_e = -\varepsilon_0 A_{el} \frac{U_{pol}^2}{2g_0^2} + \varepsilon_0 A_{el} \frac{U_{pol}^2 dg}{g_0^3} = F_{elec} + F_{soft} . \quad (2.20)$$

Thus, the first two orders of the electrostatic force applied to the moving electrode are equivalent to a constant and attractive force  $F_{elec}$  and an attractive spring force  $F_{soft}$  with a negative stiffness marking the electrostatic spring softening effect. Consequently, under differential operation, the moving electrode will be subjected to two opposite electrostatic forces, one from each capacitor, on its top and bottom surfaces. On one hand, as both surfaces and initial gaps are assumed to be equal, this serves to eliminate the effect of the attractive forces  $F_{elec}$ . On the other hand, this compounds the effect of the attractive spring forces. Considering that the electrode is held by spring structures of combined stiffness  $k_{sprg-e}$ , we write the resulting sum of external forces applied to the electrode:

$$\begin{aligned} \sum F_{ext-e} &= \varepsilon_0 A_{el} \frac{U_{pol}^2}{g_0^3} dg - \varepsilon_0 A_{el} \frac{U_{pol}^2}{g_0^3} (-dg) - k_{sprg-e} dg \\ &= (2k_{neg} - k_{sprg-e}) dg , \end{aligned} \quad (2.21)$$

where  $k_{neg} = \varepsilon_0 A_{el} \frac{U_{pol}^2}{g_0^3}$ . Thus, in order for the electrode to operate in a stable fashion, the combined spring stiffness must be equal to or higher than the combined spring softening effect.

## 2.2.2. Acoustic Sensing

The acoustic sensing element of the device is the rigid piston placed in air and sitting on top of the **BV**. Narrow slits all around its perimeter free the piston from the surrounding substrate and create an acoustic path towards the **BV**. Furthermore, similar to the electrode, the piston is assumed to have a completely translational out-of-plane movement, mechanically decoupled from the **AVATRAM**'s rotation. This also allows the study of the acoustic sensing element separately. For the following, **Figure 2.9** is used as a reference for all geometrical quantities. The mechanical decoupling is not represented, but takes place at the end of the connections of the **AVATRAM** to the piston and the moving electrode.

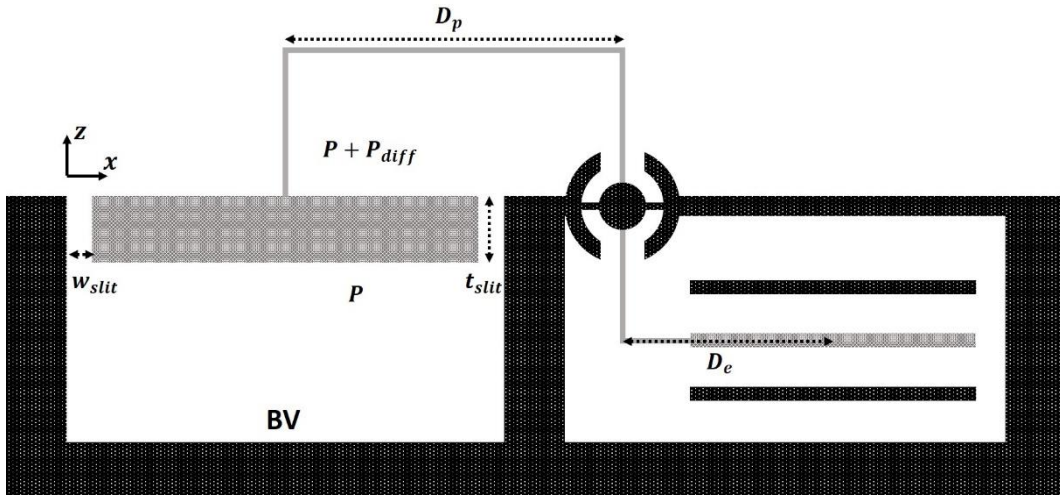


Figure 2.9: Geometric device schematic.

### Airflow rate

When an acoustic wave impinges on the device, it applies a pressure difference  $P_{diff}$  between the two faces of the piston, setting it in motion. In this configuration, the resulting total airflow rate  $q_{tot}$  into the **BV** will simply be the sum of two parts. The first part is due to the mechanical movement of the piston displacing air into the **BV** at the piston's speed  $v_{pist}$ :

$$q_{pist} = A_{pist} v_{pist} , \quad (2.22)$$

where  $A_{pist}$  is the surface area of the piston. The second part is due to the air flowing through the narrow slits due to the imposed pressure difference and the piston's movement. One side of the slits is formed by the piston and moves at its speed while the other side is formed by the stationary substrate. This is the case of combined Poiseuille and Couette flows, for which the Navier-Stokes equation simplifies to [16]:

$$\mu \frac{\partial^2 v_z(x,z)}{\partial x^2} = \frac{\partial P}{\partial z} , \quad (2.23)$$

where  $\mu$  is the viscosity of air and  $v_z$  is the speed of air in the out-of-plane direction. The speed of air is then obtained by integrating twice over  $x$  and applying the following two boundary conditions:

- $v_z(x = 0) = 0$  (at the border with the stationary wall)
- $v_z(x = w_{slit}) = v_{pist}$  (at the border with the side of the piston for a slit width  $w_{slit}$ )

This leads to the following air speed expression:

$$v_z(x, z) = \frac{1}{2\mu} \frac{\partial P}{\partial z} (x^2 - w_{slit}x) + \frac{v_{pist}}{w_{slit}} x. \quad (2.24)$$

The airflow rate resulting from this air speed can then be obtained by an integration over the open surface of the slits. With a piston perimeter  $p_{pist}$ , this gives:

$$\begin{aligned} q_{slit}(z) &= \int_0^{p_{pist}} \int_0^{w_{slit}} v_z(x, z) dx dy \\ &= -\frac{1}{12\mu} \frac{\partial P}{\partial z} w_{slit}^3 p_{pist} + v_{pist} \frac{w_{slit} p_{pist}}{2}. \end{aligned} \quad (2.25)$$

The mean flow rate over the entire thickness of the slits  $t_{slit}$  is given by definition as

$$q_{slit} = \frac{1}{t_{slit}} \int_0^t q_{slit}(z) dz, \quad (2.26)$$

giving the rate of air flowing through the slits:

$$q_{slit} = \frac{1}{12\mu} P_{diff} w_{slit}^3 \frac{p_{pist}}{t_{slit}} + v_{pist} \frac{w_{slit} p_{pist}}{2}, \quad (2.27)$$

We can finally write the total airflow rate resulting from an impinging sound wave:

$$\begin{aligned} q_{total} &= A_{pist} v_{pist} + \frac{1}{12\mu} P_{diff} w_{slit}^3 \frac{p_{pist}}{t_{slit}} + v_{pist} \frac{w_{slit} p_{pist}}{2} \\ q_{total} &= A_{pist}^* v_{pist} + \frac{P_{diff}}{R_{slit}}, \end{aligned} \quad (2.28)$$

where  $A_{pist}^* = A_{pist} + \frac{w_{slit} p_{pist}}{2}$  and  $R_{slit} = 12\mu \frac{t_{slit}}{w_{slit}^3 p_{pist}}$ . It can clearly be noticed from this final expression that the total airflow is divided into two separate parts. The circuit equivalent of this situation is a separation into two parallel circuit branches: a slits branch in which the flow  $q_{slit}$ , representing the leaks all around the piston due to the effort  $P_{diff}$ , encounters a resistance  $R_{slit}$ , and a mechanical branch with a flow  $q_{pist}$  due to the mechanical motion of the piston. The components of the mechanical branch are then to be found by studying the mechanical motion of the entire moving structure, i.e. the piston connected to the electrode via the **AVATRAM**.

## Mechanics of the moving structure

The fixed-axis rotation of the **AVATRAM** imposes a balance scale configuration, connecting the acoustic sensing piston in air to the capacitive transducer in vacuum. Both the piston and the electrode have a completely translational out-of-plane movement, and are connected to the **AVATRAM** pillar through lever arms that are supposed mechanically undeformable. Furthermore, due to the balance scale configuration, the electrode moves in the opposite direction to the piston. Thus, when applied to the rotation of the hinge, Newton's second law of motion for rotation gives:

$$\tau_{pist} + \tau_{elec} - C_{avat} \cdot \theta = I_{tot} \cdot \ddot{\theta}, \quad (2.29)$$

where  $C_{avat}$  is the rotational stiffness of the hinge,  $I_{tot}$  the total moment of inertia, and  $\theta$  and  $\ddot{\theta}$  the angle of rotation and the angular acceleration respectively. The torques  $\tau_{pist}$  and  $\tau_{elec}$  result from the forces applied to the piston and the electrode:

$$\sum F_{ext-p} \cdot D_p - \sum F_{ext-e} \cdot D_e - C_{avat} \cdot \theta = I_{tot} \cdot \ddot{\theta}, \quad (2.30)$$

where  $D_p$  and  $D_e$  are the distances from the center of rotation (center of the hinge) to the centers of the piston and the electrode respectively. The external forces acting on the electrode have been previously identified, while by analyzing the piston's movement, we find that it is subjected to three external forces: a drag force, a pressure force and a spring force.

The drag force results from the shear stress of the air moving in the narrow slits and acting on the piston. The shear stress resulting from the airflow is quantified by:

$$\sigma_{air} = -\mu \frac{\partial v_z(x=w_{slit})}{\partial x}, \quad (2.31)$$

The partial derivative of  $v_z$  by  $x$  can be obtained from **equation (2.24)**, which, by replacing  $x$  by  $w_{slit}$  gives:

$$\frac{\partial v_z}{\partial x}(x = w_{slit}) = \frac{1}{2\mu} \frac{\partial P}{\partial z} w_{slit} + \frac{v_{pist}}{w_{slit}}, \quad (2.32)$$

Therefore:

$$\sigma_{air} = -\frac{1}{2} \frac{\partial P}{\partial z} w_{slit} - \mu \frac{v_{pist}}{w_{slit}}. \quad (2.33)$$

By integrating the shear stress over the contact surface between the piston sides and the air in the slits, we can obtain the total drag force:

$$F_{drag} = -\frac{P_{diff}}{2} w_{slit} p_{pist} - \mu v_{pist} t_{slit} \frac{v_{pist}}{w_{slit}}. \quad (2.34)$$

The pressure force resulting from the applied pressure difference at the surface of the piston is the one that mainly brings about the motion of the piston:

$$F_{pres} = -P_{diff}A_{pist} . \quad (2.35)$$

As for the spring force, similarly to the electrode, the piston is held by spring structures of combined stiffness  $k_{sprg-p}$  resulting in a force opposing the out-of-plane displacement of the piston  $z_p$ :

$$F_{sprg} = -k_{sprg-p}z_p . \quad (2.36)$$

Finally, by inserting the expressions of the external forces into **equation (2.30)** we find the structure's explicit equation of motion:

$$D_p \cdot \left( -\frac{P_{diff}}{2} w_{slit} p_{pist} - \mu v_{pist} t_{slit} \frac{p_{pist}}{w_{slit}} - P_{diff} A_{pist} - k_{sprg-p} \cdot z_p \right) - D_e \cdot (-k_{rem} \cdot z_e) - C_{avat} \cdot \theta = I_{tot} \cdot \ddot{\theta} , \quad (2.37)$$

where  $k_{rem} = -(2k_{neg} - k_{sprg-e})$  and  $z_e$  is the electrode's out-of-plane displacement. In the limits of the small angle approximation, the following identities can be considered as true:  $\theta = -\frac{z_e}{D_e} = +\frac{z_p}{D_p}$  and  $\ddot{\theta} = -\ddot{z}_e/D_e$ , where  $\ddot{z}_e$  is the out-of-plane acceleration of the electrode. With  $\gamma = D_p/D_e$ , and dividing **equation (2.37)** by  $D_p$  we find:

$$\left( -\frac{P_{diff}}{2} w_{slit} p_{pist} - \mu t_{slit} v_{pist} \frac{p_{pist}}{w_{slit}} - P_{diff} A_{pist} + k_{sprg-p} \cdot \gamma z_e \right) + (k_{rem} \cdot z_e) \frac{1}{\gamma} + C_{avat} \cdot \frac{z_e}{D_p D_e} = -I_{tot} \cdot \frac{\ddot{z}_e}{D_p D_e} . \quad (2.38)$$

Which gives:

$$-P_{diff} A_{pist}^* = \mu t_{slit} v_{pist} \frac{p_{pist}}{w_{slit}} - \left( \gamma k_{sprg-p} + \frac{k_{rem}}{\gamma} + \frac{C_{avat}}{D_p D_e} \right) z_e - \frac{I_{tot}}{D_p D_e} \ddot{z}_e , \quad (2.39)$$

As we have previously shown, the flow rate in the mechanical branch is  $q_{pist} = A_{pist}^* v_{pist} = -A_{pist}^* \gamma \dot{z}_e$ . Inserting the expressions of  $z_e$  and its first and second time derivatives into the equation of motion gives:

$$-P_{diff} = \mu t_{slit} \frac{p_{pist}}{w_{slit}} \frac{q_{pist}}{A_{pist}^*} + \left( k_{sprg-p} + \frac{k_{rem}}{\gamma^2} + \frac{C_{avat}}{D_p^2} \right) \frac{1}{A_{pist}^*} \int q_{pist} + \frac{I_{tot}}{(D_p A_{pist}^*)^2} \dot{q}_{pist} . \quad (2.40)$$

Finally, we have reached an equation that links the acoustic *flow* due to the mechanical motion  $q_{pist}$  to the applied acoustic *effort*  $P_{diff}$ . The circuit equivalent of this branch can thus be modeled by three electrical components:

- An inductor (inertia):  $L_{mecha} = \frac{I_{tot}}{(D_p A_{pist}^*)^2}$



- A capacitor (mechanical compliance):  $C_{mecha} = \frac{A_{pist}^{*2}}{\left(k_{sprg-p} + \frac{k_{rem}}{\gamma^2} + \frac{C_{avat}}{D_p^2}\right)}$
- A resistance (damping):  $R_{mecha} = \mu t_{slit} \frac{p_{pist}}{w_{slit} A_{pist}^*} \frac{1}{2}$

It is also possible to retrieve the displacement  $z_e$  of the electrode during its movement by considering again the flow rate in the mechanical branch. On one hand, we have previously shown that this flow is linked to the speed of the electrode via  $q_{pist} = -A_{pist}^* \gamma \dot{z}_e$ . On the other hand, the flow is also integrated by the capacitor  $C_{mecha}$  of the branch:

$$\Delta P_{C_{mecha}} = \frac{1}{C_{mecha}} \int q_{pist} \text{ and } z_e = \int \frac{q_{pist}}{\gamma A_{pist}^*}, \quad (2.41)$$

giving:

$$z_e = \Delta P_{C_{mecha}} \frac{A_{pist}^*}{\gamma \left(k_{sprg-p} + \frac{k_{rem}}{\gamma^2} + \frac{C_{avat}}{D_p^2}\right)}. \quad (2.42)$$

The movement of the electrode will lead to a variation of charge along its top ( $\Delta Q_{top}$ ) and bottom ( $\Delta Q_{bot}$ ) counter-electrodes. At a constant polarization voltage, this variation is written:

$$\Delta Q_{top} = \Delta C_{top} U_{pol} \text{ and } \Delta Q_{bot} = \Delta C_{bot} U_{pol}. \quad (2.43)$$

The variations of capacitances  $\Delta C_{top}$  and  $\Delta C_{bot}$  can be obtained from **equation (2.18)** and its Maclaurin series expansion limited to the first order and replacing  $dg$  by  $z_e$ :

$$\Delta C_{top} \approx C_{el} \frac{z_e}{g_0} \text{ and } \Delta C_{bot} \approx -C_{el} \frac{z_e}{g_0}. \quad (2.44)$$

Plugging these expressions into **equations (2.43)** gives:

$$\Delta Q_{top} = C_{el} \frac{z_e}{g_0} U_{pol} \text{ and } \Delta Q_{bot} = -C_{el} \frac{z_e}{g_0} U_{pol}. \quad (2.45)$$

Finally, when  $z_e$  is replaced by its expression given by **equation (2.42)**, we can find a relation between  $\Delta P_{C_{mecha}}$  and the charge variations:

$$\begin{aligned} \frac{\Delta Q_{top}}{C_{el}} &= \frac{A_{pist}^* U_{pol}}{\gamma g_0 \left(k_{sprg-p} + \frac{k_{rem}}{\gamma^2} + \frac{C_{avat}}{D_p^2}\right)} \Delta P_{C_{mecha}} \text{ and} \\ -\frac{\Delta Q_{bot}}{C_{el}} &= \frac{A_{pist}^* U_{pol}}{\gamma g_0 \left(k_{sprg-p} + \frac{k_{rem}}{\gamma^2} + \frac{C_{avat}}{D_p^2}\right)} \Delta P_{C_{mecha}}. \end{aligned} \quad (2.46)$$

We note that  $\Delta Q_{top}/C_{el}$  and  $-\Delta Q_{bot}/C_{el}$  are the variations of voltage resulting from the variations of capacitance. Thus, **equations (2.46)** relate between an acoustic *effort* and an electrical one. This passage from one energy domain to the other is commonly modeled by a transformer with a *turns ratio*  $n$ :

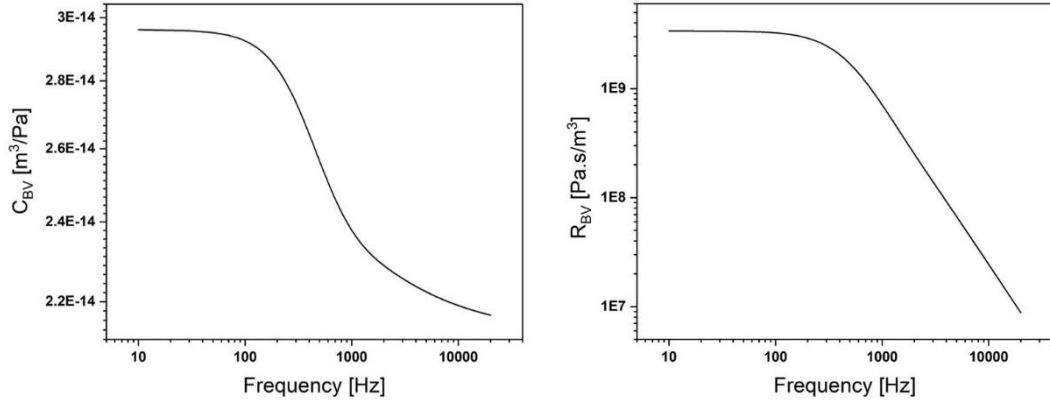
$$n = \frac{A_{pist}^* U_{pol}}{\gamma g_0 \left( k_{sprg-p} + \frac{k_{rem}}{\gamma^2} + \frac{C_{cavat}}{D_p^2} \right)}. \quad (2.47)$$

### 2.2.3. Back Volume Impedance

The final element in the acoustic airflow path is the **BV**. As explained in **Appendix B**, this back cavity adds an acoustic impedance to the acoustic *flow*  $q_{total}$  generated by the effort  $P_{diff}$ . Since it is a closed volume, the cavity exhibits a compliance  $C_{BV}$ , which represents the volume that it can accommodate at a certain pressure. However, when thermal dissipation effects along the sides of the cavity are considered,  $C_{BV}$  becomes a function of the signal frequency, and the cavity is found to exhibit an additional dissipative element  $R_{BV}$ . The impedance of the **BV** is therefore composed of a capacitive part and a resistive part:

$$P_{diff} = \frac{1}{C_{BV}} \int q_{total} + R_{BV} q_{total}. \quad (2.48)$$

The analytical and numerical calculation of the **BV**'s impedance are detailed in **Appendix B**. It is found to depend on both the size of the **BV** and the depth of the cavity. **Figure 2.10** displays the variations of the compliance and resistance of the **BV** as functions of the signal frequency.

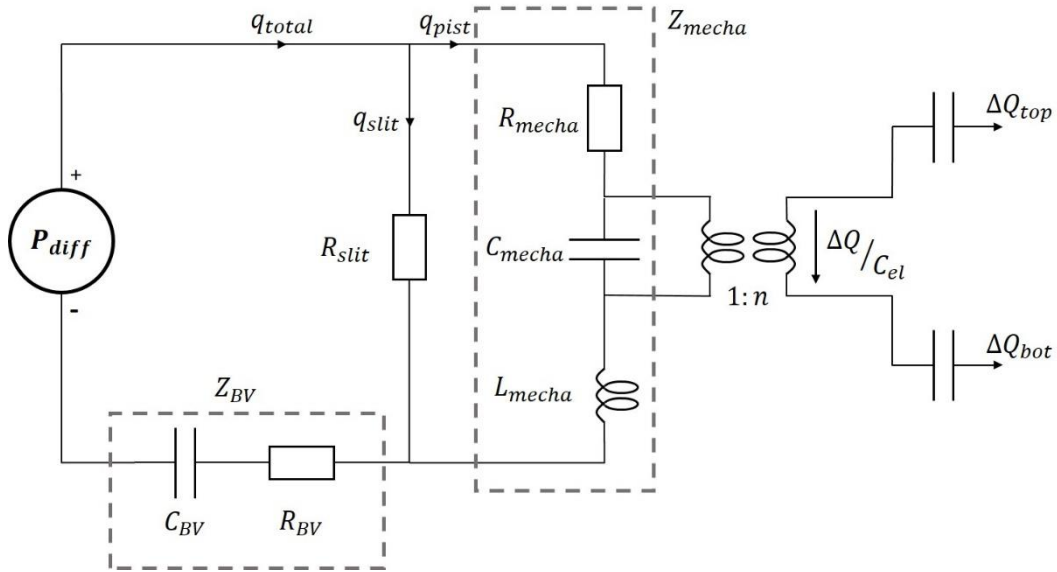


**Figure 2.10: Variations of the BV resistance and compliance as functions of the frequency for 300  $\mu\text{m}$  deep BV of 3  $\text{mm}^3$  in the 1D-model approximation**

### 2.2.4. Lumped Elements Model

Now that each part of the microphone has been studied, the equivalent circuit can be constructed based on the relations found between *effort* and *flow* for each energy domain. Referring to **Figure 2.11**, the airflow generated by the pressure difference is divided into two parts, the first of which goes through slits surrounding the piston encountering a resistance  $R_{slit}$ . The second part brings about the motion of the entire mechanical structure, represented by a damped spring-self system. The

resulting motion of the electrode is then transformed into a variation of charges in the electrical branch. Finally, both parts of the airflow rejoin and feed through the **BV** impedance. **Table 2.3** gives a summary of the expressions of all lumped elements used in this microphone model.



**Figure 2.11: Equivalent circuit of the lumped elements model.**

Lumped element	Expression
$R_{slit}$	$12\mu \frac{t_{slit}}{w_{slit}^3 p_{pist}}$
$R_{mecha}$	$\mu t_{slit} \frac{p_{pist}}{w_{slit}} \frac{1}{A_{pist}^{*2}}$
$C_{mecha}$	$\frac{A_{pist}^{*2}}{\left(k_{sprg-p} + \frac{k_{rem}}{\gamma^2} + \frac{C_{avat}}{D_p^2}\right)}$
$L_{mecha}$	$\frac{I_{tot}}{(D_p A_{pist}^*)^2}$
$R_{BV}$	Numerically calculated ( <b>Appendix B</b> )
$C_{BV}$	Numerically calculated ( <b>Appendix B</b> )
$n$	$\frac{A_{pist}^* U_{pol}}{\gamma g_0 \left(k_{sprg-p} + \frac{k_{rem}}{\gamma^2} + \frac{C_{avat}}{D_p^2}\right)}$

**Table 2.3: Summary of the expressions of all lumped elements used in the microphone model.**

## Transfer function

The equivalent circuit obtained by the lumped elements approach simplifies the study of the microphone's response. The entire system can be analyzed based on basic circuit analysis techniques. These techniques are used to find the microphone's transfer function and its resultant sensitivity. Taking **Figure 2.11** as a reference, the total flow  $q_{total}$ , generated by the pressure difference  $P_{diff}$ , is divided into  $q_{slit}$  and  $q_{pist}$  which feed through the impedances  $R_{slit}$  and  $Z_{mecha}$  respectively. As a consequence to this division of airflow,  $q_{pist}$  is quantified by:

$$q_{pist} = \frac{R_{slit}}{Z_{mecha} + R_{slit}} q_{total} . \quad (2.49)$$

The total airflow depends on the equivalent impedance of the device  $Z_{equ}$

$$q_{total} = \frac{P_{diff}}{Z_{equ}} = \frac{(Z_{mecha} + R_{slit})}{Z_{mecha}R_{slit} + Z_{BV}(Z_{mecha} + R_{slit})} P_{diff} . \quad (2.50)$$

Plugging the expression of  $q_{tot}$  into **equation (2.49)** we find:

$$q_{pist} = \frac{R_{slit}}{Z_{mecha}R_{slit} + Z_{BV}(Z_{mecha} + R_{slit})} P_{diff} . \quad (2.51)$$

This flow is linked to the (imagined) pressure difference acting on the moving structure  $\Delta P_{C_{mecha}}$  via

$$\Delta P_{C_{mecha}} = q_{pist} \frac{1}{sC_{mecha}} , \quad (2.52)$$

where  $s$  is the complex frequency in the Laplace domain, which leads to the relation between  $P_{diff}$  and  $\Delta P_{C_{mecha}}$ :

$$\Delta P_{C_{mecha}} = \frac{R_{slit}}{Z_{mecha}R_{slit} + Z_{BV}(Z_{mecha} + R_{slit})} \frac{1}{sC_{mecha}} P_{diff} . \quad (2.53)$$

Moreover, the pressure acting on the moving structure leads to the variation of charges  $\Delta Q$  as shown by equations (2.46). We can thus find the transfer function giving the output of the microphone in terms of variation of charges at a given pressure difference:

$$\Delta Q = \frac{sC_{mecha}C_{el}U_{pol}}{\gamma g_0 A_{pist}^*} \cdot \frac{R_{slit}}{Z_{mecha}R_{slit} + Z_{BV}(Z_{mecha} + R_{slit})} \cdot \frac{1}{sC_{mecha}} P_{diff} = H_{P \rightarrow \Delta Q} P_{diff} , \quad (2.54)$$

By developing and factorizing the different impedances, the expression of  $H_{P \rightarrow \Delta Q}$  can be simplified to

$$H_{P \rightarrow \Delta Q} = \frac{sR_{slit}C_{BV}C_{mecha}C_{el}U_{pol}}{\gamma g_0 A_{pist}^*} \cdot \frac{1}{1 + s\eta_1 + s^2\eta_2 + s^3\eta_3} , \quad (2.55)$$

where

- $\eta_1 = R_{slit}C_{BV} + R_{BV}C_{BV} + R_{mecha}C_{mecha} + R_{slit}C_{mecha}$

- $\eta_2 = R_{slit}R_{mecha}C_{mecha}C_{BV} + R_{BV}R_{mecha}C_{mecha}C_{BV} + R_{BV}R_{slit}C_{mecha}C_{BV} + L_{mecha}C_{mecha}$
- $\eta_3 = R_{slit}L_{mecha}C_{mecha}C_{BV} + R_{BV}L_{mecha}C_{mecha}C_{BV}$

As we will proceed to demonstrate later in this chapter, the slit resistance  $R_{slit}$  is much higher than the two other resistances, leading to the following simplifications:

- $\eta_1 \approx R_{slit}(C_{BV} + C_{mecha})$
- $\eta_2 \approx R_{slit}C_{mecha}C_{BV}(R_{BV} + R_{mecha}) + L_{mecha}C_{mecha}$
- $\eta_3 \approx R_{slit}L_{mecha}C_{mecha}C_{BV}$

The transfer function can thus be rewritten in the harmonic approximation:

$$H_{P \rightarrow \Delta Q} \approx \frac{C_{equ}C_{el}U_{pol}}{\gamma g_0 A_{pist}^*} \cdot \frac{1}{-j\frac{\omega_c}{\omega} + 1 + j\frac{\omega}{\omega_0} \frac{1}{Q_f} \frac{\omega^2}{\omega_0^2}}, \quad (2.56)$$

with:

- $C_{equ} = \frac{C_{BV}C_{mecha}}{C_{BV} + C_{mecha}}$
- $\omega_c = \frac{1}{R_{slit}(C_{BV} + C_{mecha})}$
- $Q_f = \left( \omega_0 C_{equ} (R_{mecha} + R_{BV}) + \frac{1}{\omega_0 R_{slit} C_{BV}} \right)^{-1}$
- $\omega_0 = \sqrt{\frac{1}{L_{mecha} C_{equ}}}$

From the expression of the transfer function, we find that the microphone exhibits two asymptotic regimes.

- For low frequencies, the transfer function is dominated by the  $j\omega/\omega_c$  factor. This means that the system acts as a high-pass filter with a cut-off frequency  $\omega_c$ .
- For high frequencies, the  $-j\omega_c/\omega$  factor becomes negligible, and the microphone acts as a second order damped resonant system.

## Resonance frequency

In the high frequencies regime, the microphone resonates at a frequency  $\omega_0$ :

$$\omega_0 = \sqrt{\frac{1}{L_{mecha}C_{mecha}} + \frac{1}{L_{mecha}C_{BV}}}. \quad (2.57)$$

When the different factors are expressed and factorized (**Table 2.3**), the expression becomes:

$$\omega_0 = \sqrt{\frac{\left( k_{sprg-p} + \frac{k_{rem}}{\gamma^2} + \frac{C_{avat}}{D_p^2} + k_{BV} \right) D_p^2}{I_{tot}}}, \quad (2.58)$$

with  $k_{BV} = A_{pist}^*{}^2 / C_{BV}$  the acoustic stiffness of the **BV**. The moment of inertia of the moving structure is the sum of the moments of inertia of all of its parts rotating around the fixed axis of the **AVATRAM**:

$$I_{tot} = m_p D_p^2 + m_{D_p} \frac{D_p^2}{3} + m_e D_e^2 + m_{D_e} \frac{D_e^2}{3}. \quad (2.59)$$

$$I_{tot} = D_e^2 \left( m_p \gamma^2 + \frac{m_{D_p}}{3} \gamma^2 + m_e + \frac{m_{D_e}}{3} \right), \quad (2.60)$$

where  $m_p$  and  $m_e$  are the masses of the piston and the electrode, which are assimilated to point masses given their out-of-plane translational movement.  $m_{D_p}$  and  $m_{D_e}$  are the masses of the rotating levers of constant section that connect the **AVATRAM** to the piston and the electrode respectively. Inserting this expression into equation (2.58):

$$\omega_0 = \sqrt{\frac{\gamma k_{tot}}{(m_p \gamma^2 + \frac{m_{D_p}}{3} \gamma^2 + m_e + \frac{m_{D_e}}{3})}}, \quad (2.61)$$

where:

$$k_{tot} = \gamma k_{sprg-p} + \gamma k_{BV} + \frac{k_{rem}}{\gamma} + \frac{C_{avat}}{D_p D_e}. \quad (2.62)$$

The resulting expression clearly shows that the resonance frequency will depend on the mechanical stiffness of the rotating structure as well as the stiffness of the **BV**. However, despite the small size of the **BV**, its acoustic stiffness will have little effect on the overall stiffness, because of the small size of the piston: since the piston is only used to harvest the acoustic signal, its size and therefore  $A_{pist}^*{}^2$  can be reduced. This will be further detailed in **Chapter 3**. Consequently, adding that  $C_{avat}$  and  $k_{rem}$  are decreased by design, the resonance frequency will mainly depend on the total moment of inertia of the moving structure, on the spring stiffness of the piston and on the geometric  $\gamma$  factor. Thus, in spite of the fact that  $k_{sprg-p}$  is determined by the required electrode displacement for a given variation of capacitance, the resonance frequency of the device can still be increased by decreasing the overall mass of the structure and designing a small  $\gamma$  factor. The resonance frequency should be increased beyond the operational frequency range of the device, with a value much higher than 20 kHz.

## Sensitivity

The sensitivity of the microphone in terms of generated charges is given by **equation (2.56)**, considered in the operation frequency band, away from its asymptotic regimes:

$$Sense_{\Delta Q} \approx \frac{C_{equ} C_{el} U_{pol}}{\gamma g_0 A_{pist}^*}. \quad (2.63)$$

By developing the expressions of  $C_{equ}$  and  $C_{el}$ , the sensitivity can be rewritten:

$$Sense_{\Delta Q} \approx \frac{\epsilon_0 A_{el} U_{pol}}{g_0^2} \cdot \frac{A_{pist}^*}{\gamma(k_{sprg-p} + \frac{k_{rem}}{\gamma^2} + \frac{C_{cavat}}{D_p^2} + k_{BV})} \cdot \quad (2.64)$$

The sensitivity of the device is therefore composed of two parts: an electrical part related to the capacitance of the device and a mechanical one related to the compliance of the mechanical structure. Increasing the surface of the electrode can clearly increase the sensitivity. However, this would have the undesirable effect of increasing the overall size of the device. Likewise, a higher sensitivity is also possible with a higher polarization voltage or a lower capacitance gap. This approach can be beneficial up until the capacitive nonlinearity becomes a limiting factor. Since the compliance of the structure is determined by the required electrode displacement, the sensitivity can only be further improved with a smaller  $\gamma$  factor. As we shall demonstrate in the following chapter, it is imperative to consider the benefits and drawbacks of each approach when optimizing the sensitivity of the device with respect to its size and performance limitations.

## Cut-off frequency

We have previously noted that, at low frequencies, the device acts as a high-pass filter with a cut-off frequency  $\omega_c$

$$\omega_c = \frac{1}{R_{slit}(C_{BV} + C_{mecha})} \cdot \quad (2.65)$$

This is due to the fact that, at low frequency, the pressure inside the **BV** has the time to equalize with the impinging pressure through the slits surrounding the piston. Since the acoustic stiffness of the **BV** has little effect due to the small size of the piston, we can safely assume that the compliance of the **BV**, despite the small size of the cavity, is larger than that of the mechanical structure. The cut-off frequency can then be rightly approximated by neglecting  $C_{mecha}$  and, developing the expressions of  $R_{slit}$  and  $C_{BV}$  we find:

$$\omega_c \approx \frac{1}{12\mu} W_{slit}^3 \frac{p_{pist}}{t_{slit}} \cdot \frac{1}{C_{BV}} \cdot \quad (2.66)$$

Decreasing the cut-off frequency to increase the operational **BW** of the device can thus be achieved by changes to either the **MEMS** sensor or its packaging. A larger back cavity will increase the compliance of the **BV**, thereby decreasing the cut-off frequency. This comes of course at the cost of a bulkier device. Alternatively,  $\omega_c$  is decreased by using shorter, thicker and narrower slits to increase the slit resistance. No matter the approach,  $\omega_c$  should be lower than the operational **BW** of the device.

## Quality factor

The quality factor determines the gain at resonance of the device in its high frequencies regime. From **equation (2.56)** we find:

$$Q_f = \left( \omega_0 C_{equ} (R_{mecha} + R_{BV}) + \frac{1}{\omega_0 R_{slit} C_{BV}} \right)^{-1} \cdot \quad (2.67)$$

As expected, the quality factor will be determined by the dissipation mechanisms in the device: mechanical dissipations  $R_{mecha}$  and  $R_{slit}$ , and thermal dissipations in the **BV**  $R_{BV}$ . These dissipations will also determine the noise of the **MEMS** sensor.

#### MICROPHONE MODEL VARIABLES

$g_0$	Capacitance gap
$A_{el}$	Electrode surface
$U_{pol}$	Polarization voltage
$k_{neg}$	Spring softening
$k_{sprg-e}$	Stiffness of electrode mechanical springs
$k_{rem}$	$-(2k_{neg} - k_{sprg-e})$
$t_{slit}$	Slit thickness
$w_{slit}$	Slit width
$p_{pist}$	Piston perimeter
$A_{pist}$	Piston surface
$A_{pist}^*$	$A_{pist} + \frac{w_{slit}p_{pist}}{2}$
$C_{avat}$	AVATRAM total rotational stiffness
$k_{sprg-p}$	Stiffness of piston mechanical springs
$D_e$	Distance from AVATRAM axis of rotation to electrode center
$D_p$	Distance from AVATRAM axis of rotation to piston center
$\gamma$	$D_p/D_e$
$z_e$	Electrode out-of-plane displacement
$z_p$	Piston out-of-plane displacement
$I_{tot}$	Total moment of inertia
$R_{slit}$	Slit viscous resistance
$R_{mecha}$	Mechanical drag resistance
$C_{mecha}$	Mechanical compliance
$L_{mecha}$	Structure inertia
$R_{BV}$	BV resistance
$C_{BV}$	BV compliance

Table 2.4: Microphone model main variables.



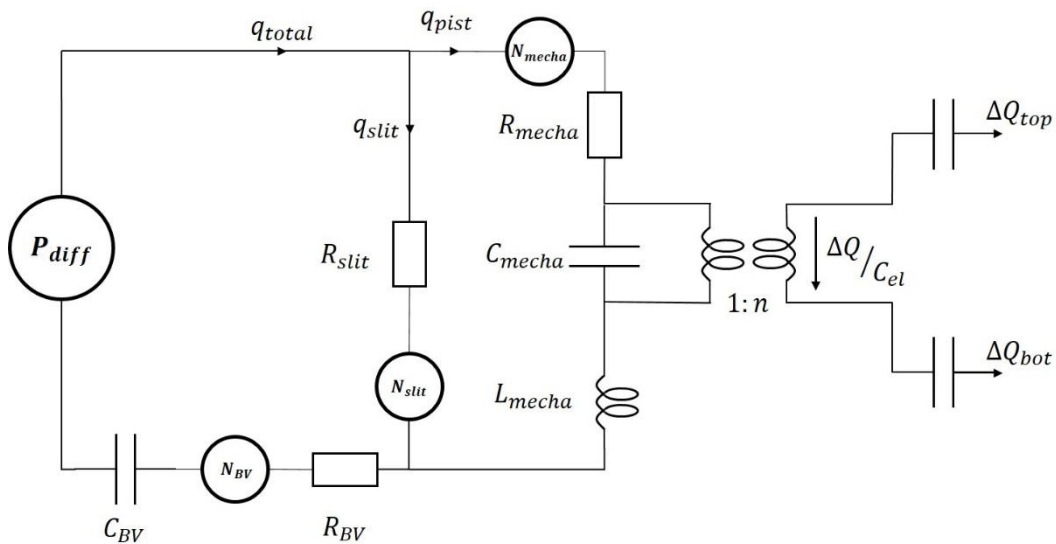
## 2.3. Microphone Noise

### 2.3.1. Noise sources

The noise of the **MEMS** sensor stems from all dissipative processes within the system. With the previously developed lumped model, these processes can be easily identified by the presence of dissipative circuit elements, i.e. the electrical resistors. Each resistance will therefore lead to a fluctuating pressure, translated as noise added to the output of the system. We recall from **Chapter 1** the expression of the spectral density of the resulting pressure fluctuations, derived from Nyquist's relation:

$$P_{noise} = \sqrt{4k_B T R_{ac}} [Pa/\sqrt{Hz}] . \quad (2.68)$$

The pressure fluctuations relative to each resistor can then be represented as added *effort* sources in the lumped elements model's equivalent circuit (**Figure 2.12**). Thus, by finding the transfer function between each noise source and the output, it is possible to quantify the effects on the microphone's signal. Moreover, in order to reference these effects to the input of the device and describe them in terms of Equivalent Input Noise (**EIN**), this transfer function should be divided by the transfer function between the input and the output of the device. This is done in a similar fashion to the steps taken previously to find the device transfer function. However, these steps are too numerous to list here.



**Figure 2.12:** Equivalent circuit of the lumped elements model with the noise sources represented as generators

#### Slit Resistance Noise

Written in terms of **EIN**, the fluctuations due to the acoustic resistance of the slits are:

$$EIN_{slit} = \frac{1+j\omega R_{BV}C_{BV}}{j\omega R_{slit}C_{BV}} \sqrt{4k_B T R_{slit}} . \quad (2.69)$$

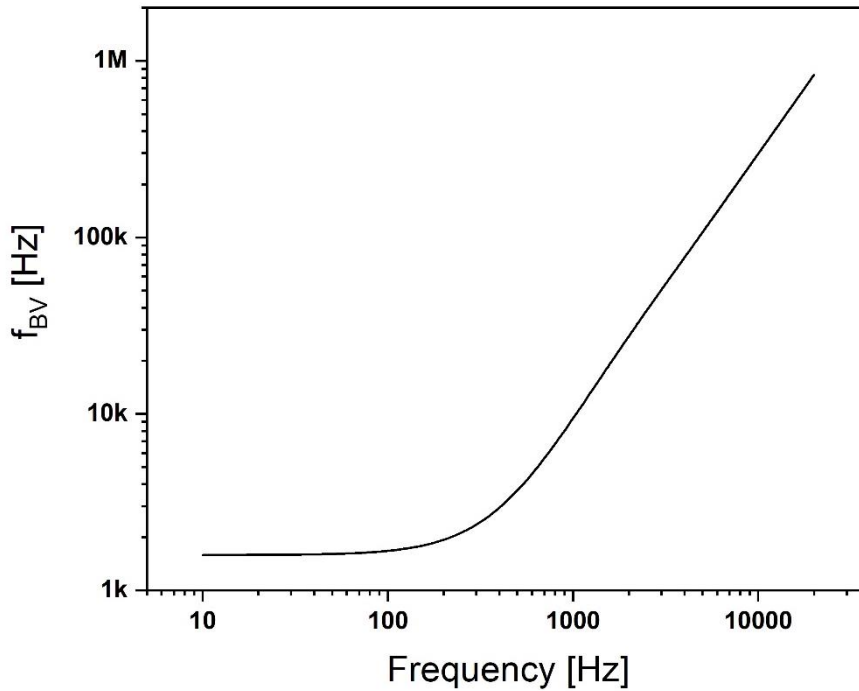
Defining the cut-off frequency of the **BV** as  $f_{BV} = (2\pi R_{BV}C_{BV})^{-1}$ , we find that it varies as a function of the signal frequency, similarly to  $R_{BV}$  and  $C_{BV}$ . The effect of the **BV** in this respect is therefore better visualized by tracing the variations of  $f_{BV}$ . From **Figure 2.13**, we can deduce that the cut-off frequency of the **BV** is always much higher than the signal frequency, and its effect is therefore negligible.

**Equation (2.69)** simplifies to:

$$EIN_{slit} \approx \frac{1}{j\omega C_{BV}} \sqrt{\frac{4k_B T}{R_{slit}}} . \quad (2.70)$$

Thus, by replacing  $R_{slit}$  by its expression, we find that the input referred slit resistance noise is:

$$EIN_{slit} \approx \frac{1}{j\omega C_{BV}} \sqrt{\frac{4k_B T w_{slit}^3 \rho_{pist}}{12\mu t_{slit}}} . \quad (2.71)$$



**Figure 2.13: Variations of the BV cut-off frequency as a function of the signal frequency**

## Mechanical Resistance Noise

Written in terms of **EIN**, the fluctuations due to the mechanical resistance of the drag force acting on the piston are:

$$EIN_{mecha} = \frac{1+j\omega(R_{BV}+R_{slit})C_{BV}}{j\omega R_{slit}C_{BV}} \sqrt{4k_B T R_{mecha}} . \quad (2.72)$$

As we have previously noted, the resistance of the slits and the compliance of the **BV** are designed in such a way that the cut-off frequency of the device  $\omega_c$  takes values in the order of tens of *Hz* or lower. This means that the product  $j\omega R_{slit} C_{BV}$  dominates the numerator of equation (2.72), which therefore simplifies to:

$$EIN_{mecha} = \sqrt{4k_B T R_{mecha}} . \quad (2.73)$$

When  $R_{mecha}$  is expressed, we find the input referred mechanical resistance noise:

$$EIN_{mecha} = \sqrt{4k_B T \mu t_{slit} \frac{p_{pist}}{w_{slit} A_{pist}^*} \frac{1}{2}} . \quad (2.74)$$

This noise is commonly referred to as slide-film damping noise.

### Back Volume resistance noise

The back cavity is the last element of the acoustic path. The fluctuations due to the thermal dissipation along the cavity walls affect the entire device, which means they have the same transfer function as the one placed at the microphone's input. The input referred noise of the **BV** resistance is therefore:

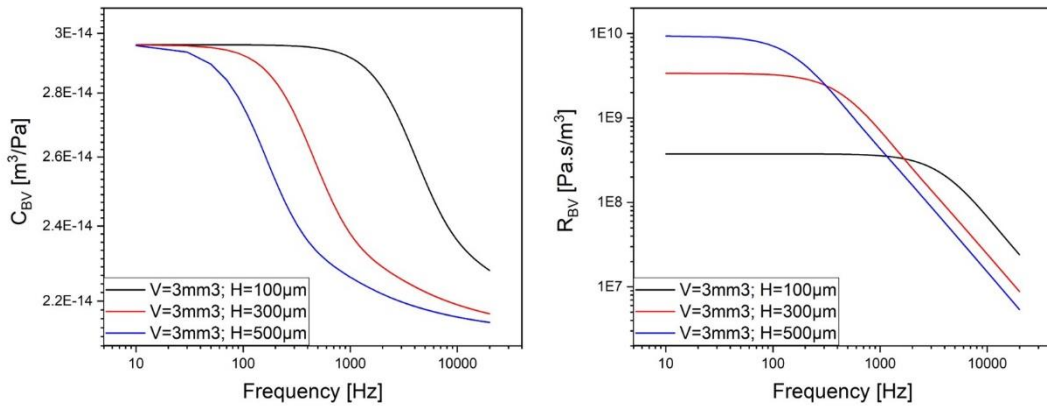
$$EIN_{BV} = \sqrt{4k_B T R_{BV}} . \quad (2.75)$$

## 2.3.2. Noise analysis

Reducing the total noise of the **MEMS** sensor requires reducing the contribution of each noise source. Considering the mechanical and slit resistances' noises, we find that they have a contrary yet not entirely opposite dependence on the same geometric parameters. Bearing in mind that the piston perimeter is proportional to the square root of the piston surface, we can list the dependencies of both noise sources thusly

$\sqrt{\int_{f_{min}}^{f_{max}} EIN_{slit}^2}$	$\sqrt{\int_{f_{min}}^{f_{max}} EIN_{mecha}^2}$
$\propto A_{pist}^{1/4}$	$\propto A_{pist}^{-3/2}$
$\propto w_{slit}^{3/2}$	$\propto w_{slit}^{-1/2}$
$\propto t_{slit}^{-1/2}$	$\propto t_{slit}^{1/2}$
$\propto C_{BV}^{-1}$	—

Although it would increase  $EIN_{slit}$ , increasing the area of the piston would lead to a three-fold decrease in the mechanical resistance noise. Conversely, decreasing the slit width would increase  $EIN_{mecha}$  yet decrease the slit resistance noise three-fold. A high piston area to slit width ratio would therefore serve to decrease both noise sources equally. Furthermore, there is nothing to gain from varying the thickness of the slits as the two noise sources have an equal but opposite dependence on this parameter. We also note that the noise due to the slit resistance is a pink noise with a power density that is inversely proportional to the frequency. This noise will therefore be more strongly present at lower frequencies in the **BW** compared to the white mechanical resistance noise. Finally, increasing the size of the **BV** and the depth of the cavity can also be used as a way to decrease both the slit resistance noise and the **BV** noise (**Figure 2.14**).



**Figure 2.14: Variations of  $C_{BV}$  and  $R_{BV}$  for different cavity volumes and depths, calculated in the 1D-model approximation (Appendix B).**

The noise reduction methods thus described can lead to a stringent tradeoff between a low noise level and large device footprint and packaging. Besides, the geometric parameters should also be considered from a technological and mechanical design point of view, taking into account what is achievable through the fabrication process and its effect on the mechanical structure. However, as we shall detail in the next chapter, even by considering all of these limitations, the noise of the **MEMS** sensor can still be drastically reduced, making the **ROEC** the main contributor to the noise of the microphone.

# Chapter 3 Microphone design and fabrication

The performance parameters generated from the microphone's model largely depend on geometrical elements. From the **BW** to the noise sources, the microphone's geometry has a preponderant influence on its final performance. Since the fabrication process is the determining factor with respect to what is achievable regarding the device's geometry, it should be adequately chosen keeping in mind its feasibility, risks, cost and scalability. The present chapter illustrates the selected process flow and the role of each step in the making of the final device. Then, after discussing the resulting effects on device performance, the design process and the final microphone designs are presented.

## 3.1. Device Fabrication

The M&NEMS fabrication process, developed to maturity and implemented by CEA-Leti, was chosen for this microphone design. This two-wafer process allows the presence of relatively thick and thin layers within the **MEMS** device, which gives great flexibility in terms of design possibilities. Furthermore, it enables the juxtaposition of encapsulated and exposed parts, crucial for this new microphone concept. Adding that it shares core similarities with well-known industrial processes, this fabrication method exhibits all the required elements to reach the set objectives in terms of feasibility and scalability. Even though the process does present drawbacks concerning its risks and cost, they can be mitigated by changing and adapting the process flow.

### 3.1.1. Process flow

#### **Device wafer**

- a) The fabrication process starts with a heavily p-doped 550  $\mu\text{m}$  thick Silicon On Insulator (**SOI**) wafer, with a 1  $\mu\text{m}$  thick top monocrystalline silicon (Top-Si) and a 1  $\mu\text{m}$  buried silicon oxide (**BOX**). The bulk silicon of the wafer (Bulk-Si) is also doped, as it will later serve as a counter electrode. The Top-Si is first patterned and covered with a 1  $\mu\text{m}$  thick sacrificial silicon oxide ( $\text{SiO}_2$ ) layer, which is then etched. On one hand, in the places where the Top-Si had previously been removed, the etching of the  $\text{SiO}_2$  reveals the bulk, allowing a subsequent epitaxial growth to create a link

between the bulk silicon and the top epitaxy. The pillar of the **AVATRAM** as well as the connection points between the lever arms and the piston in air are created during this important step. On the other hand, the sacrificial layer can be maintained to protect the Top-Si in the places where a thin silicon part is required. It can also be used to make space for the capacitance gap between the moving electrode and the top electrode. Therefore, the deposited thickness of sacrificial SiO<sub>2</sub> should be equal to the **BOX** thickness, so that both capacitance gaps are equal.

- b) After a p-doped epitaxial silicon growth step, the epitaxial layer is dry polished then planarized by Chemical Mechanical Planarization (**CMP**) in order to reduce it to the desired thickness of 20  $\mu\text{m}$  and to obtain a flat wafer surface. A thickness of 300  $\text{nm}$  of Germanium (Ge) is then deposited and patterned in preparation of a future Aluminum-Germanium (AlGe) eutectic bonding. This step serves two purposes: it ensures the electrical connection with the different parts of the device, and, around what will be the vacuum cavity and the **BV**, it forms the bonding seal with the cap wafer. A thin SiO<sub>2</sub> layer is then deposited and patterned to serve as a hard mask for the upcoming Deep Reactive Ion Etching (**DRIE**) of the epitaxial growth. In addition, a photoresist is deposited around the Germanium to safeguard the Si next to it for a subsequent etching step.
- c) The **DRIE** step patterns the top 20  $\mu\text{m}$  Si layer. Afterwards, the photoresist is stripped followed by the partial etching of the Si around the previously deposited Germanium. This creates trenches around the contact points of the two wafers to confine any overflow during the eutectic bonding process.
- d) Finally, a controlled isotropic etching of the SiO<sub>2</sub> by Hydrogen Fluoride (HF) vapor releases the structures. As we shall later explain, the precise control of the HF release step is critical, since the **BOX** is used as an anchor point for the top counter-electrode, and as a stopping layer during the **DRIE** of the Bulk-Si.

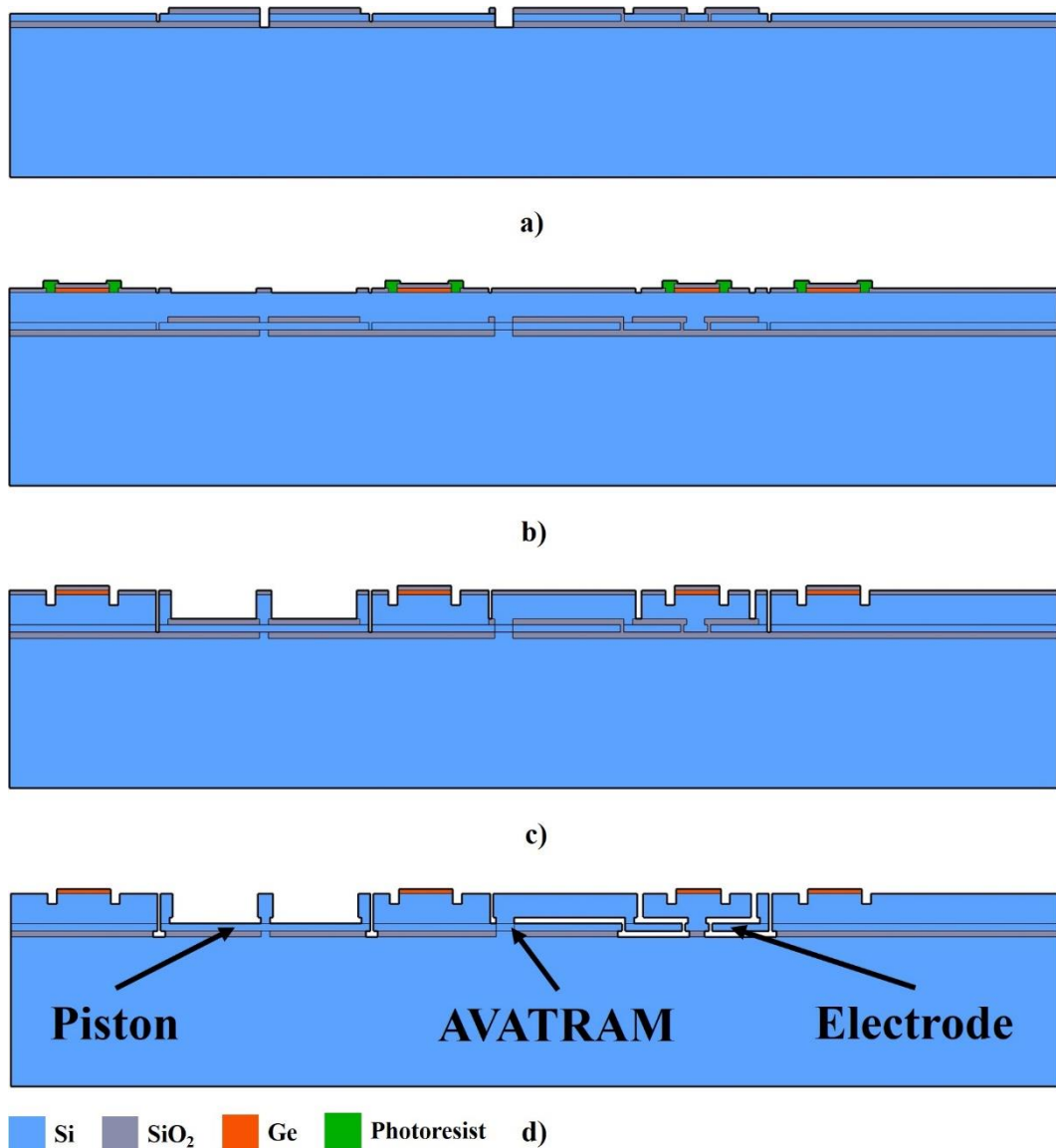


Figure 3.1: Device wafer process flow.

## Cap wafer

- e) Parallel to the device wafer, the cap wafer is processed starting with a  $550\ \mu\text{m}$  thick crystalline Si wafer. A  $1\ \mu\text{m}$  thick  $\text{SiO}_2$  layer is created via thermal oxidation and patterned by a lithography step revealing an access to the Si bulk. A combination of Aluminum-Copper alloy (AlCu), Titanium (Ti), and Titanium Nitride (TiN) is then deposited and patterned forming a first conductive layer to route the electrical signal. At this point, another oxide layer is deposited by chemical vapor deposition using tetra-ethyl orthosilicate (TEOS), and its density is increased by thermal annealing.

- f) After a **CMP** step, a 200 nm thin Silicon Nitride (SiN) layer is deposited followed by another TEOS deposition of a 3 μm thick oxide layer. The SiN acts as a stopping layer for the subsequent etching of the oxide layer before it is itself etched and stripped. This effectively creates protruding elements on the cap wafer which will be the contact points with the device wafer during the bonding step. However, before depositing the Aluminum necessary for the eutectic bonding, the first TEOS oxide layer is patterned to create vias leading to the first conductive layer, enabling the routing of the electrical signal from one conductive layer to the other.
- g) Once the Aluminum-Silicon (AlSi) forming the second conductive layer is deposited and patterned, the wafer undergoes two consecutive etching steps. The first patterns the total oxide thickness, and the second etches the bulk silicon to create what will become the vacuum cavity and the **BV**. The Si etching depth can vary between 100 μm and 300 μm depending on the required cavity size, as it will later be discussed. Finally, a getter layer is deposited at the bottom of the future vacuum cavity through a stencil.

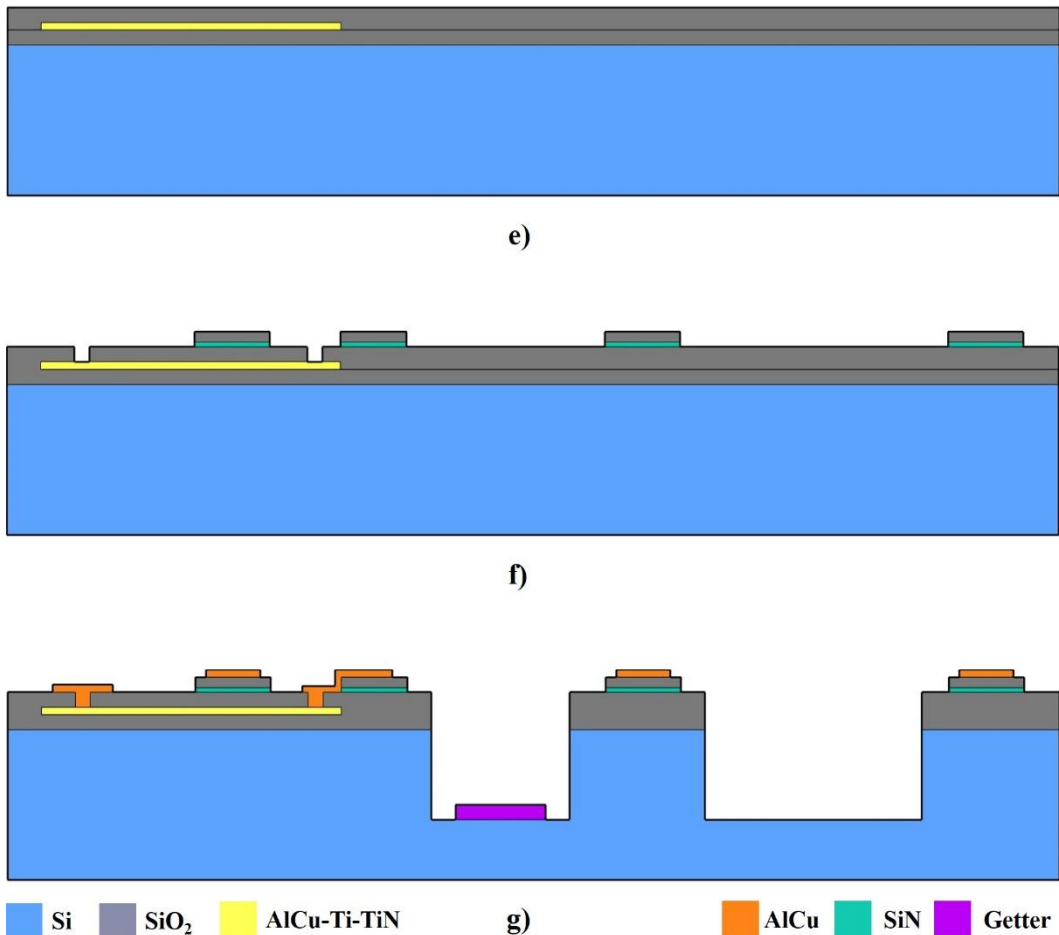


Figure 3.2: Cap wafer process flow.



## Wafer stack

- h) When the two wafers are ready, the device wafer is flipped and bonded to the cap wafer through AlGe eutectic bonding at 450 °C. The Bulk-Si of the device wafer is then thinned down to a thickness of 100  $\mu\text{m}$  by successive coarse and fine mechanical grinding steps. As we will later explain, the final microphone design incorporates two **AVATRAMs**, and, consequently, two levers connecting the piston to the hinges. The thinning of the Bulk-Si is therefore important, not only for reducing the total thickness of the wafers, but also for reducing the mass of the piston levers.
- i) The **DRIE** of the Bulk-Si defines the pillars of the hinges and their connections to the piston, and separates the bulk counter-electrodes from the rest of the bulk. The Bulk-Si remaining on top of the piston is also removed during this step, which uses the **BOX** as an etch-stopping layer. A second controlled HF vapor release of the **BOX** entirely exposes the piston to the surrounding atmosphere. Finally, parts of the device wafer are mechanically sawed off to expose the electrical bonding pads of the final device.

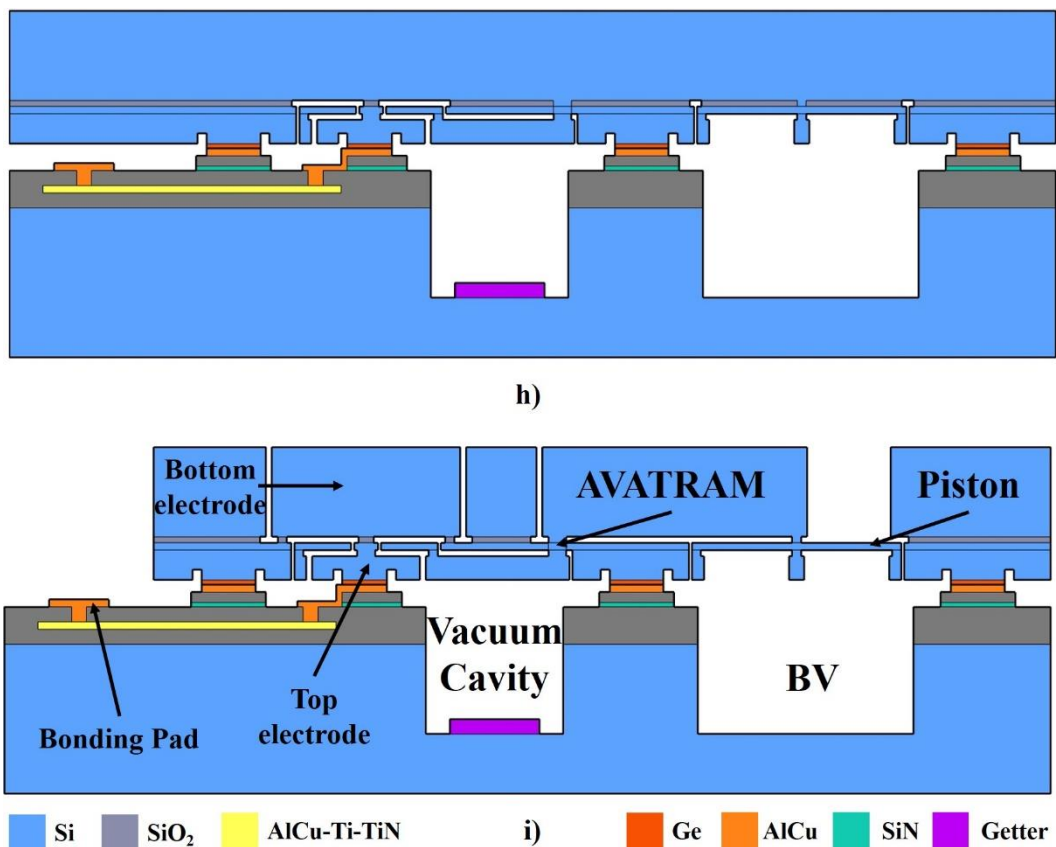
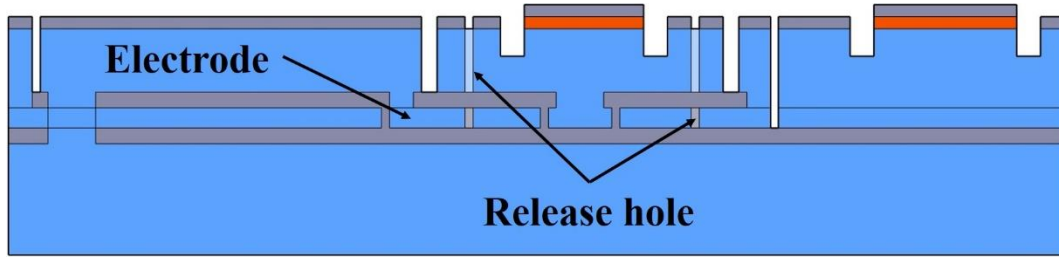


Figure 3.3: Wafer stack process flow.

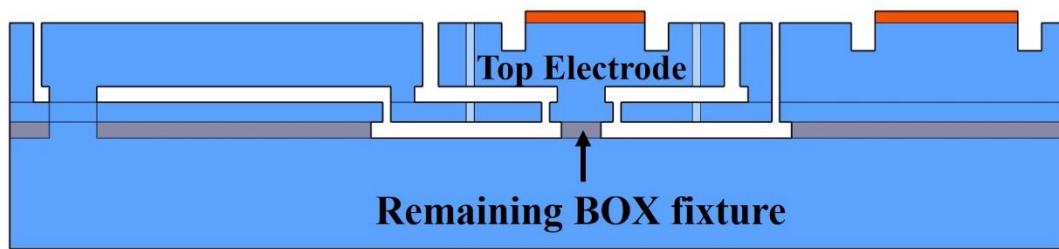
### 3.1.2. Critical dimensions and risks

All the different steps that make up the fabrication process flow present critical aspects that should be taken into account during the design process. However, the limitations and risks of some specific steps can have a more profound impact on device performance.

- Although the **DRIE** process can have a maximum achievable aspect ratio of 30:1, a ratio of 20:1 is preferred for fabrication on an industrial scale. Consequently, for the etching of the epitaxial growth of  $20\ \mu\text{m}$ , the smallest achievable trench width is considered to be limited to  $1\ \mu\text{m}$ . This is an important parameter since it is during this step that the slits around the piston are created. The slit width  $w_{slit}$  is a parameter that eventually affects the microphone's cut-off frequency, as well as its mechanical and slit noise sources. Furthermore, the same aspect ratio is considered for the **DRIE** of the  $100\ \mu\text{m}$  thick Bulk-Si, meaning that the trenches used to define the **AVATRAM** pillar and the piston levers can have a minimum width of  $5\ \mu\text{m}$ . Although the size of these trenches is not critical, a secondary effect can take place during this step, since the surface to etch on top of the piston is very large compared to the trenches. This can lead to etch notching at the edges of the piston, which can have detrimental effects if it takes place near the edges of the **BOX** stopping layer.
- The first HF vapor release step etches the exposed SiO<sub>2</sub> on the device wafer. Aside from the sacrificial SiO<sub>2</sub> used to protect the thin parts of Si during the first **DRIE**, the HF vapor also etches the **BOX** exposed under the piston slits and under the movable electrode. Concerning the latter, the etch distance should be set so that the movable electrode is completely released from the **BOX** and the sacrificial layer, while making sure there remains a sufficient part of the **BOX** to which the top electrode remains fixed. This can be done by creating small release holes in the top and moving electrodes during the first **DRIE** and the Top-Si patterning steps (**Figure 3.4**).



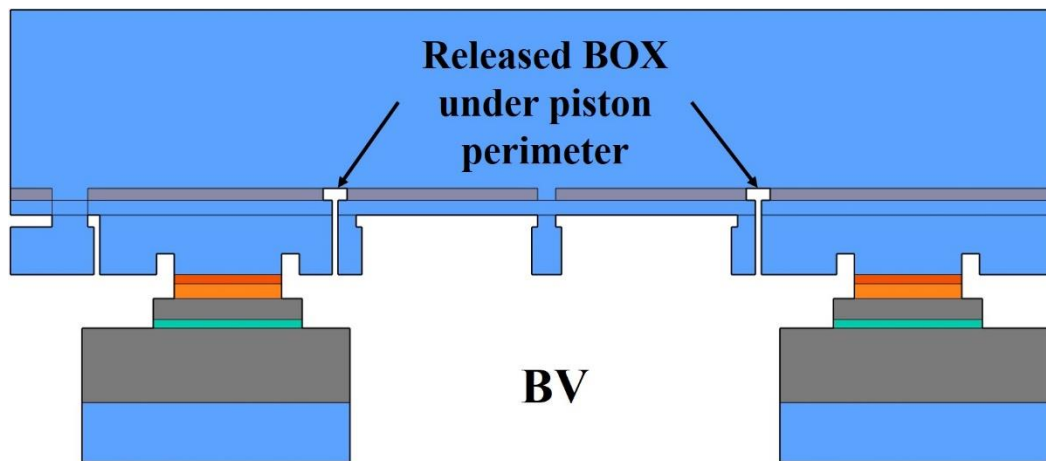
Zoom Electrode - Step c)



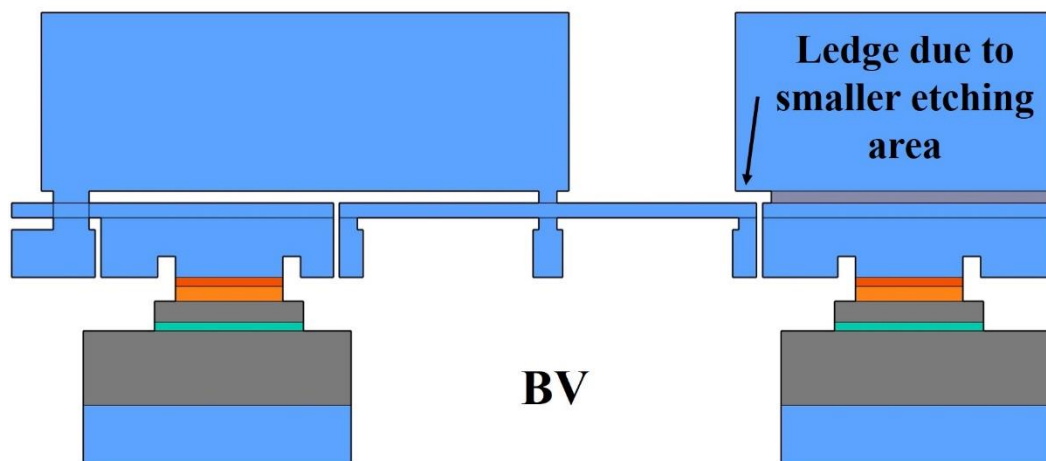
Zoom Electrode - Step d)

**Figure 3.4: Steps c) and d) of the device wafer showing how release holes are used to ensure the full release of the movable electrode while maintaining a BOX fixture to hold the top counter-electrode in place.**

A multitude of these holes can effectively reduce the etch distance required to completely release the movable electrode from the oxide. Moreover, a small etch distance proves also necessary on the piston side, since, in this part, the **BOX** is used as a stopping layer for the second **DRIE**. Ideally, the **BOX** should be present all over the piston area, so that all of the Bulk-Si covering the piston can be removed. However, as parts of the **BOX** are etched all around the piston, the missing etch-stopping layer could lead to the etching of the Si piston perimeter, increasing the width of the slits. To avoid this, the margin of error concerning the maximum release distance of the **BOX**, as well as the notching effects during the **DRIE** are taken into account when defining the area to etch. The smaller etching area results in ledges all around the piston, which lead to squeeze-film damping and added noise to the microphone. However, well controlled HF vapor release and **DRIE** steps can alleviate these effects.



Zoom Piston - Step h)

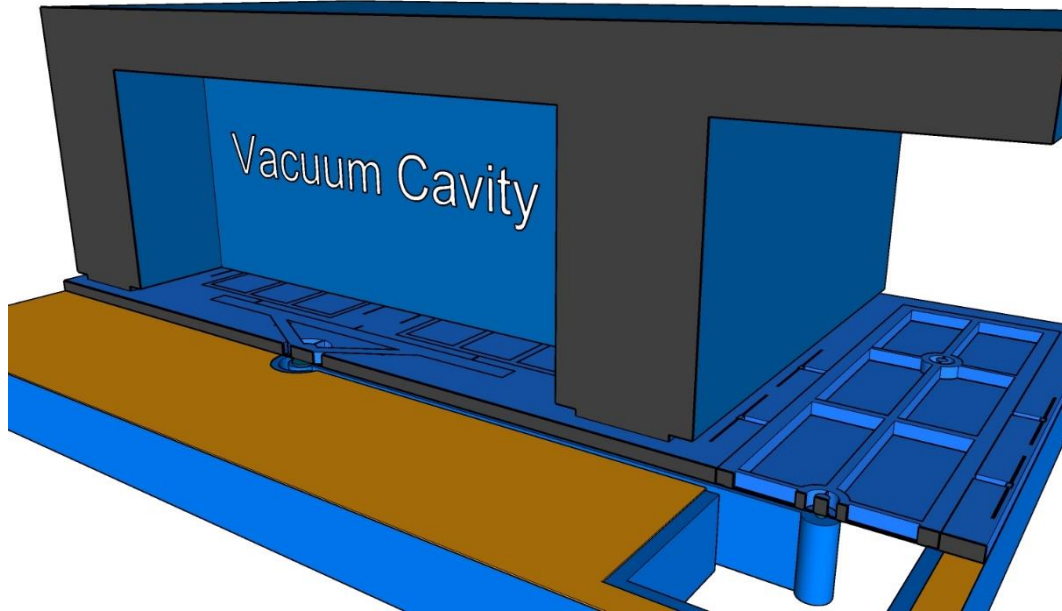


Zoom Piston - Step i)

Figure 3.5: Steps h) and i) of the wafer stack showing the results of the first HF release and its consequences. The reduced etching area creates a ledge around the piston perimeter, leading to squeeze film damping.

- The Si etching of the cap wafer to create the space for the vacuum cavity and the **BV** is an important step that directly affects the performance of the final device. As we have previously explained, the noise due to thermal dissipation along the **BV** walls is proportional to the **BV**'s resistance, which itself is a function of the size and the depth of the cavity. More specifically, a deeper cavity at the same volume leads to a lower resistance and therefore a lower noise. What is more, a deeper vacuum cavity for the same surface has a larger volume, which can improve the quality of the vacuum. However, multiple side by side deep cavities can weaken the wafer, giving it the shape of a thin waffle. A compromise should therefore be found between the depth of the cavities and the structural integrity of the wafer.
- The second HF vapor release is also a critical step and should be well controlled due to the fact that the vacuum cavity is partly sealed by the

remaining **BOX** on the device wafer. However, given its high electrical permittivity, the remaining oxide also adds to the stray capacitance at the output of the bottom electrode. Thus, the second HF release should be set by considering the margin of error of its maximum and minimum etch distance, as well as the margin of error of the first HF release. By doing so, the stray capacitance can be minimized while still ensuring the airtightness of the cavity.



**Figure 3.6:** 3D schematic of a final microphone design showing the juxtaposed cavities and the different parts of the device. Parts of the cap wafer and the MEMS have been sectioned off to reveal otherwise hidden details of the structure.

### 3.1.3. Process adaptation

The M&NEMS process was developed for the fabrication of a multitude of devices, mostly based on piezoresistive nanogauge transduction. It is therefore not optimized for this new microphone design. Still, several of the listed undesirable effects due to process risks can be alleviated by adapting the fabrication process with minor changes to the process flow. Even though these changes were not implemented for the fabrication of the devices discussed in this document, it is important to consider any possible optimization of the process flow. In fact, the most critical risk for device performance is the squeeze-film damping around the piston, which can be drastically reduced by increasing the gap between the piston and the bulk. However, on an SOI wafer, this gap is determined by the thickness of the **BOX**, which is also used to create the capacitance gap between the movable electrode and the bottom electrode. Thus, the goal is to increase the gap in certain critical areas while maintaining the small gap for higher capacitive density.

This objective can be accomplished by opting for a crystalline silicon wafer instead of an **SOI** wafer at the start of the process. By doing so, the limitation of a previously set **BOX** thickness is removed, and different SiO<sub>2</sub> thicknesses can be etched into and deposited onto the crystalline silicon bulk. The following steps can then be performed onto the silicon wafer before the previously described process steps, which remain unchanged.

- i. The wafer is first patterned and etched to create trenches in the places where a larger gap is required. The trenches are then filled with the deposition of a thick SiO<sub>2</sub> layer, which is then planarized.
- ii. Another SiO<sub>2</sub> layer is deposited, the thickness of which is equal to the required capacitance gap thickness. Finally, a thin polycrystalline Si layer is grown on top of the SiO<sub>2</sub> layer, giving a layer stack similar to the starting **SOI** in the original M&NEMS process.
- iii. Steps a) to d) can then be performed without any changes.

The initial patterning of the bulk-Si with deep trenches can also be used to counter another effect, which is the imbalance of the capacitances between the movable electrode and its counter electrodes. More precisely, as it will be explained further along this chapter, the movable electrode is reinforced by a skeleton etched from the epitaxial silicon growth. These reinforcements takes space from the top counter-electrode, as it is also etched from the same layer. However, the bottom side of the movable electrode remains uniform, with a larger overlap surface with the bottom electrode. The resulting difference in capacitance leads to unbalanced electrostatic forces, pulling the electrode towards the bottom counter-electrode, thereby changing the original capacitance gaps. Thus, deeper trenches can be used to increase the capacitance gap with the bottom counter-electrode in the places where the overlap surface is not matched by the top counter-electrode. Finally, we do note that, aside from the added fabrication steps, this adapted process has the undesirable effect of changing the Top-Si layer, and the subsequent epitaxial growth, from monocrystalline to polycrystalline. The poorer mechanical properties of the material should therefore be kept in mind during the design process.



i.



ii.

■ Si   ■ SiO<sub>2</sub>

**Figure 3.7: Adapted device wafer process flow.**

## 3.2. Achievable performance

The fabrication process not only defines the design possibilities for the different elements of the device, but also directly affects several microphone performance parameters by setting geometrical fabrication limits. With these limitations, some minor degrees of freedom are removed, and the chain linking all the performance parameters of the device can be untangled.

### 3.2.1. Cut-off frequency

Recalling its expression from **Chapter 2**, the cut-off frequency is a function of the piston perimeter  $p_{pist}$ , the width and thickness of the slits  $w_{slit}$  and  $t_{slit}$ , and the compliance of the **BV**  $C_{BV}$ :

$$\omega_c \approx \frac{1}{12\mu} w_{slit}^3 \frac{p_{pist}}{t_{slit}} \cdot \frac{1}{C_{BV}}. \quad (3.1)$$

In order to increase the microphone's **BW** and decrease  $\omega_c$ , thick, short and narrow slits should be privileged. The thickness of the slits is determined by the thickness of the epitaxial growth. Given that many structural elements are formed by this layer, its thickness was set at  $20 \mu m$  to ensure the structural rigidity of the device. Concerning the width of the slits, it has a lower bound of  $1 \mu m$ , determined by the aspect ratio (20:1) considered for the **DRIE** of the epitaxial growth. Accordingly, the only remaining variables in the expression of  $\omega_c$  are the piston perimeter and the compliance of the **BV**. **Figure 3.8** displays how these two parameters affect the cut-off frequency  $f_c = \omega_c/2\pi$  of the device. For the sake of simplicity, a square piston is considered with  $p_{pist} = 4\sqrt{A_{pist}}$ . The cut-off frequency increases therefore linearly with the piston side length, yet remains very low, below  $20 \text{ Hz}$  regardless of the size of the **BV**. What is more, for such low frequencies, the depth of the cavity has no effects on  $C_{BV}$ , leading to no visible effects on the cut-off frequency from this parameter (**Figure 2.10**). Thus, considering the limitations imposed by the fabrication process, the cut-off frequency can be reduced below the targeted operational **BW** of the microphone. It should be specified that if a higher cut-off frequency is required, it could easily be achieved by either increasing the width of the slits or adding a dedicated hole towards the **BV**. The latter is more preferable as it has the benefit of not increasing the mechanical and slit noise sources, both of which are functions of  $w_{slit}$ .



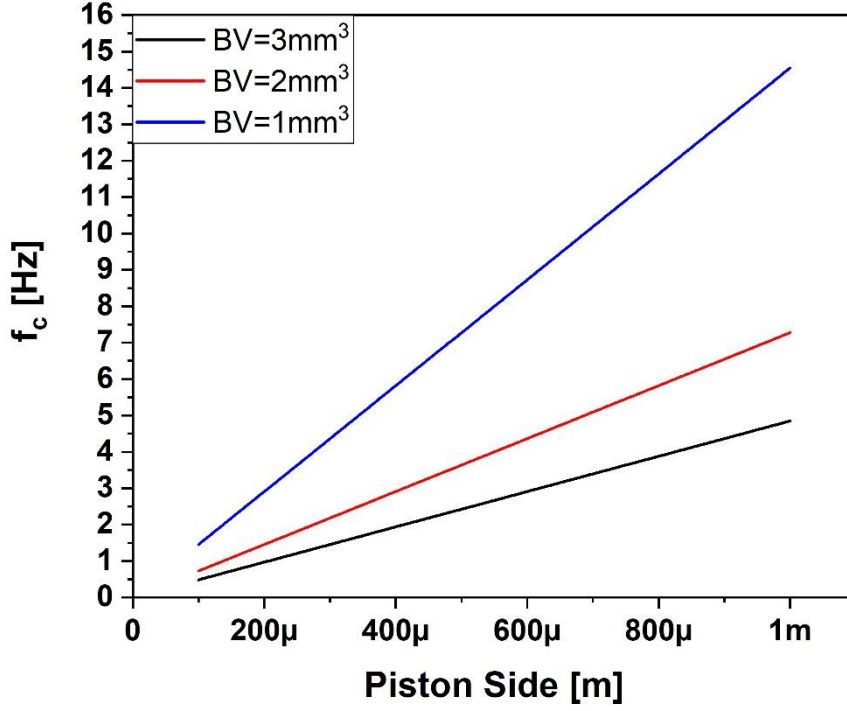


Figure 3.8: Variation of the theoretical cut-off frequency as a function of the side length of a square piston at different BV sizes.

### 3.2.2. Noise Level

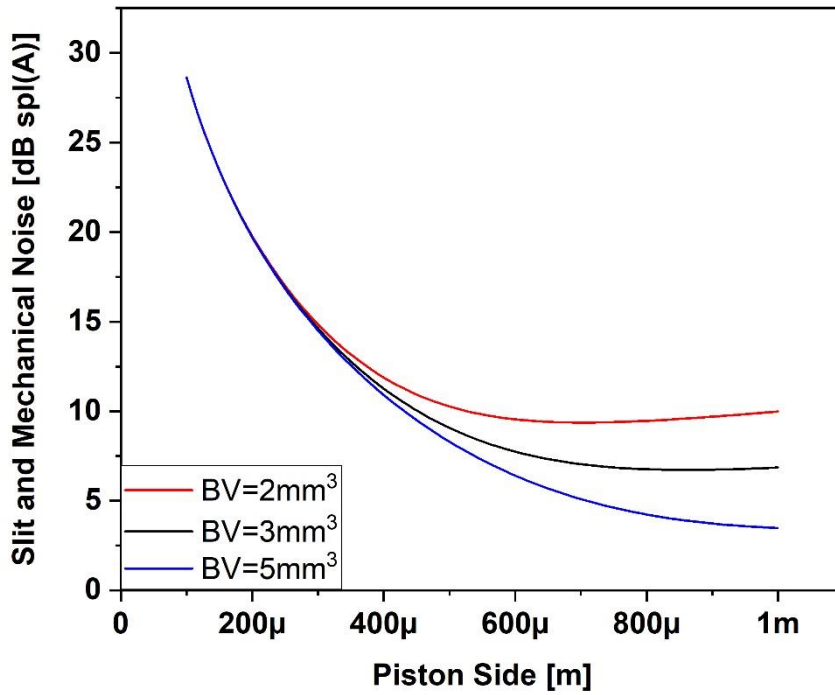
The mechanical resistance and slit resistance noises both depend on the piston and slit geometry. As we have previously noted in **Chapter 2**, a high piston area to slit width ratio would serve the objective of reducing both noise sources. With  $w_{slit}$  and  $t_{slit}$  set at  $1 \mu m$  and  $20 \mu m$  respectively, the two noises are found to remain only dependent on the piston geometry:

$$EIN_{slit} = \frac{1}{j\omega C_{BV}} \sqrt{\frac{4k_B T w_{slit}^3 p_{pist}}{12\mu t_{slit}}} \quad (3.2)$$

$$EIN_{mecha} = \sqrt{4k_B T \mu t_{slit} \frac{p_{pist}}{w_{slit}} \frac{1}{A_{pist}^*}} \quad (3.3)$$

Thus, analogous to the cut-off frequency, the noises can be quantified as functions of the side length of a square piston and of the size of the **BV**, the latter only affecting the slit resistance noise. To do so, the noises are integrated and A-weighted over the expected working **BW** of the device between  $20 Hz$  and  $20 kHz$ . The total noise due to both sources can then be graphed as a function of the piston side length as shown in **Figure 3.9**. For small piston surfaces, the mechanical resistance noise is dominant, leading to the same total noise regardless of **BV** size.

However, as the piston size is increased, the effects of the mechanical resistance diminish in favor of the slit resistance. The latter increases with the size of the piston, but decreases as the **BV** size and compliance increase. We add that the depth of the cavity does not have any consequential effect on the slit resistance noise, due to the relatively small variation of  $C_{BV}$  as a function of cavity depth (**Figure 2.14**). It can therefore be concluded that the noise due to the mechanical and slit resistances can be reduced to below  $15 \text{ dBspl}(A)$  by considering square pistons with a side length larger than  $300 \mu\text{m}$ , or their equivalent in terms of surface.



**Figure 3.9:** Variations of the total slit and mechanical noise as a function of the side length of a square piston, for different **BV** sizes.

Concerning the **BV** noise, it varies with the **BV** resistance, which strongly depends on the size and on the depth of the cavity:

$$EIN_{BV} = \sqrt{4k_B TR_{BV}} \quad (3.4)$$

**Figure 3.10** displays the variations of the **BV** noise as a function of the **BV** size at different cavity depths. At each point, the **BV** resistance is quantified by numerical simulations, as detailed in **Appendix B**. It can clearly be observed that the noise decreases when both the volume and the depth of the cavity are increased. However, the noise level remains quite significant, even more so when considering the limitation in cavity depth, which is set so as not to weaken the cap wafer. Accordingly, for a maximum cavity depth of  $300 \mu\text{m}$ , a noise lower than  $15 \text{ dBspl}(A)$  is only possible with a cavity volume larger than  $7 \text{ mm}^3$ . In this case,

an integrated **BV** fabricated from the cap wafer, as considered for this new microphone design, is no longer conceivable as it would take too much space and unnecessarily increase the cost. Therefore, in keeping an integrated **BV**, it becomes the dominant noise source when compared to slit and mechanical resistance noises. Consequently, for a **BV** of  $3 \text{ mm}^3$  and a cavity depth of  $300 \mu\text{m}$ , the noise limit of the device is set by the **BV** noise at around  $19 \text{ dBspl}(A)$ . On a final note, this graph further underlines the importance of taking into consideration the effects of thermal dissipation along the back cavity walls. The fact that a larger **BV** is necessary to improve the performance in terms of noise goes against the current trend of decreasing the overall size of the microphone. If such a size constriction is imposed, it is essential to consider the limitation of the resulting noise.

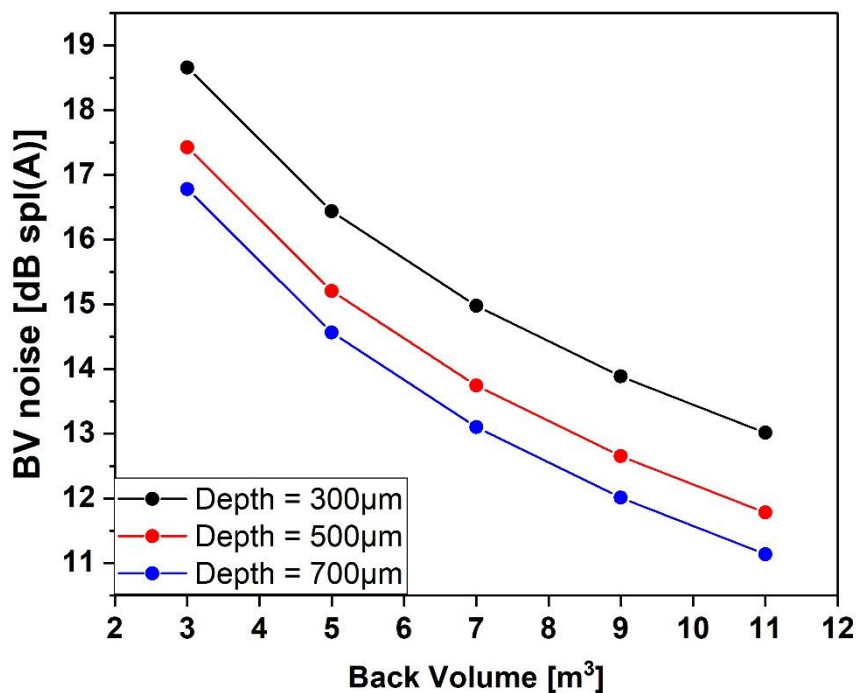


Figure 3.10: Back Volume resistance noise as a function of cavity size for different cavity depths.

### 3.2.3. Linearity

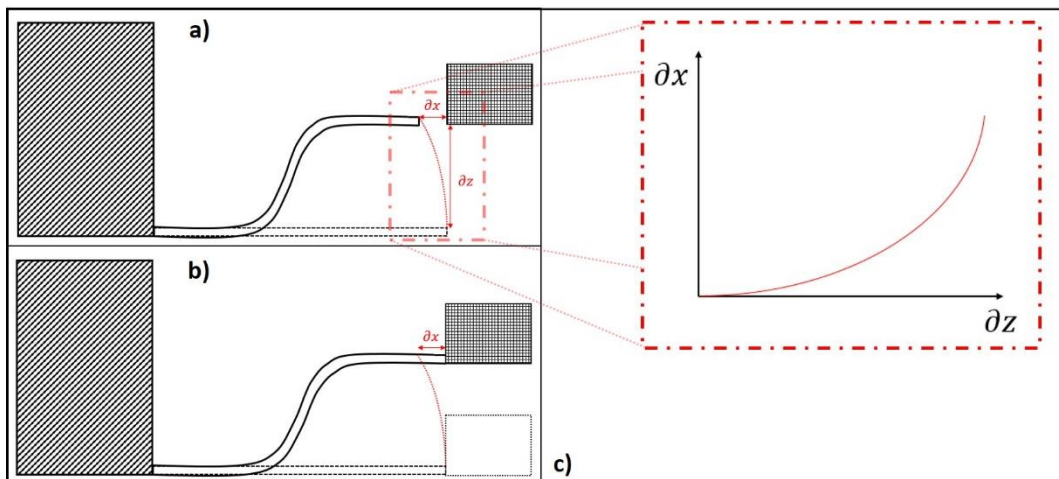
Sources of nonlinearity and consequent signal distortion stem from both the **MEMS** microphone sensor and the signal amplifying electronics. At any given Sound Pressure Level (**SPL**), these nonlinearity sources should therefore be limited so as not to surpass the acceptable signal distortion limit. Two main nonlinearity sources can be found at the **MEMS** level, one due to the chosen capacitive transduction scheme and the other due to the geometric deformation of the mechanical structure. By considering these sources during the design process, their

contributions can be limited, ensuring a small overall contribution from the **MEMS** sensor to the total signal distortion.

## Geometric nonlinearity

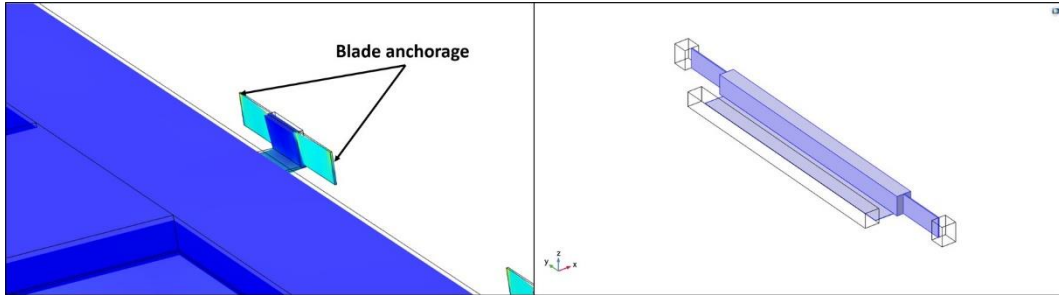
In order to ensure the validity of the initial hypothesis of a strictly out-of-plane translational movement for the piston and the electrode, Out-of-Plane mechanical Springs (**OPS**) are placed all around the perimeters of both parts of the mechanical structure. As explained later in this chapter, these springs are positioned in such a way that they reject any in-plane motion, maintaining a strictly out-of-plane movement. They also counteract the spring softening effect on the electrode as well as oppose the effects of the pressure difference applied on the piston to reach the required displacement. Since the **AVATRAM** has been designed to exhibit a very high flexibility, the **OPSs** make up the main contributors to the total stiffness of the structure. It is therefore important to make certain that, when they undergo deformations during device operation, the springs' response in terms of stiffness remains within the bounds of the acceptable nonlinearity.

For a better understanding of the source of the problem, we consider first the simple case of a single thin plate serving as a spring structure. The plate is connected to a moving object on one side and to a fixed structure on the other. Whenever the object moves out of plane, the plate undergoes flexion as it is forced to follow and accommodate the object's movement, which leads to an in-plane stretching of the plate (**Figure 3.11.a and Figure 3.11.b**). However, as it can be seen in **Figure 3.11.c**, the in-plane deformation (stretching) varies nonlinearly with the out-of-plane movement. This means that, even if both in-plane and out-of-plane stiffnesses are linear, the response of the membrane, i.e. the spring force it exerts on the moving object, is nonlinear, varying greatly as a function of the out-of-plane displacement. The same problem is also encountered whenever beams are used as spring structures.



**Figure 3.11: Case of a single membrane used as a spring. During an out-of-plane movement, the membrane undergoes flexion and in-plane stretching (a) and (b). The stretching is then found to be nonlinear (c).**

To remedy the problem of the single plate's nonlinear response, the in-plane stretching can be reduced by connecting the plate in series to another spring, exhibiting a much higher in-plane flexibility. Instead of the fixed substrate, the plate can be connected to a suspended block, which is then fixed to the substrate via two narrow torsion blades (**Figure 3.12**). In this case, when the moving object is set in motion, its movement is opposed by the flexion of the plate and the torsion of the blades. Thanks to their relatively low in-plane stiffness, the blades can absorb the nonlinear deformation that would have otherwise been incurred by the plate had it been directly connected to a fixed substrate. This serves to greatly reduce the geometric nonlinearity of the **OPS**.



**Figure 3.12: Simulation result of the OPS (left) and 3D model of the OPS showing the blade anchorage and the movable block connected to the plate in wireframes (right).**

The design of these **OPSs** makes use of the different layer thicknesses allowed by the M&NEMS fabrication process. The plate is therefore etched from the  $1\ \mu\text{m}$  thick monocrystalline Top-Si, while the block and its suspending blades are etched from the  $20\ \mu\text{m}$  thick epitaxial growth. This leaves a few degrees of freedom by which the spring stiffness can be tuned, which are the width and length of the plate as well as the length of the blades. As for the width of the blades, it is set to  $1\ \mu\text{m}$ , the minimum value allowed by the **DRIE** of the epitaxial growth. This is done to reduce as much as possible the in-plane stiffness of the blades, similarly to the previously discussed case of the **AVATRAM**'s torsion blades. Thus, the stiffnesses of the spring forces applied to the piston and the electrode ( $k_{sprg-p}$  and  $k_{sprg-e}$ ) can be set and tuned to the required values, without surpassing the maximum acceptable nonlinearity.

### Capacitive transduction nonlinearity

Capacitive transduction based on gap variation is an inherently nonlinear process, as the capacitance is inversely proportional to the gap. As we have previously shown, this leads to an attractive electrostatic force acting on the electrode, as well as a spring softening effect. However, the resulting nonlinearity has a farther reach, which can only be adequately valued by considering higher order terms. Developing the expression of the capacitance (2.18) to a third order Maclaurin series we find:

$$\begin{aligned}
C &\approx \varepsilon_0 \frac{A_{el}}{g_0} \left( 1 - \frac{dg}{g_0} + \left( \frac{dg}{g_0} \right)^2 - \left( \frac{dg}{g_0} \right)^3 \right) \\
&= C_{el} \left( 1 - \frac{dg}{g_0} + \left( \frac{dg}{g_0} \right)^2 - \left( \frac{dg}{g_0} \right)^3 \right).
\end{aligned} \tag{3.5}$$

Differentiating  $C$  by  $dg$ , and following the same steps of the development in **section 2.2.1**, we find that the sum of external forces applied to the electrode becomes:

$$\begin{aligned}
\sum F_{ext-e} &= 2\varepsilon_0 A_{el} \frac{U_{pol}^2}{g_0^3} dg + 4\varepsilon_0 A_{el} \frac{U_{pol}^2}{g_0^3} \frac{dg^3}{g_0^2} - k_{pos-e} dg \\
&= (2k_{neg} - k_{sprg-e}) dg + 4k_{neg} \frac{dg^3}{g_0^2}.
\end{aligned} \tag{3.6}$$

Although the first order nonlinearity of the spring softening effect can be opposed by the additional spring stiffness of the electrode, it is difficult to counter the effects of the cubic term by well-controlled physical phenomena. As such, it adds an attractive part to the sum of external forces, which is translated as a higher electrode displacement. This can be better understood when the sum of forces on the electrode is replaced by its new expression in the equation of motion of the total mechanical structure **(2.37)**:

$$\begin{aligned}
&(-v_{pist} R_{mecha} A_{pist}^* - P_{diff} A_{pist}^* - k_{sprg-p} \cdot z_p) \cdot D_p - \\
&\left( -k_{rem} \cdot z_e + 4k_{neg} \frac{z_e^3}{g_0^2} \right) \cdot D_e - C_{avat} \cdot \theta = I_{tot} \cdot \ddot{\theta}.
\end{aligned} \tag{3.7}$$

Keeping in mind that  $z_p = -\gamma z_e$  and  $\gamma = D_p/D_e$ , the equation can be rewritten at equilibrium as:

$$P_{diff} A_{pist}^* = \left( \gamma k_{sprg-p} + \frac{k_{rem}}{\gamma} + \frac{C_{avat}}{D_p D_e} \right) z_e - 4k_{neg} \frac{z_e^3}{\gamma g_0^2}. \tag{3.8}$$

Therefore, the cubic term is a force that affects the response of the mechanical structure, directly affecting the sensitivity of the device. Thus, considering the simple case of a very large **BV** ( $k_{BV} \approx 0$ ), the equation can be simplified to:

$$\underbrace{\frac{P_{diff} A_{pist}^*}{k_{tot}}}_{\tilde{z}_e} = z_e - \frac{4k_{neg}}{\gamma g_0^2 k_{tot}} z_e^3. \tag{3.9}$$

At this point, the additional displacement due to the third order nonlinearity can be clearly discerned. Recognizing that the left hand side of the equation is none other than the expected linear displacement  $\tilde{z}_e$  at a given pressure difference, the real displacement of the electrode can thus be approximated as:

$$z_e \approx \tilde{z}_e + \varphi \tilde{z}_e^3, \tag{3.10}$$

where  $\varphi = \frac{4k_{neg}}{\gamma g_0^2 k_{tot}}$ . The additional effect of this displacement is cumulated with the capacitive nonlinearity and can be quantified by studying the resulting differential variation of capacitance:

$$\Delta C = (C(-z_e) - C(0)) - (C(z_e) - C(0)) = 2C_{el} \cdot \left( \frac{z_e}{g_0} + \frac{z_e^3}{g_0^3} \right). \quad (3.11)$$

Replacing the real displacement of the electrode with its expression we find:

$$\Delta C = 2 \frac{C_{el}}{g_0} \cdot \left( \tilde{z}_e + \varphi \tilde{z}_e^3 + \frac{(\tilde{z}_e + \varphi \tilde{z}_e^3)^3}{g_0^2} \right), \quad (3.12)$$

which, in accordance with the initial small gap variation consideration, can be simplified to:

$$\Delta C \approx \underbrace{2 \frac{C_{el}}{g_0} \tilde{z}_e}_{Lin} \left( 1 + \underbrace{\tilde{z}_e^2 \cdot \left( \varphi + \frac{1}{g_0^2} \right)}_{NL} \right) \approx \underbrace{2 \frac{C_{el}}{g_0} \tilde{z}_e}_{Lin} \left( 1 + \underbrace{\frac{\tilde{z}_e^2}{g_0^2} \cdot \left( \frac{4k_{neg}}{\gamma k_{tot}} + 1 \right)}_{NL} \right). \quad (3.13)$$

The total variation of capacitance is composed of a part varying linearly with the capacitance change (Lin), and a nonlinear part (NL) that varies with the nonlinear capacitance change. Moreover, NL is further amplified by the ratio of the compound spring softening effect to the total stiffness of the structure. Controlling this ratio is therefore crucial for controlling the amount of added capacitive nonlinearity. A simple way to do so is by defining a maximum to the nonlinear part  $NL_{max}$ , not to be surpassed at the maximum capacitive variation. This sets a minimum for the total stiffness of the structure:

$$k_{tot} \geq \frac{4k_{neg} \tilde{z}_{e_n}^2}{\underbrace{\gamma (NL_{max} - \tilde{z}_{e_n}^2)}_{k_{tot_{min}}}}, \quad (3.14)$$

where  $\tilde{z}_{e_n}$  is the normalized maximal gap variation. Thus, the capacitive transduction through gap variation sets the lower limit of the structure's total stiffness, and  $k_{tot}$  should be increased beyond  $k_{tot_{min}}$ . For a given  $\tilde{z}_{e_n}$  at a maximum pressure  $P_{max}$ , this can only be achieved by increasing the size of the piston. More specifically, when  $k_{tot}$  is replaced by its expression given in **equation (3.9)**, a minimum piston area can be determined:

$$A_{pist}^* \geq \frac{4C_{el} U_{pol}^2 \tilde{z}_{e_n}^3}{\underbrace{\gamma g_0 (NL_{max} - \tilde{z}_{e_n}^2) P_{max}}_{A_{pist_{min}}^*}}, \quad (3.15)$$

Finally, since the stiffness of the structure is a determining factor in the remaining performance parameters, this simplifies the design process as the maximum acceptable nonlinearity  $NL_{max}$  sets guidelines for the design of the final structure.

### 3.2.4. Resonance Frequency

The previously found expression of the resonance frequency can be rewritten in terms of the total stiffness of the mechanical structure:

$$\omega_0 = \sqrt{\frac{k_{tot}\gamma}{(m_p\gamma^2 + \frac{m_{Dp}}{3}\gamma^2 + m_e + \frac{m_{De}}{3})}} = \sqrt{\frac{P_{max}A_{pist}^*\gamma}{\tilde{z}_e(m_p\gamma^2 + \frac{m_{Dp}}{3}\gamma^2 + m_e + \frac{m_{De}}{3})}}. \quad (3.16)$$

Consequently, the lower limit of  $k_{tot}$  defined by the maximum acceptable nonlinearity defines a minimum resonance frequency:

$$\omega_0 \geq \underbrace{\sqrt{\frac{4k_{neg}\tilde{z}_{en}^2}{(NL_{max} - \tilde{z}_{en}^2)(m_p\gamma^2 + \frac{m_{Dp}}{3}\gamma^2 + m_e + \frac{m_{De}}{3})}}}_{\omega_{0min}}. \quad (3.17)$$

Thus, the capacitive transduction also determines the lower limit of the resonance frequency  $\omega_{0min}$ . Since  $\omega_0$  varies with  $k_{tot}$ , for a fixed maximum electrode displacement at  $P_{max}$ , the resonance frequency of the microphone can only be increased with a larger piston size.

### 3.2.5. Sensitivity

In contrast to the resonance frequency, the sensitivity is inversely proportional to the total stiffness of the structure:

$$Sense_{\Delta Q} \approx \frac{\varepsilon_0 A_{el} U_{pol}}{g_0^2} \cdot \frac{A_{pist}^*}{k_{tot}}. \quad (3.18)$$

If we consider again the case of a set maximum electrode displacement  $\tilde{z}_{en}$  at a maximum pressure  $P_{max}$ , the sensitivity can be rewritten as:

$$Sense_{\Delta Q} \approx C_{el} U_{pol} \cdot \frac{\tilde{z}_{en}}{P_{max}}. \quad (3.19)$$

The expression of sensitivity is then simplified to a variation of charges divided by the maximum applied pressure. Thus, the sensitivity can be determined and remain unchanged, while  $k_{tot}$  and  $\omega_0$  are increased to meet the required values.

In conclusion, in view of the limitations of the fabrication process and transduction nonlinearity, the size of the piston is the common thread linking all performance parameters of the device. Once the capacitance and electrode displacement at maximum pressure are determined, the sensitivity is set, and the noise and **BW** of the microphone can be optimized by the correct choice of piston size. Once again, one of the principal interests of this new microphone design is underlined: the



capacitive transduction and the harvesting of the acoustic signal can be separately optimized, removing the need for any tradeoff in terms of performance.

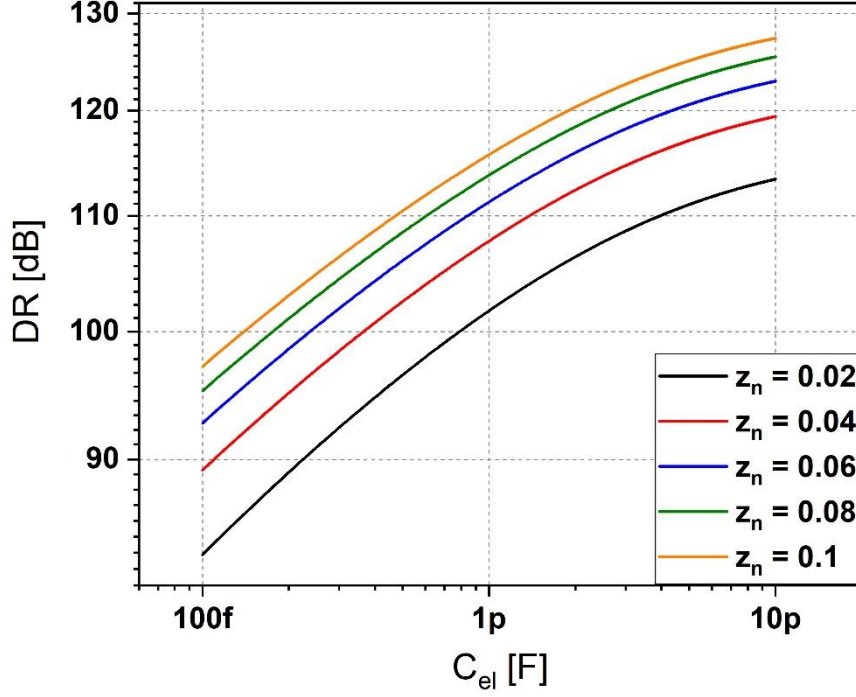
## 3.3. Microphone Design Process

The design process of any **MEMS** sensor can be undertaken differently depending on the set requirements for the final device. As the main objective for this new microphone design is to increase the overall performance, a performance driven design process was chosen and developed. This method consists in establishing first the targeted performance parameters and then designing the sensor accordingly. Alternatively, a different design process can be exemplified by one that is motivated by size limitation, for which the final device size is considered as the main and initial constraint.

### 3.3.1. Initial design parameters

The performance driven design process starts by defining the required microphone performance in terms of total noise and **AOP**. By definition, these two parameters define the microphone's **SNR** as well as its dynamic range **DR**, which is the ratio of the maximum signal readable by the **MEMS** sensor to its total noise. The circuit chosen for this design process is detailed in **Appendix C**. Although other circuits and architectures can be used, such as a simple instrumentation amplifier, the charge amplifier circuit was privileged for its low noise, made possible by the modulation of the polarization signal at high frequency. Hence, as further explained in **Appendix C**, by choosing the maximal variation of capacitance required by the electronic circuit, the **DR** could be reached. In other words, the chosen maximal signal variation ensures that the electronic noise is not a limiting noise source for the microphone.

Based on the calculation explained in **Appendix C**, **Figure 3.13** shows an example of the variation of the **DR** as a function of the signal capacitance for different normalized maximal gap variations  $\tilde{z}_{e_n}$  and at a polarization amplitude of 15 V. As expected, the signal capacitance required to reach a given **DR** can be reduced with a larger gap variation. For a given capacitance gap  $g_0$ , this would go in the desirable direction of a reduction in the size of the electrode and the device. However, as it affects the sensitivity and the resonance frequency of the microphone,  $\tilde{z}_{e_n}$  is a degree of freedom that should be carefully chosen considering its effect on the other performance parameters. **Table 3.1** recapitulates the main expressions of the microphone parameters. In these expressions,  $NL_{max}$  and  $P_{max}$  are set at the start of the design process by the required **AOP**. We do however note that  $NL_{max}$  can be changed depending on the part of nonlinearity allocated to the **MEMS** sensor. For higher clarity, the design process and the influence of all variables on the final performance parameters are illustrated in **Figure 3.14**.



**Figure 3.13: Variation of the DR of the electronic circuit as a function of the signal capacitance for different normalized maximum gap variations.**

When increased, the polarization amplitude  $U_{pol}$  has a positive effect on the sensitivity and on the **DR**. However, it also results in a twofold augmentation of the minimum piston size, which is the reason behind the increase of the minimum resonance frequency. Therefore,  $U_{pol}$  should be set high enough to increase the sensitivity and meet the **DR** requirement at a reasonable signal capacitance, but still low enough to maintain a small piston size. We add that, industrially, a lower polarization amplitude is preferred for circuitry limitations and power consumption considerations. For these reasons, the polarization amplitude considered during the design process was set at 15 V, keeping in mind the possibility of a later adjustment if necessary.

$Sense_{\Delta Q}$	$\omega_0$	$k_{tot}$	$A_{elec}$	$A_{pist_{min}}^*$
$\frac{C_{el}U_{pol}\tilde{z}_{e_n}}{P_{max}}$	$\sqrt{\frac{k_{tot}\gamma}{(m_p\gamma^2 + \frac{m_{Dp}}{3}\gamma^2 + m_e + \frac{m_{De}}{3})}}$	$\frac{P_{max}A_{pist}^*}{\tilde{z}_e}$	$\frac{C_{elec}g_0}{\epsilon_0}$	$\frac{4C_{el}U_{pol}^2\tilde{z}_{e_n}^3}{\gamma g_0(NL_{max} - \tilde{z}_{e_n}^2)P_{max}}$

**Table 3.1: Expressions of main microphone parameters.**

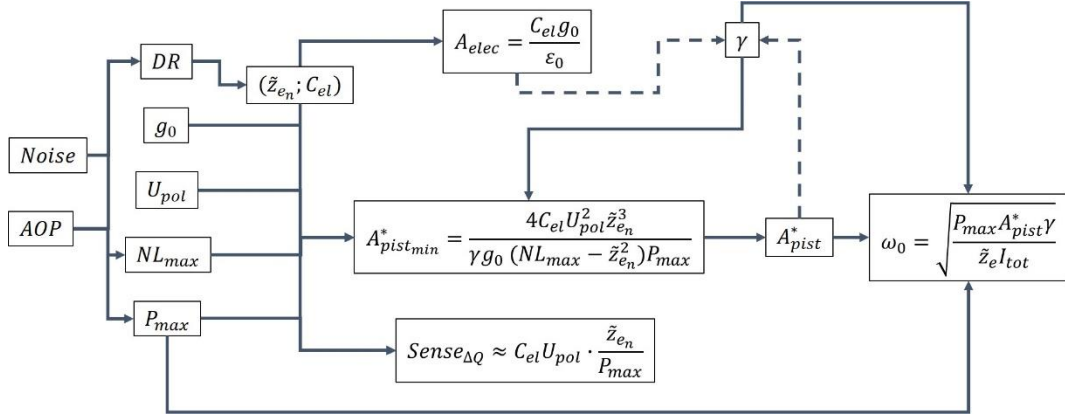
At first glance, the same reasoning seems to apply to the capacitance gap, since the surface of the electrode can be reduced with a smaller  $g_0$  while maintaining the same capacitance. This would also equally increase the minimum size of the piston, leading to an approximately unchanged total device size. However, a great benefit to reducing  $g_0$  hides in the fact that  $\tilde{z}_{e_n}$  can be reached for a smaller maximum electrode displacement. This can therefore be used as way to increase  $k_{tot}$  and  $\omega_0$

without increasing the total device size. As previously specified, during the presentation of the fabrication process, the capacitance gap is set at  $1 \mu m$ , which is the thickness of the **BOX** and the first deposited SiO<sub>2</sub> layer. This decision was also partly motivated by the fact that fabrication variabilities can have dire consequences at smaller gap sizes. For a small gap, even a small variation during the deposition of the first SiO<sub>2</sub> layer can lead to a big difference between the gaps of the top and bottom electrodes, which would destabilize the structure and lead to a low pull-in voltage.

Concerning the  $\gamma$  factor, it only depends of the final dimensions of the device. It is therefore not possible to determine the value of  $\gamma$  at the start of the design process. However, as concluded in **Chapter 2**, a small  $\gamma$  factor serves to increase the total stiffness and the resonance frequency of the structure. Although this may not be directly apparent from the developed expressions in **Table 3.1**, it can be clarified by considering the linear piston displacement  $\tilde{z}_p = -\gamma\tilde{z}_e$ . For a given electrode displacement, decreasing  $\gamma$  means a lower piston displacement, which is translated by an increase in the spring stiffness of the entire structure.

Finally, with the design elements thus defined, the sensitivity and the minimum values for the piston area and resonance frequency can be calculated for different  $(\tilde{z}_{e_n}, C_{el})$  couples and for different discrete values of  $\gamma$ . The resonance frequency and the total stiffness can then also be calculated by considering a piston size greater than the minimum limit. A computing software can easily carry out these calculations, tabling for each  $[(\tilde{z}_{e_n}, C_{el}), \gamma]$  the expected values. Furthermore,  $\omega_0$  and  $\omega_{0_{min}}$  can only be approximated at this point, since the exact dimensions and masses of the piston, the electrode and the connecting levers are yet to be set. Thus, based on these calculated values,  $A_{pist}^*$ ,  $\tilde{z}_e$ ,  $A_{el}$  and  $\gamma$  can be chosen, which represent the initial design parameters.

However,  $A_{pist}^*$  should also be chosen depending on the required noise limit. Since the electronic circuit's noise is no longer a dominant noise with the choice of  $(\tilde{z}_{e_n}, C_{el})$ , the noise of the mechanical sensor should also not surpass the required noise limit. The size of the piston should therefore also be determined based on its effect on the slit and mechanical resistance noise (**Figure 3.9**). Moreover, the size of the **BV** remains a degree of freedom that depends on the required noise limit (**Figure 3.10**). If the **BV** noise is dominant, the size of the piston can be chosen based only on the requirements set by  $[(\tilde{z}_{e_n}, C_{el}), \gamma]$  and on size constraints. As there are a few approximations made during this first stage of the design process, the obtained initial design parameters should only be considered as rough guidelines for the final device.



**Figure 3.14: Design diagram showing the influence of all design variables on the microphone performance parameters.**

Let us consider the example of a microphone for which the desired **AOP** and noise limit are at 135 *dBspl* and 18 *dB(A)* respectively. The expected **SNR** of the microphone is therefore at 76 *dB(A)* with a **DR** of 117 *dB*. The **AOP** sets  $P_{max}$  at 112.5 *Pa*, and  $NL_{max}$  is set at 0.1. Although this means that an upper limit of 10% is considered for the nonlinearity of the **MEMS** at the maximum pressure, the actual **NL** will not necessarily reach that limit. By feeding these requirements into the computing software, the performance parameters and their limits can be calculated for each  $(\tilde{z}_{e_n}, C_{el})$  couple that ensures the **DR**, and for different  $\gamma$  factors. Studying the tabled values for each  $[(\tilde{z}_{e_n}, C_{el}), \gamma]$ , the initial design parameters can be chosen so that the desired performance is met for a small device size, which is estimated by adding the surfaces of the electrode and the piston. The parameters chosen for this example are given in **Table 3.2**.

$\tilde{z}_{e_n}$	$C_{el}$	$\gamma$	$Sense_{\Delta Q}$	$A_{pist_{min}}^*$	$A_{pist}^*$	$k_{tot}$	$\omega_0/2\pi$
0.1	1.25 <i>pF</i>	1.5	16.67 <i>fC/Pa</i>	0.074 <i>mm</i> <sup>2</sup>	0.425 <i>mm</i> <sup>2</sup>	478 <i>N/m</i>	$\approx 35$ <i>kHz</i>

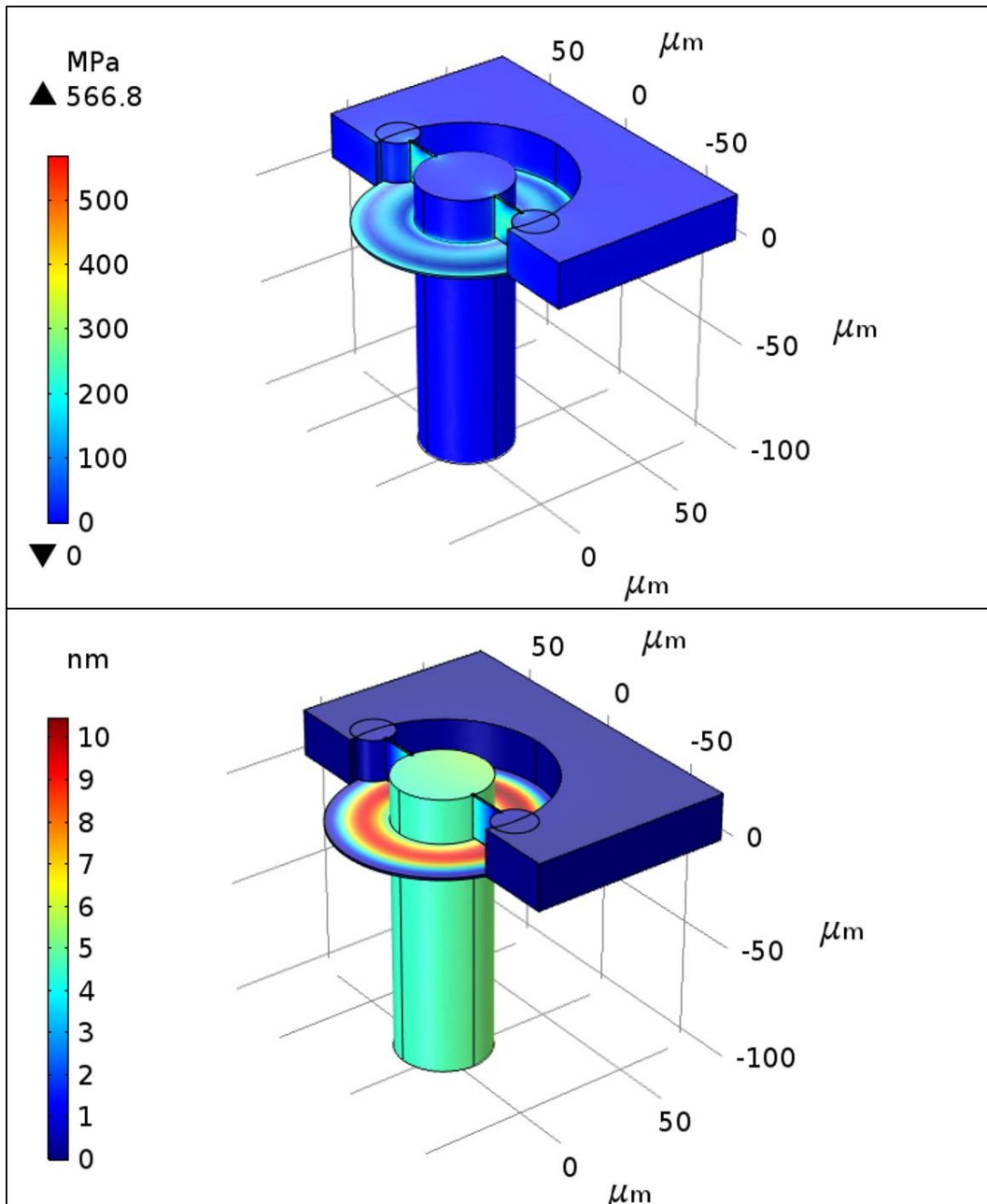
**Table 3.2: Calculated and chosen initial design parameters.**

As it can be noticed by the difference between  $A_{pist_{min}}^*$  and  $A_{pist}^*$ , the chosen piston size is much larger than the limit. This is done to increase the total stiffness and the estimated resonance frequency of the structure. This also reduces the mechanical and slit resistance noise below the required noise limit. Additionally, this decreases the nonlinearity at  $P_{max}$  to  $NL = 0.025$ , calculated from the expression given in **equation (3.13)**. The contribution of the sensor to the signal distortion has therefore been much reduced, leaving room for the contribution of the electronic circuit. Thus, the design of each element of the microphone can now be done based on the rough guidelines drawn by these initial design parameters.

### 3.3.2. AVATRAM Dimensions

The dimensions given to the **AVATRAM** are chosen based on the method presented in **Chapter 2**, with the same objectives of high flexibility and robustness applied to a plate thickness of 1  $\mu m$ . A plate radius  $R_{plt}$  of 45  $\mu m$  was selected, to

moderate the space taken by the hinge, with a pillar radius  $R_{pil}$  of  $20\ \mu\text{m}$  giving a  $\alpha = 0.44$  within its range of validity. The torsion blades holding the pillar on its vacuum side were given a length of  $18\ \mu\text{m}$  ensuring the hinge's robustness at 10 bars and high flexibility with a total rotational stiffness  $C_{avat} = 1.47\ \mu\text{N} \cdot \text{m}/\text{rad}$ . Simulation results prove the robustness of the final structure and the validity of the theoretical design of the hinge: under 10 bars of pressure, the maximum stress remains below the  $600\ \text{MPa}$  limit, and the vertical displacement of the pillar under atmospheric pressure is of around  $4\ \text{nm}$  only.



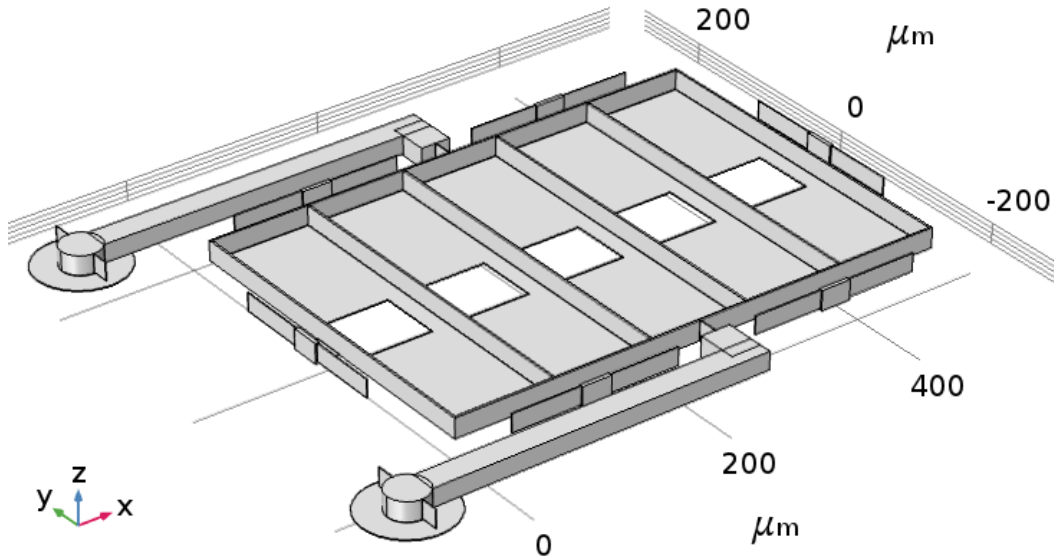
**Figure 3.15: Simulation results of the AVATRAM with the chosen dimensions, showing the Von Mises Stress under 10 bars of pressure (top), and the displacement under atmospheric pressure (bottom).**

### 3.3.3. Electrode Design

The design of the movable electrode starts by calculating the electrode surface required to reach  $C_{el}$ . However, it is important to add reinforcement beams to the electrode plate, so that it can be connected to the rest of the mechanical structure and to reduce as much as possible any deformation during its movement. Therefore, the electrode surface obtained from  $C_{el}$  should be increased to account for the added reinforcement beams on the structure: these beams are formed from the thick epitaxial growth layer, which means that they reduce the surface and the capacitance of the top counter-electrode. As it can be seen on the 3D model shown in **Figure 3.16**, the **OPS**'s are placed all around the perimeter of the electrode, strongly opposing any in-plane movement to impose a strictly out-of-plane gap variation. These springs are designed so that their combined added stiffness  $k_{sprg-e}$  is larger than the compound spring softening effect. Furthermore, on two of its sides, beams connect the electrode to two **AVATRAMEs**. These beams are connected to the electrode via two torsion blades, to decouple the rotational movement of the beams from the out-of-plane displacement of the electrode. More precisely, if the added rotational stiffness of the blades  $C_{dcpl}$  is considered, the sum of external forces applied to the electrode given in **equation (2.21)** becomes:

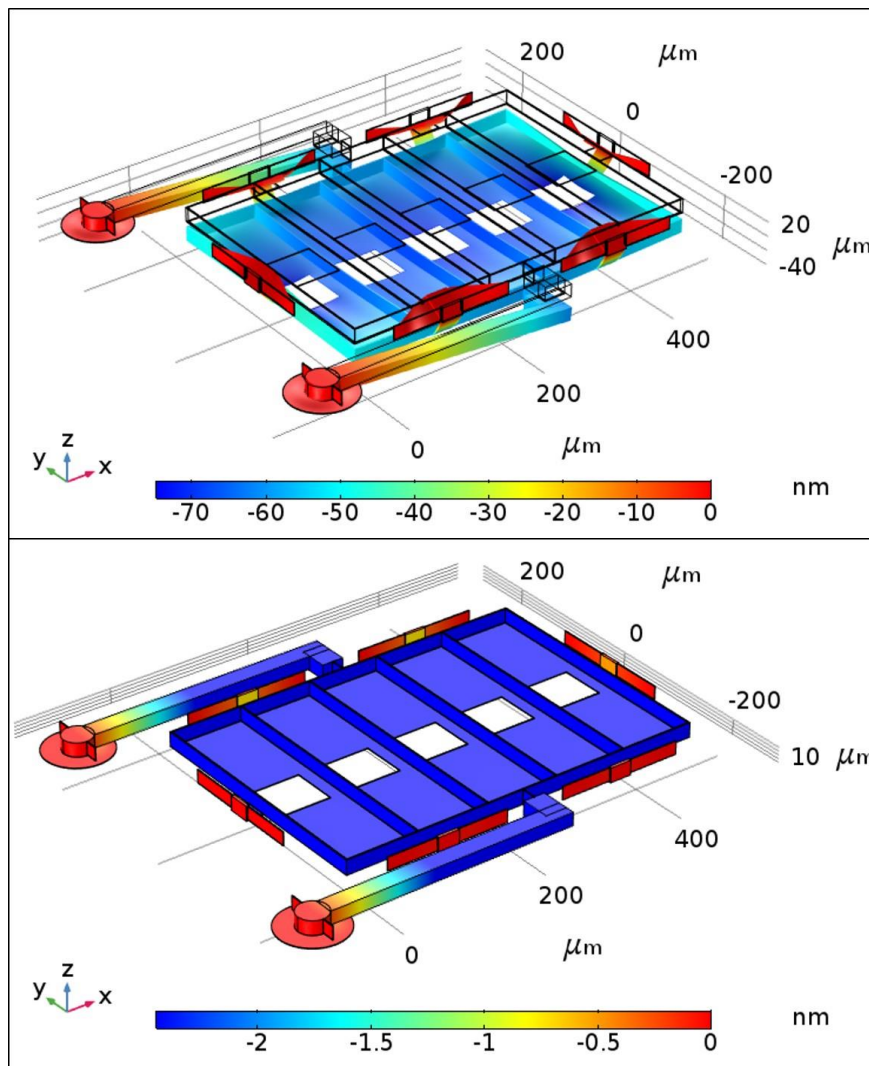
$$\Sigma F_{ext-e} = (2k_{neg} - k_{sprg-e})z_e + \frac{C_{dcpl}}{D_e} \theta = (-k_{rem} - \frac{C_{dcpl}}{D_e^2})z_e . \quad (3.20)$$

Since  $C_{dcpl}$  is very low, the rotational blades will undergo an in-plane deformation to accommodate the rotation of the beams. However, given their high out-of-plane stiffness due to their considerable thickness, they still transfer the out-of-plane movement to the electrode.



**Figure 3.16: 3D model of the electrode design.**

Thus, for the presently discussed design, the total electrode surface was increased from  $0.14 \text{ mm}^2$  (calculated from equation (1.1) for a capacitance of  $1.25 \text{ pF}$ ) to  $0.17 \text{ mm}^2$  to account for lost space. This is done as a precautionary measure, in order to make sure that the required active capacitance surface of  $0.14 \text{ mm}^2$  is reached so that the **DR** requirement is met. Moreover, although this would increase  $D_e$  and go in the desired direction of a smaller  $\gamma$ , it also increases the length of the beams connecting the AVATRAMs to the electrode. We note that if the length is increased too far, it can weaken the beams and lead to their deformation during the operation of the structure. Therefore, for the chosen  $502 \mu\text{m} \times 350 \mu\text{m}$  rectangular electrode design,  $D_e$  was set at  $387 \mu\text{m}$ , and the final value of the capacitance was around  $1.38 \text{ pF}$  between the movable electrode and the bottom counter-electrode, and  $1.25 \text{ pF}$  with the top counter-electrode. This inevitable imbalance between the two capacitances leads to a higher electrostatic force attracting the movable electrode towards the bottom counter-electrode and changing the capacitance gaps. The effect of the unbalanced electrostatic forces can be seen in **Figure 3.17**, with an average electrode displacement of  $60 \text{ nm}$ . This



**Figure 3.17:** Electrode deformation due to the unbalanced electrostatic force, without (top) and with (bottom) a patterned counter-electrode and an adapted fabrication process.



shows the importance of adapting the fabrication process to the new device (**Figure 3.7**), as by increasing the gap underneath the electrode's reinforcements, the additional electrostatic force can be drastically decreased, leading to an average displacement of only  $2.5 \text{ nm}$ . In an effort to account for the difference in capacitance gaps, the electrode displacement was set at  $z_e = 98 \text{ nm}$ .

### 3.3.4. Final Structure

The design of the piston is simplified by the fact that  $A_{pist}^*$  is determined at the start of the process. The only two remaining variables are the piston stiffness  $k_{sprg-p}$  and the distance  $D_p$  between the center of the piston and the **AVATRAMs'** axis of rotation. Ideally,  $D_p$  should be decreased in order to decrease  $\gamma$  (**section 3.3.1**), however, there is a limit to how close to the **AVATRAMs** the piston can be placed. In fact, in order to reach a high level of vacuum within the cavity, the vacuum seal should have a minimum width of  $200 \mu\text{m}$ , a limitation imposed by the fabrication process. The **AVATRAMs** are therefore placed as close as possible to the inner edge of the cavity, to decrease the distance to the middle of the piston, which is placed right at the outer edge of the vacuum seal. The smallest possible distance for this design was chosen with  $D_p = 521 \mu\text{m}$ . Hence, even though initially the  $\gamma$  factor was considered at 1.5, it was possible to reduce it to 1.34.

With this new value for  $\gamma$ , the remaining  $k_{sprg-p}$  can be calculated from the expression of  $k_{tot}$  given in **equation (2.62)**:

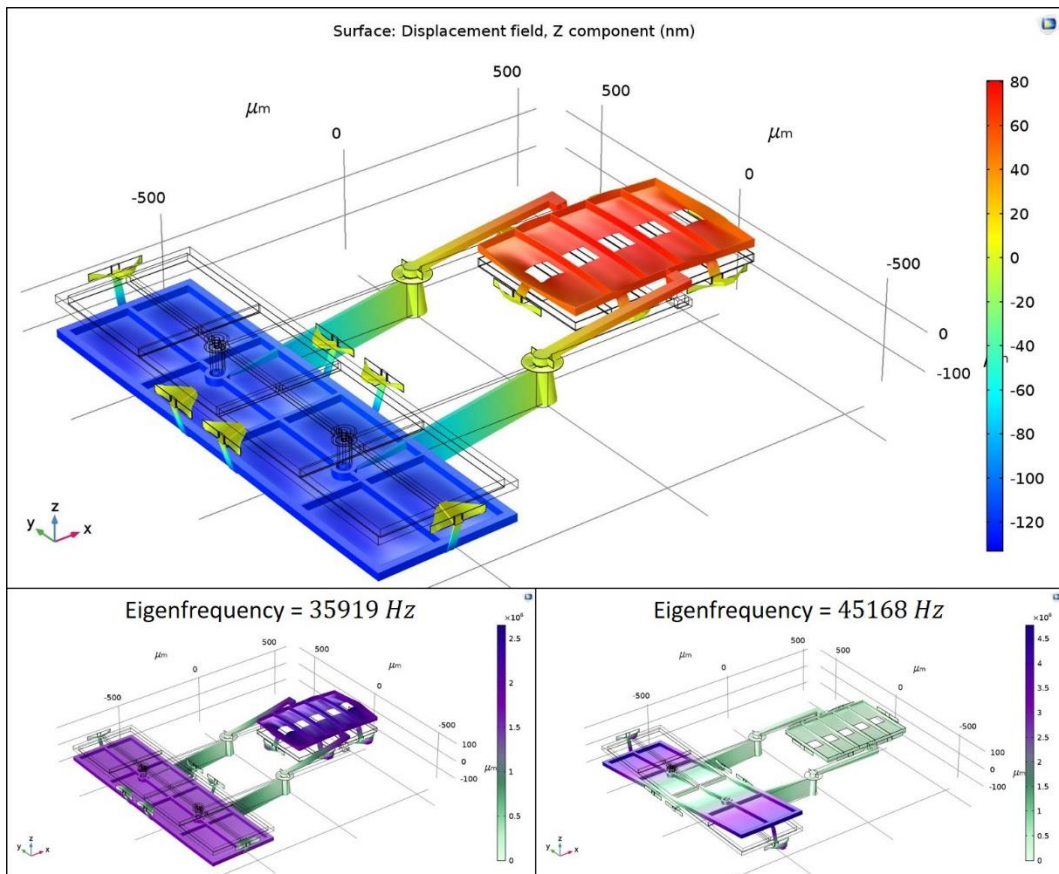
$$k_{sprg-p} = \frac{k_{tot}}{\gamma} - k_{BV} - \frac{k_{rem}}{\gamma^2} - \frac{2C_{avat}}{D_p^2}. \quad (3.21)$$

The equivalent stiffness of the **AVATRAMs** is known, and  $k_{rem}$  is obtained from **equation (3.20)** by considering that  $C_{dcpl}$  is negligible compared to the surplus of stiffness added by the electrode's **OPSs**, the design of which gives  $k_{rem} = 16.4 \text{ N/m}$  for this device. As for the stiffness of the **BV**, it can be calculated from its expression  $k_{BV} = A_{pist}^{*2} / C_{BV}$ , once the size of the **BV** is determined. In the case of the present design, an integrated cavity formed by the cap wafer was chosen with a volume of  $3 \text{ mm}^3$ , giving  $k_{BV} = 8.3 \text{ N/m}$ . Hence, the noise due to the **BV** will be the dominant noise source, slightly increasing the noise limit to  $19 \text{ dB}(A)$ .

The required stiffness of the piston springs can now be calculated, resulting in  $k_{sprg-p} = 330 \text{ N/m}$ . The **OPSs** can thus be designed according to this value and placed all around the perimeter of the piston, in a similar fashion to the electrode. The out-of-plane movement of the piston is also mechanically decoupled from the rotational movement of the beams connecting it to the **AVATRAMs**. This is also ensured by low rotational stiffness torsion blades. Thus, the total piston displacement is expected to be  $z_p = \gamma z_e = 126 \text{ nm}$ . As it can be seen on **Figure 3.18**, simulation results of the final structure are in good agreement with the

theoretical calculations. We do however note a slightly higher electrode displacement mainly due to the deformation of the electrode. Nevertheless, as we have previously specified, this discrepancy can be minimized by adapting the fabrication process to reduce the imbalance of the capacitances, which would also allow more robust electrode reinforcements and thereby less deformation.

On a final note, as all the elements in the structure have been designed, the resonance frequency can be calculated from its expression given in **Table 3.1**. The masses of two piston connection beams and two electrode connection beams should be taken into account. The first resonance frequency of the microphone is calculated at  $36\text{ kHz}$ , which is also in very good agreement with the simulation results. The second resonance mode is found at the much higher frequency of  $45\text{ kHz}$ , which proves that neither resonances have a limiting effect on the targeted **BW** of operation in the audible range. The microphone has thus been designed to meet the initially set performance requirements, with a total device size of  $1.92\text{ mm}^2$ .



**Figure 3.18: Simulation result of the structure's static displacement at maximum pressure applied to the piston (top), and first (bottom left) and second (bottom right) eigenmodes.**

### 3.3.5. Final Devices

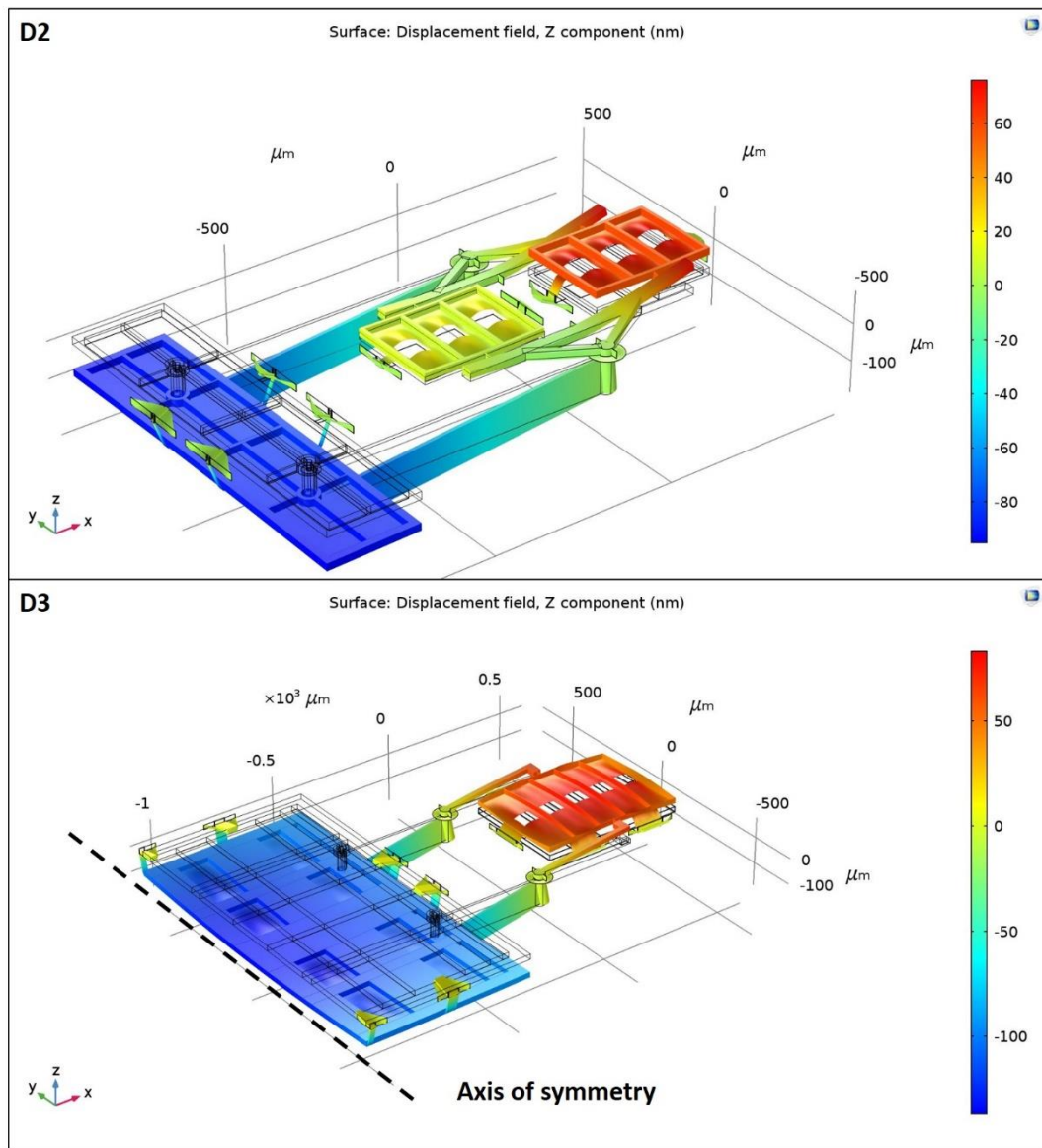
The main benefit of the chosen design process is that it ensures that the desired performance is reached, even if it is not at the optimal device size. The increase in size is mainly due to the margins taken on the sizes of the piston and the electrode, a decision justifiable by its linearization and simplification of the design process. If these margins were not to be taken, the same design process would still be possible, albeit with multiple back-and-forths between the design of each element and that of the final structure.

Furthermore, with the simplification of the design process, additional structure designs and performance parameters can be explored, to gauge the limits of this new microphone concept. Aside from the previously discussed design, hereafter denoted by **D1**, two other main structure designs (**D2 and D3**) were implemented as shown in **Figure 3.19**. The major advantage of the **D2** design is its insensitivity to the imbalance between the top and bottom capacitances, as the differential operation is performed by two electrode plates. The single electrode of **D1** is thus separated into two completely symmetrical smaller electrodes moving in opposite directions. However, the main disadvantage is that this takes more space than **D1** and can only be achieved with a larger  $\gamma$ , since the **AVATRAMs** need to be placed between the two electrode plates. As for the **D3** design, it is similar to the **D1** in its electrode design, yet differs from it at the level of the piston, which is now connected to two movable electrodes, one from each side. Although this obviously increases the size of the device, it does allow a much larger signal capacitance while keeping a small  $\gamma$  factor since the piston no longer needs to be connected at its middle. This design is thus more suited for high **DR** devices.

A multitude of devices with different expected performance levels have been designed based on the three main structure. The details of four devices are given in **Table 3.3** as an example, showing the range of performance that can be achieved with this new microphone concept, which can even be implemented for the design of an aeroacoustic microphone (Device 4).

	<i>Device 1</i>	<i>Device 2</i>	<i>Device 3</i>	<i>Device 4</i>
<i>Structure Design</i>	D1	D2	D3	D3
<i>SNR [dB(A)]</i>	76	70	77	<i>N.A</i>
<i>AOP [dBspl]</i>	135	125	140	160
<i>f<sub>0</sub> [kHz]</i>	35	22	33	105
<i>Sense<sub>ΔQ</sub> [C/Pa]</i>	$20 \cdot 10^{-15}$	$6.5 \cdot 10^{-15}$	$60 \cdot 10^{-15}$	$36 \cdot 10^{-15}$
<i>Size [mm<sup>2</sup>]</i>	1.92	1.74	5	2.51

**Table 3.3: Performance parameters of four microphone designs. All devices are expected to have a NL lower than 0.1.**



**Figure 3.19: Examples of D2 and D3 structure designs**

# Chapter 4 Results and discussion

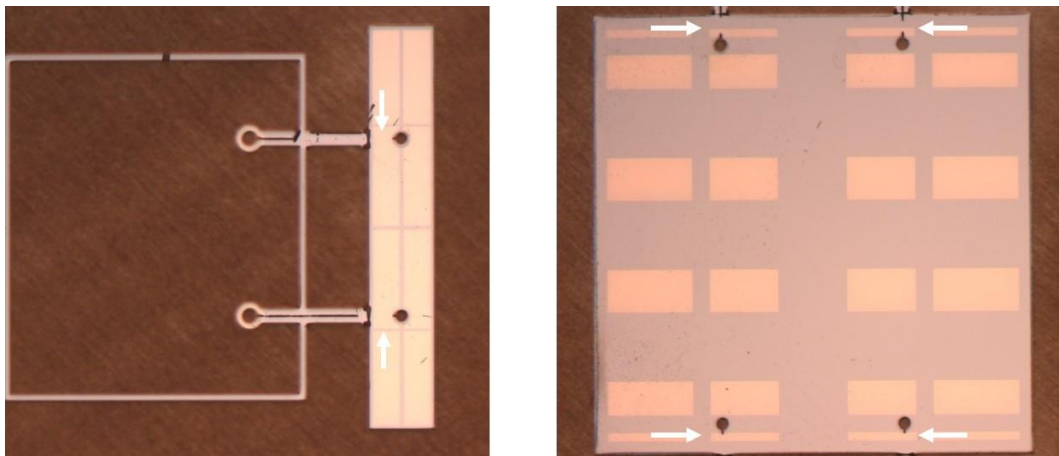
Multiple microphones with varying expected performance parameters were designed based on the previously discussed structures. The fabrication and analysis were performed on small batches of two or three 200 *mm* wafers at a time. This judicious choice gave the opportunity to perform necessary corrections in the case of unforeseen problems, since this was the first time this fabrication process was implemented for the fabrication of such devices. In this chapter, wafer-level fabrication and characterization results are presented following the progression of encountered problems and given solutions.

## 4.1. First fabrication batch

The first fabrication batch consisted of three wafers, each with a different cavity depth of 150  $\mu\text{m}$ , 250  $\mu\text{m}$  and 300  $\mu\text{m}$ . As we have previously mentioned, although they lead to larger **BVs** and better vacuum levels, a large number of deep and juxtaposed cavities can jeopardize the structural integrity of the cap wafer, possibly causing the breaking of the wafer stack. This was the case of the wafer with the deepest cavity, as the wafer stack broke during the final chemical and mechanical polishing steps, while the two other stacks remained intact.

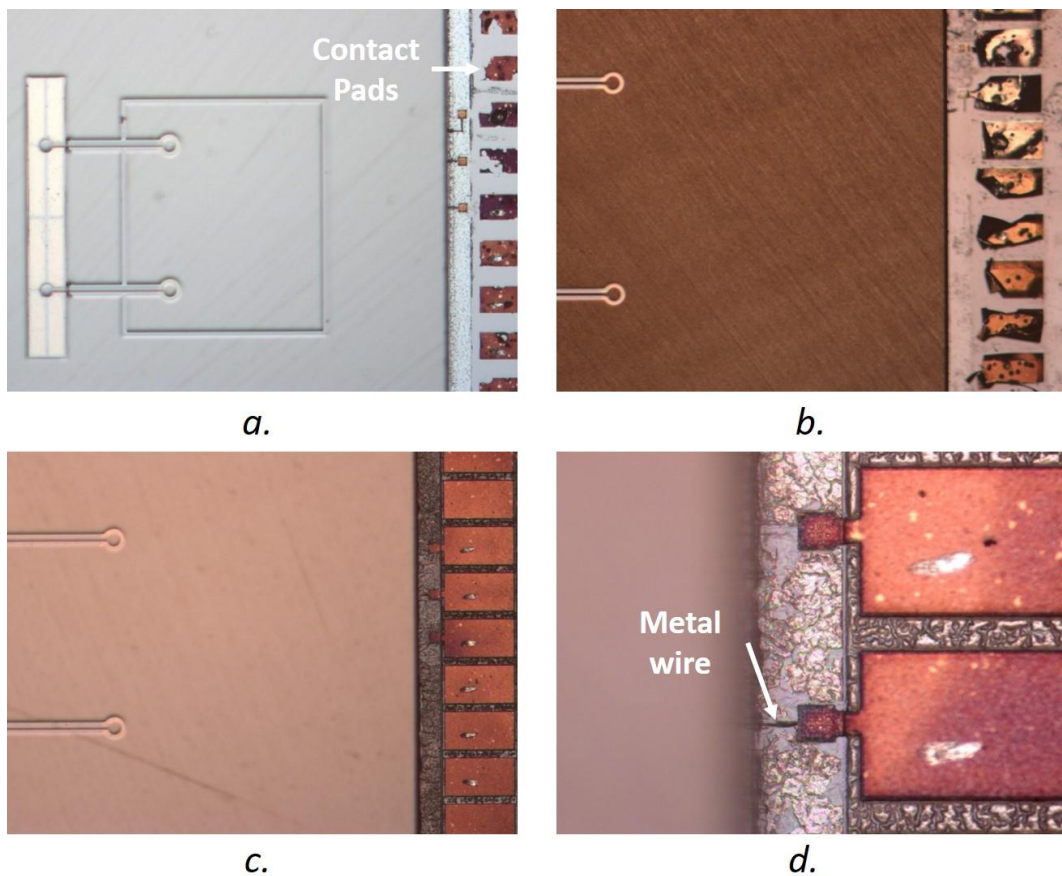
### 4.1.1. Fabrication results

Although the two remaining stacks (**ws1** and **ws2**) were structurally sound, they exhibited two visible problems, the first one being missing connection levers between the **AVATRAMs** and the pistons for a large number of devices (**Figure 4.1**). The reason behind these missing and broken levers is that, during the last step of the fabrication process, the devices are covered with an adhesive tape while parts of the wafer are sawed off to expose the contact pads. This is done to avoid the accumulation of debris on the exposed pistons. However, the tops of the piston levers strongly adhered to the tape, and many were pulled and broken when the tape was peeled off to reveal the devices. Therefore, a simple and direct solution to this minor problem is to use a less adhesive tape that would not strongly bond with the connections.



**Figure 4.1:** Optical microscopy images of the broken piston connections of two devices indicated by white arrows.

**Figure 4.2** shows optical microscopy images of contact pads in different locations on **ws1**. In some locations, the pads were severely damaged, to the point that they were either completely or partially removed from the face of the wafer (**Figure**



**Figure 4.2:** Optical microscopy images of the contact pads on **ws1**. In some locations the pads were almost entirely missing (a and b), although in other areas the contacts seemed intact (c). By zooming on these areas (d), the consumed  $\text{SiO}_2$  surrounding the pads can be seen, as well as a missing connecting wire on the top contact.



4.2.a. and Figure 4.2.b.). In other places, the contact pads seemed to be intact (Figure 4.2.c.). However, a closer inspection of these pads revealed that the SiO<sub>2</sub> layers, on which the metal layers of the cap wafer are deposited, have been chemically attacked during the fabrication process (Figure 4.2.d.). This indicates that, at some point during the process, the pads were exposed to HF vapor, which attacked and consumed the SiO<sub>2</sub> layers, to the point of fully releasing the pads in some locations. Moreover, even when it only partially consumed the SiO<sub>2</sub> layers, the exposure to HF damaged the narrow metal wires connecting the pads to the electrodes in the vacuum cavities. The same results were observed on **ws2**.

The cap wafer is only exposed to HF vapor after its bonding to the device wafer, and therefore during the last steps of the process. Furthermore, by closely observing the wafer stacks, a repetitive pattern of severely and slightly damaged contacts was found, pointing in the direction of a problem at the layout or design level. In fact, the wafer is divided into identical square fields, each one divided into four rows and four columns containing the devices (Figure 4.3). On the two wafer stacks, the pads on the second and fourth column were found to always be more damaged than the

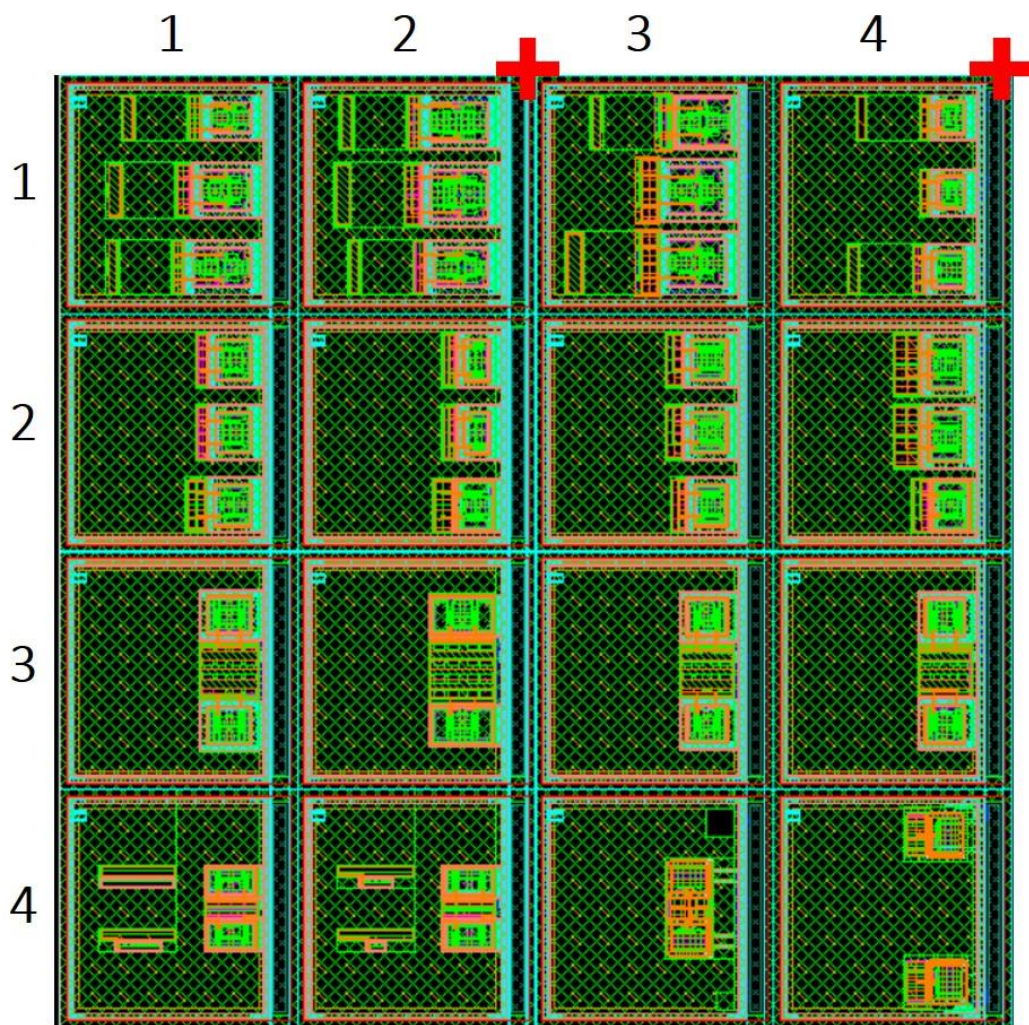


Figure 4.3: Layout showing the 4x4-field division. Red crosses indicate the position of the mask identifiers next to the second and fourth column.

others, with the ones on the first and fourth rows being almost entirely released. Among the other contacts, the ones on the third row were found to have incurred the least damage. This revealed that the problem was due to the identifiers of the mask used for the second **DRIE** step. These motifs sit at the top of the second and fourth column, and are not normally entirely etched. However, for these devices, this etching step takes more time than usual because it is used to etch the bulk-Si on the large piston surfaces. Furthermore, these designs require the thinning of the bulk-Si to  $100\ \mu\text{m}$  instead of the  $300\ \mu\text{m}$  thickness used normally in the M&NEMS process. For these reasons, the identification motifs were entirely etched. Consequently, during the subsequent release step, the HF vapor was able to infiltrate all the interconnected cavities containing the contact pads. For later batches, this problem was corrected by removing the identifier of the **DRIE** mask.

## 4.1.2. Device characterization

For a microphone to be correctly working, it evidently needs to be in good condition both mechanically and electrically. Given the encountered mechanical and electrical problems and the large number of 693 devices on each wafer stack, it was necessary to first automatically sort the working devices from the defective ones.

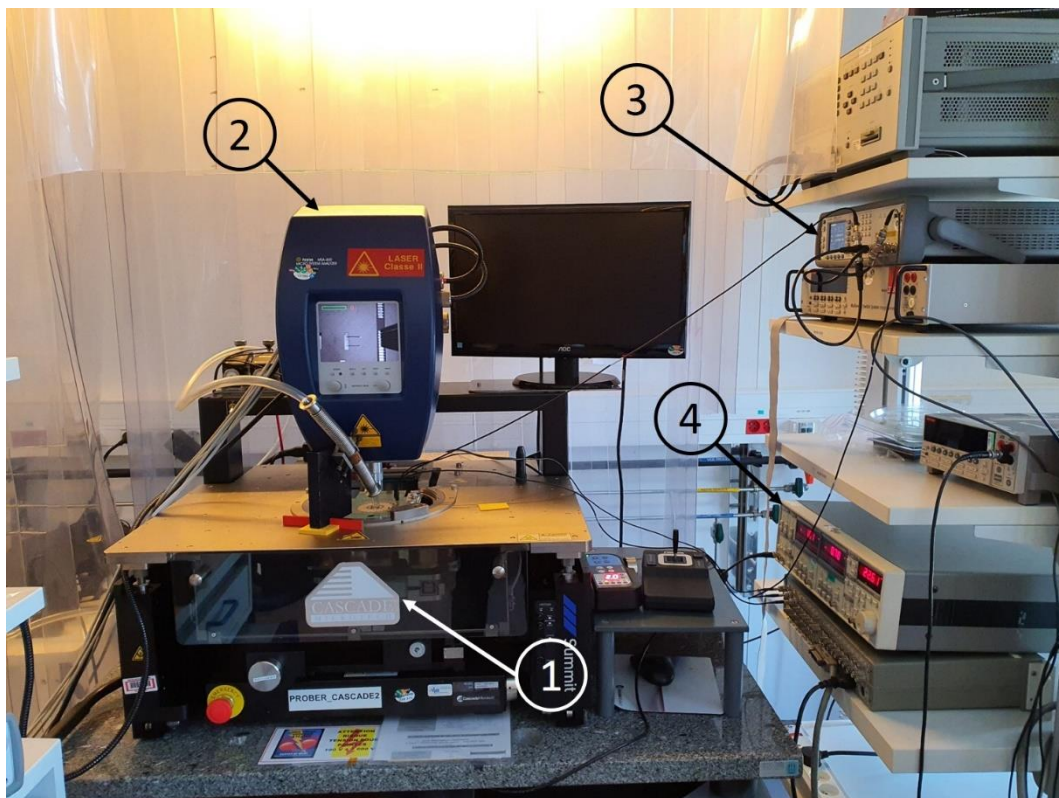
### Automatic tests

The first test performed on the wafer stacks was the measurement of the value of the capacitances of all devices. This test serves as a first sorting round of the microphones: by comparing the expected and the measured values of capacitance, the state of the electrical connectivity of each device can be decided. To do so, each wafer was placed on a semi-automatic probe station, which sequentially measured the capacitances of each device using an LCR meter (**Figure 4.4**). For example, the expected values for a device based on the **D3** structure design are around  $4\ \text{pF}$  for the top counter-electrode capacitance, and  $18\ \text{pF}$  for the bottom counter-electrode. The discrepancy between the two values is due to the higher parasitic capacitances with the bottom electrode, caused by the remaining **BOX** ensuring the vacuum in the cavity. This difference is also present experimentally, with average values of  $7.8\ \text{pF}$  and  $24.9\ \text{pF}$  measured for the top and bottom counter-electrodes respectively for this device type. The values are higher than expected, due to additional parasitic capacitances caused by the electrical wiring of the device and the remaining parts of **BOX** surrounding the cavity. Still, with these results the measured device can be considered as having good electrical connections. In the opposite cases, the measured values for capacitances were either negative, or an order of magnitude higher than expected. Thus, the analysis of the first test's results showed that the number of devices that can be expected to have good connections is 192 for **sw1** and 179 for **sw2**, with a yield of 28% and 26%



respectively. This low yield shows the extent of the damage to the electrical connections on the wafers.

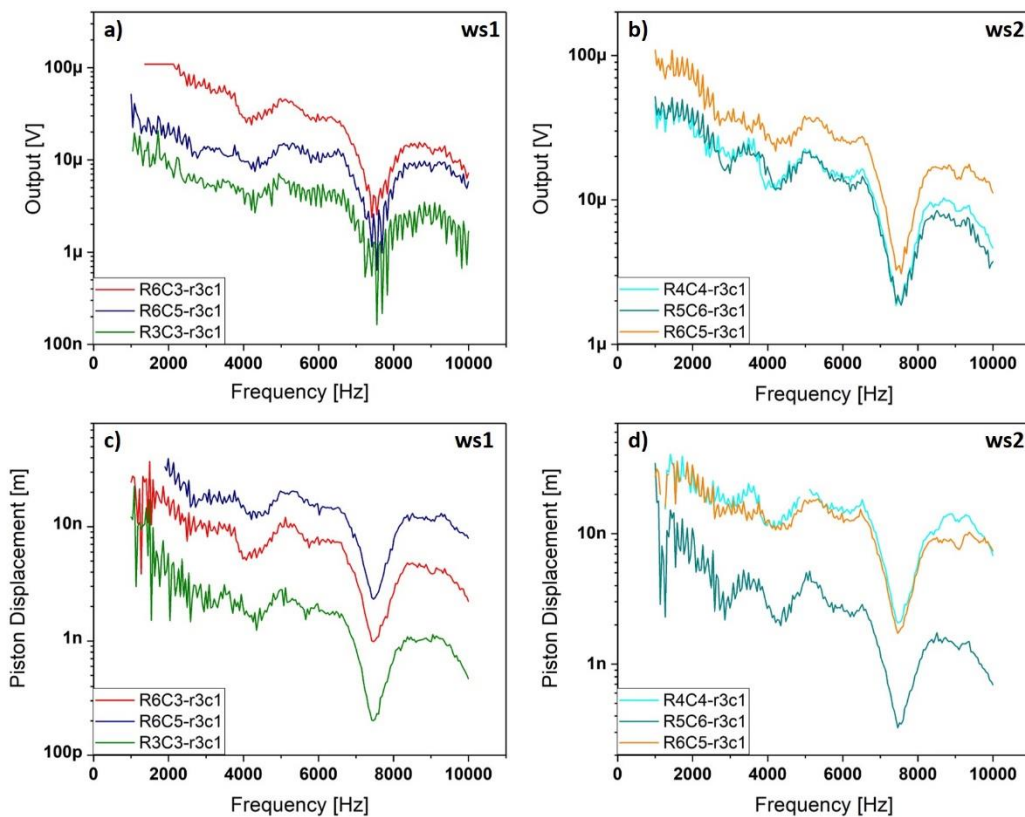
After this first sorting round, a second automatic test was performed on the remaining sorted devices to assess their mechanical response. Given the large number of remaining devices, it was not possible to check all pistons under the microscope in order to make sure the piston levers were still intact. The response of the devices was instead tested by actuating them acoustically and measuring their electrical output. In this case, not only would a measured output prove a device has a sound mechanical structure, but also prove the previously found results concerning the electrical connectivity. During the test, the movable electrode is polarized by a constant DC voltage, and a loudspeaker is used for the acoustic actuation with a signal frequency swept in the audible range. The outputs of the electrodes are connected to high impedance differential inputs of a lock-in amplifier, which demodulates the electrical signal at the actuation frequency. Due to space limitations in the setup, the loudspeaker could not be placed directly in front of the tested device. Instead, the acoustic signal was guided towards to the microphone through a plastic tube (Figure 4.4).



**Figure 4.4:** Test setup used for the electric and acoustic automatic wafer level tests performed on the microphones. (1) Semi-automatic probe station - (2) Polytec MSA 400 Laser Doppler Vibrometer – (3) LCR meter – (4) SR830 Stanford Research Systems Lock-in Amplifier.

**Figure 4.5** shows the output signals measured for three microphones of the same design on each wafer stack. As we will later show, the observed uneven response is only due to the uneven transfer function of the loudspeaker setup. Nevertheless, as it can be seen on the two top graphs, the outputs of all devices follow the acoustical

actuation, having the same electrical response with only a variation in amplitude. This proves that these devices have good electrical connections, and gives a first indication that the measured signal is due to the acoustically actuated pistons. However, in order to examine and demonstrate the correlation between the electrical output and the movement of the mechanical structure, the displacement of each microphone's piston was also measured under the same acoustic actuation. This was performed by using a Laser Doppler Vibrometer, which measured the out-of-plane displacement of the pistons while the loudspeaker was frequency swept. By comparing the measured piston displacement of each device (**Figure 4.5** bottom graphs) to its electrical output, correct microphone operation is evident: the electrical output of each device follows exactly the piston displacement as a function of the frequency of the acoustic actuation. This gives a clear first proof of concept for this new microphone design as it shows that the movement resulting from the acoustic signal was effectively transferred from air to the vacuum cavity.



**Figure 4.5: Variations of the electrical outputs (top) and piston displacements (bottom) as functions of acoustic actuation frequency, measured on ws1 and ws2. The uppercase letters R and C indicate the position of the layout field, and lowercase r and c specify the placement of the device within the field. All microphones share the same design, based on the D3 structure.**

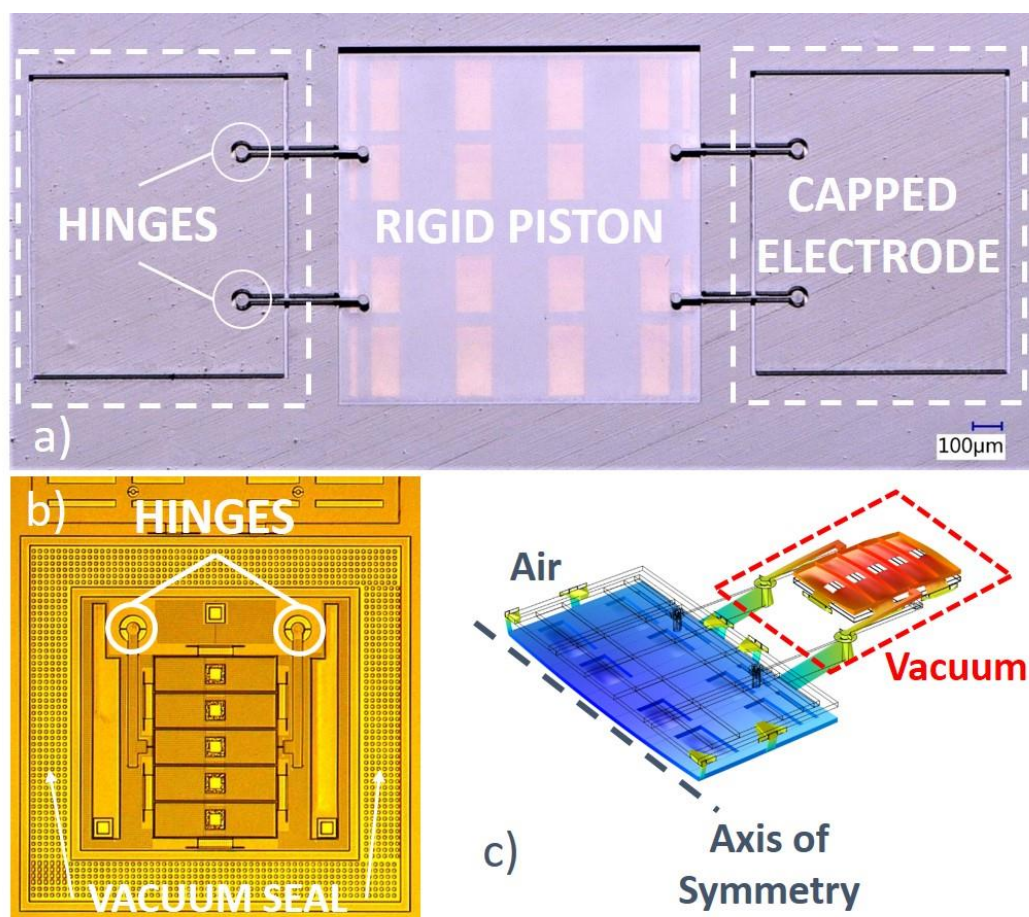
Similar results were obtained for 24 microphones on **ws1** and 21 microphones on **ws2**, decreasing the yield of the fabrication process to approximately 3% for both wafers. This can be explained by the missing piston levers on a large number of devices, in addition to the defective electrical connections. Furthermore, all working devices except for one were based on the **D3** structure design, and they are placed either along the third row or the first column of the fourth row in the field

layout (**Figure 4.3**). This is coherent with the first observations performed on the two wafer stacks, since the contacts in these locations incurred the least damage.

On a final note, differences can be noticed when the mechanical and electrical responses of the microphones are mutually compared. Considering **ws1** for example, although device R6C3 has a higher electrical output than R6C5, it has a lower piston displacement. The same is observed on **ws2** for devices R4C4 and R6C5. Since all these devices share the same design, this indicates that they exhibit either differences of stiffness or electrical connectivity issues, leading to the apparent difference in sensitivity. Given the small number of devices found to be working, the response of each microphone was further tested and studied separately, to better elucidate any underlying problems.

### Single device tests

Nearly all the microphones that were found to be working after the two sorting rounds of automatic tests are designed based on the **D3** structure. **Figure 4.6** shows a fabricated sample of one of these designs, which is **device 3** previously presented in **Chapter 3**, in which the rigid piston can be seen at the center. Four

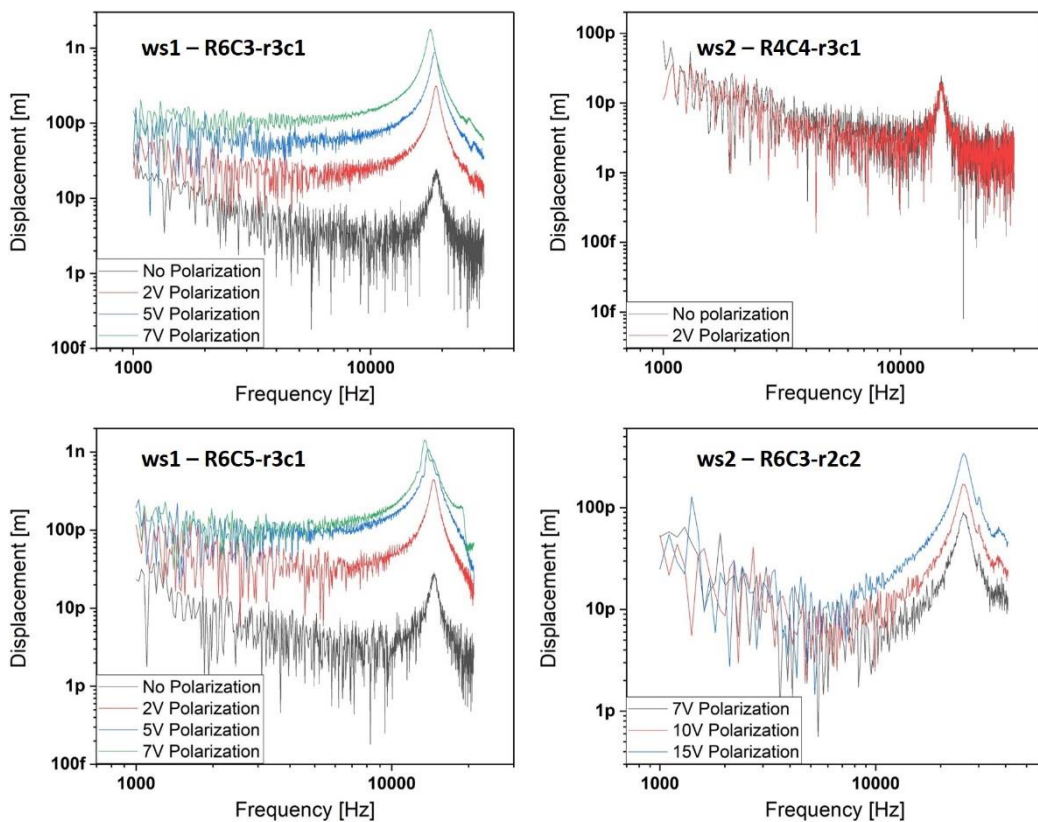


**Figure 4.6:** Optical microscopy images of the airside (a) and of an uncapped electrode (b). FEM simulation result showing the expected displacement of the moving parts of the mechanical structure (c). The scale of the deformation has been increased and only half of the symmetric structure is represented for higher clarity.



airtight hinges, mechanically connected to the piston, transmit its movement to two lateral electrodes enclosed in separate vacuum cavities. As explained earlier, similarly to the **D1** structure design, both electrodes move in the opposite direction of the piston and out-of-plane between top and bottom counter-electrodes.

To analyze further the mechanical response of the microphones, it is important to measure their resonance frequency, which gives an idea of the structures' total stiffness and mass. To bring about the resonance of the microphones, the movable electrodes of each device are polarized by a DC voltage and actuated by an AC signal applied to the counter-electrodes. The signals applied to the counter-electrodes are phase shifted by  $180^\circ$  for symmetric actuation. At the same time, the Laser Doppler Vibrometer is used to measure the displacement of the piston as a function of the AC actuation frequency. **Figure 4.7** shows the results obtained on selected devices on the two wafer stacks.

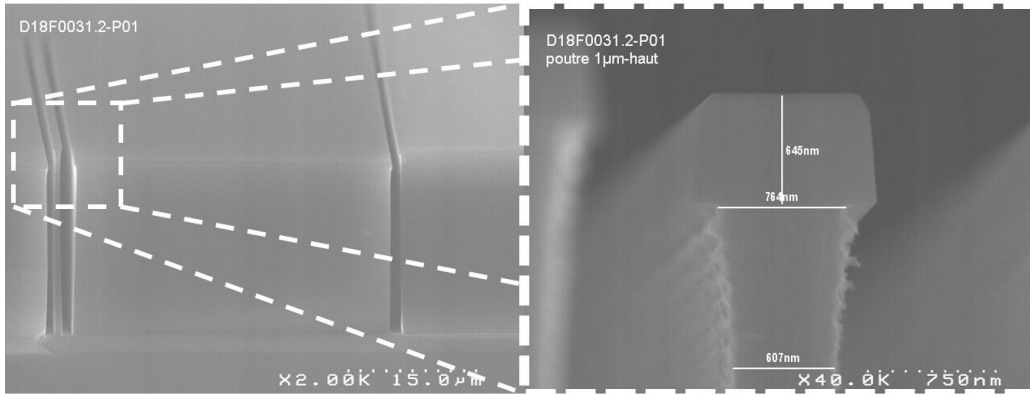


**Figure 4.7: Measured resonance frequencies of devices on ws1 and ws2 at different DC polarization voltages.**

On **ws1**, the two devices belong to the design presented earlier in **Figure 4.6**, for which the theoretical resonance frequency is expected at around  $33\text{ kHz}$ . However, the measured resonance frequencies were much lower, at  $19\text{ kHz}$  and  $14.6\text{ kHz}$  for R6C3 and R6C5 respectively. First, this explains the higher piston movement under acoustic actuation noted previously for R6C5: since its resonance frequency is lower, and both devices have the same design, the difference must be due to a lower stiffness, which explains the higher mechanical movement. Yet, this does not explain the lower electrical signal of R6C5, which should be proportional to its

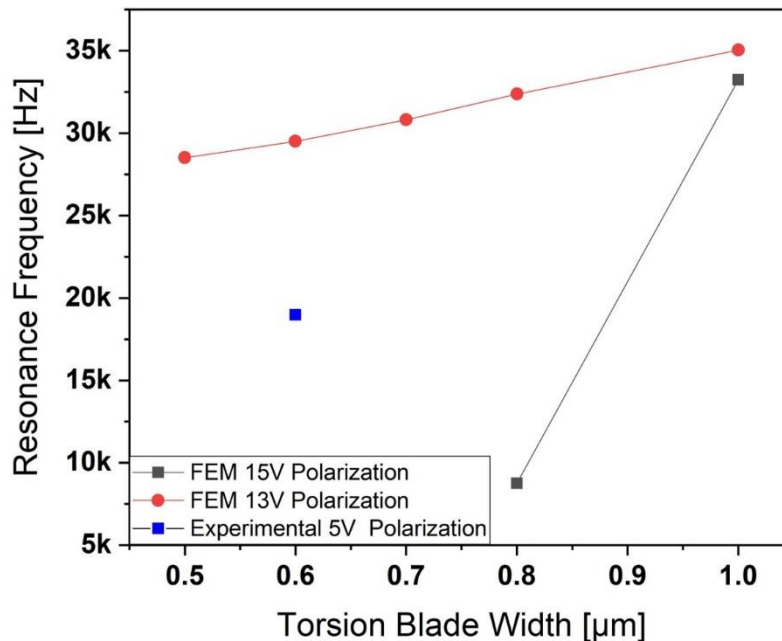
higher piston displacement. Therefore, this indicates faulty electrode connections for R6C5. Furthermore, the same reduced stiffness is observed for the same design at R4C4 on **ws2**, with a resonance frequency of 14.9 kHz. Two explanations can be given to these reduced resonance frequencies:

- Lower stiffness of the **OPSs** due to overetching effects. A Focused Ion Beam cut section of a test wafer showed that the width of the torsion blades was at 600 nm instead of 1 μm (**Figure 4.8**).
- Disconnected or damaged **OPSs** around the pistons and/or the electrodes.



**Figure 4.8:** Scanning electron microscopy images of a test wafer section cut with a Focused Ion Beam. The section shows the overetching of the torsion blades to a width of 600 nm instead of 1 μm.

The overetching of the torsion blades does reduce the stiffness and decrease the resonance frequency as it can be seen in the **FEM** simulation results shown in **Figure 4.9**. For a 15 V DC polarization, the width of torsion blades has a strong effect on the resonance frequency and on the stability of the device: for widths lower

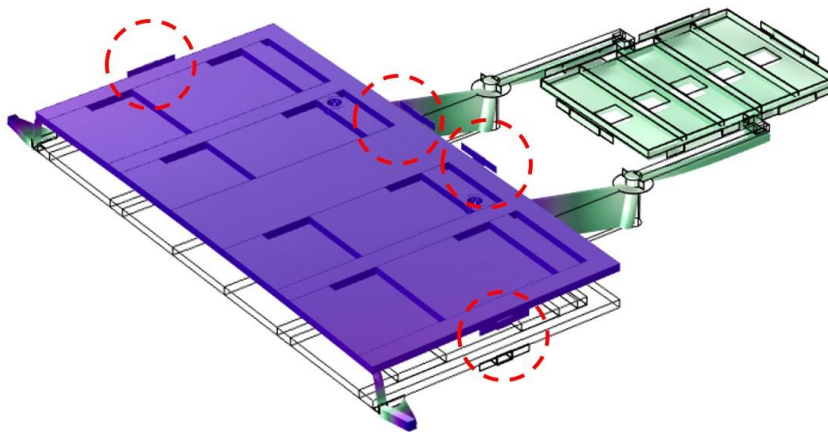


**Figure 4.9:** Variation of the resonance frequency of device 3 design as a function of the torsion blades' width FEM simulation results at different polarization voltages.

than  $800\text{ nm}$ , the structure becomes unstable due to the spring softening effects that become dominant. At  $13\text{ V}$ , the resonance frequency decreases with the lower blade width, yet remains stable. This would indicate that, theoretically, the resonance frequency should be much higher at  $5\text{ V}$  of polarization, regardless of the overetching. However, the highest measured resonance frequency was much lower, and did not strongly vary with the DC polarization as evidenced by **Figure 4.7**.

Moreover, although the resonance frequency remains globally unchanged, the amplitude of displacement increases with the higher polarization amplitude. These results therefore point towards the hypothesis that the lower stiffness is mainly due to damaged or disconnected **OPSs**, which lower the stiffness around the piston. This reduced stiffness leads to a higher piston displacement, and, normally, to a higher electrode displacement as well. However, due to the low polarization amplitude, the remaining stiffness applied to the electrode is much higher than initially designed to be, strongly opposing the electrode's movement and leading to the bending of the levers connecting it to the **AVATRAMs**. This can be observed on the simulation result displayed on **Figure 4.10**: on the first measurable eigenmode, with disconnected **OPSs** around the piston, the electrode's connection beams and torsion blades sustain a highest deformation. Thus, for this reason, an increase in polarization would increase the spring softening effect on the electrodes, decreasing the deformation of the beams and giving the piston the observed greater range of motion at resonance.

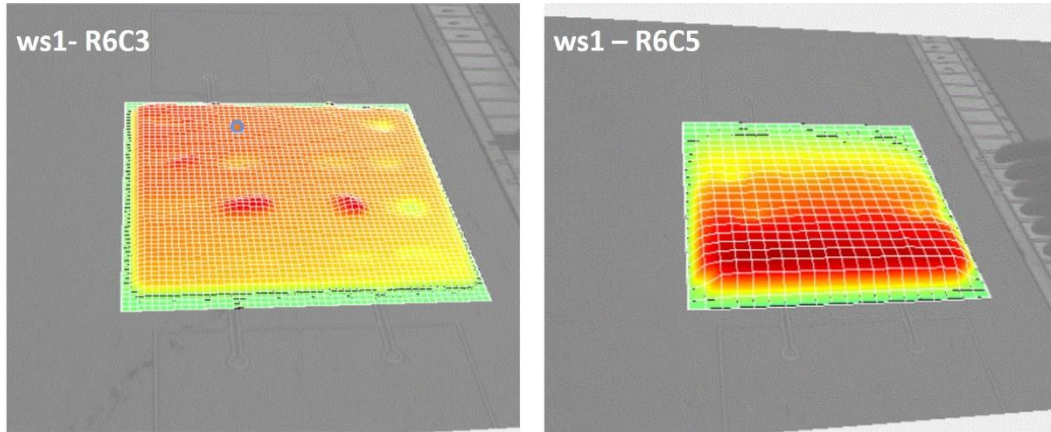
Eigenfrequency=19831 Hz



**Figure 4.10: Eigenfrequency simulation result of the D3 design with disconnected OPSs around the piston (indicated by dashed red circles).**

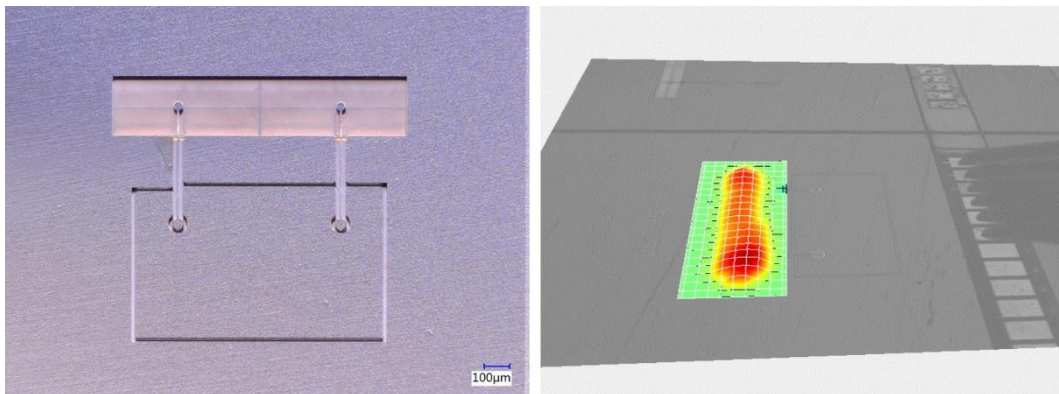
Additional experimental evidence further supports this hypothesis. At the resonance of each device, the Laser Doppler Vibrometer was used to scan the entire piston and map its displacement and deformation. As displayed in **Figure 4.11**, device R6C5 on **ws1** has a highly dissymmetric deformation, with one side of the piston having a much higher displacement than the other does. Since the piston has

all four of its levers and connections to the **AVATRAMs**, this can only be explained by damaged or disconnected **OPSs**. This most likely occurred during the removal of the adhesive tape covering the pistons. Despite the fact that it has a much more symmetric displacement, device R6C3 does exhibit a slight dissymmetry, which is also indicative of damaged **OPSs**.



**Figure 4.11: Laser Doppler Vibrometer scans of the piston deformation at resonance for devices ws1 - R6C3 and R6C5.**

Concerning the **ws2** wafer, as it can be seen on **Figure 4.7**, the resonance of device R4C4 is unaffected by the polarization amplitude. This can only be explained by a defective electrical connection to the movable electrode. This is the case for nearly all devices that were previously thought to be working on **ws2**, which shows the limitations of the acoustic automatic test. These devices exhibited a measurable output under acoustic actuation, one that was very similar to their pistons' movements. However, the results of the resonance frequency test clearly prove that the movable electrode is electrically disconnected. It can therefore be concluded that the measured signal during the automatic test was only due to trapped charges along the electrode. An exception to these devices on **ws2** is a device on field R6C3 (**Figure 4.7**), based on the **D1** structure design. This device had a measurable output during the acoustic automatic test, and, at 15 V of DC polarization, its expected resonance frequency is at 27.3 kHz while its measured resonance is found at 25.7 kHz. Furthermore, the mapping of the piston's deformation at resonance proved that it was moving out-of-plane as intended in the design (**Figure 4.12**). No

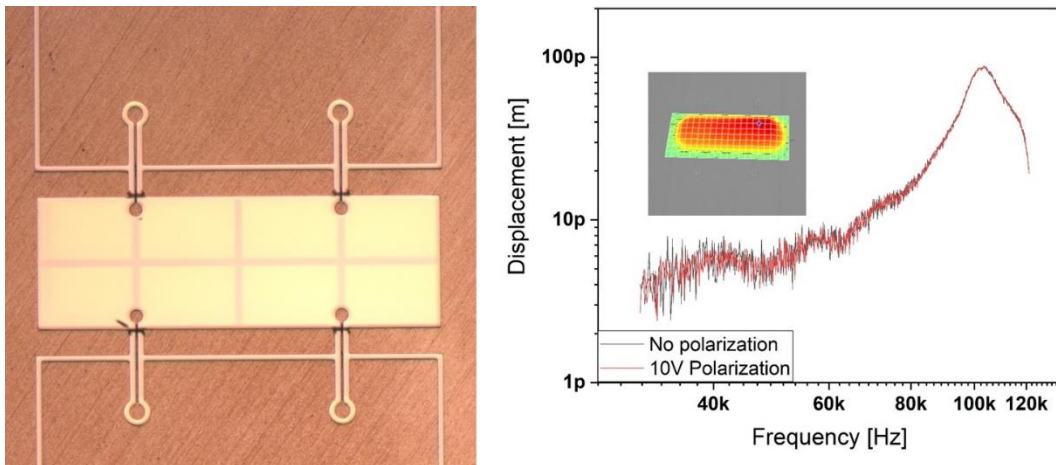


**Figure 4.12: Optical microscopy image of device R6C3-l2c2 based on the D1 structure design (left), and mapping of the piston's deformation during resonance (right).**



further tests could be performed on the device as it stopped responding after the scanning of the piston's displacement, despite the care that was taken during the measurements. This is probably due to the fragility of its contacts and its electrical wires, as this device is on the second row of the second column in the layout field, where the contacts were severely damaged. Nonetheless, these results do give a first validation of the **D1** structure design.

Another notable device measurement is the resonance of four aeroacoustic microphones on **ws1**, based on the design of **device 4** previously detailed in **Chapter 3**. The devices exhibited resonance frequencies in the range of  $92.7\text{ kHz}$  and  $104.7\text{ kHz}$ , which is close to their expected resonance at  $105\text{ kHz}$ . However, as shown by the example in **Figure 4.13**, they all had an electrical connection problem with the movable electrode, as no variation of resonance amplitude was measured for different DC polarizations. Nevertheless, these results also prove the validity of the **D3** structure for aeroacoustic designs with resonance frequencies beyond the audible range.



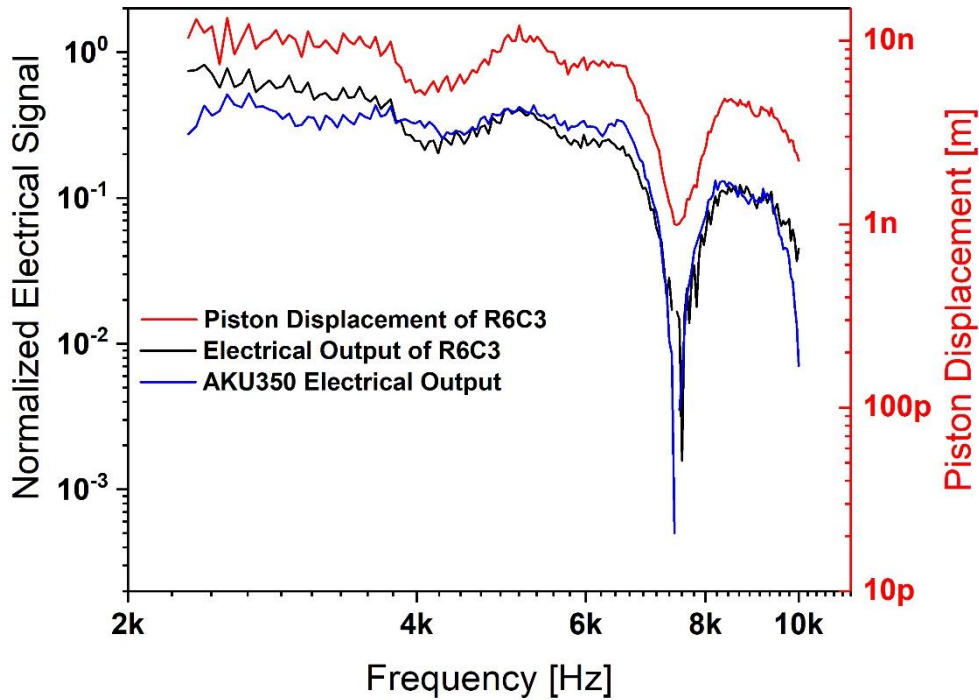
**Figure 4.13: Optical microscopy image of an aeroacoustic microphone based on the design of device 4, and its resonance frequency at different DC polarizations. The mapped deformation of the piston at resonance is shown in the inset.**

At the end of the resonance frequency test, only five devices, all on the **ws1** wafer, could be considered as having a good overall microphone response. These microphones all belong to the **device 3** design, having resonance frequencies between  $14.6\text{ kHz}$  and  $22\text{ kHz}$ , with a resonance peak amplitude that varied with the DC polarization of the movable electrode. The remaining 19 microphones on **ws1** and all microphones on **ws2** were rejected due to the electrically disconnected movable electrode evidenced by the unvarying amplitude at resonance at different DC polarizations. In addition to the detached piston connections and released electrical contact pads, a third reason for this very low yield will be elucidated with the discussion of the second fabrication batch results later in this chapter.

Out of the remaining five microphones, the previously discussed device on R6C3 exhibited the highest electrical output under acoustic actuation, and the highest resonance frequency at  $19\text{ kHz}$  for a symmetric out-of-plane piston displacement. For these reasons, it was chosen for more detailed acoustic measurements. These



measurements were also conducted at wafer level, as all microphones are prepackaged with an integrated **BV**. Thus, the acoustic characterization of the test bench was necessary due to the uneven transfer function of the loudspeaker setup. At wafer level, it is impossible to use a standard measurement microphone for reference, as its larger size would require a change in the measurement setup. An Akustika AKU350 [81] commercial **MEMS** microphone was therefore used instead: the microphone was glued on a thin plastic board, and placed in the probe station, the same way as was done with the tested wafer. Even though it does not offer the same level of precision as a standard measurement microphone, the **MEMS** microphone permits the characterization of the setup with the closest possible acoustic configuration to the one during the tests. **Figure 4.14** shows the measured acoustic response of the commercial microphone, proving the uneven transfer function of the loudspeaker. This measurement is also in very close agreement to the previously discussed electrical output and piston displacement of the R6C3 device. This characterization step was performed before each measurement.



**Figure 4.14: Electrical output and piston displacement of the R6C3 device on ws1 and electrical output of the reference commercial MEMS microphone under acoustic excitation. The outputs are normalized as the AKU350 has an internal amplifying electronic circuit.**

In order to better study the acoustic response of the microphone under acoustic excitation, the output of each counter electrode was measured separately using the current input of the lock-in amplifier, while the other counter-electrode was connected to the ground. The current input is internally connected to a transimpedance amplifier with a gain defined by the feedback resistance  $R_{Gain}$ :

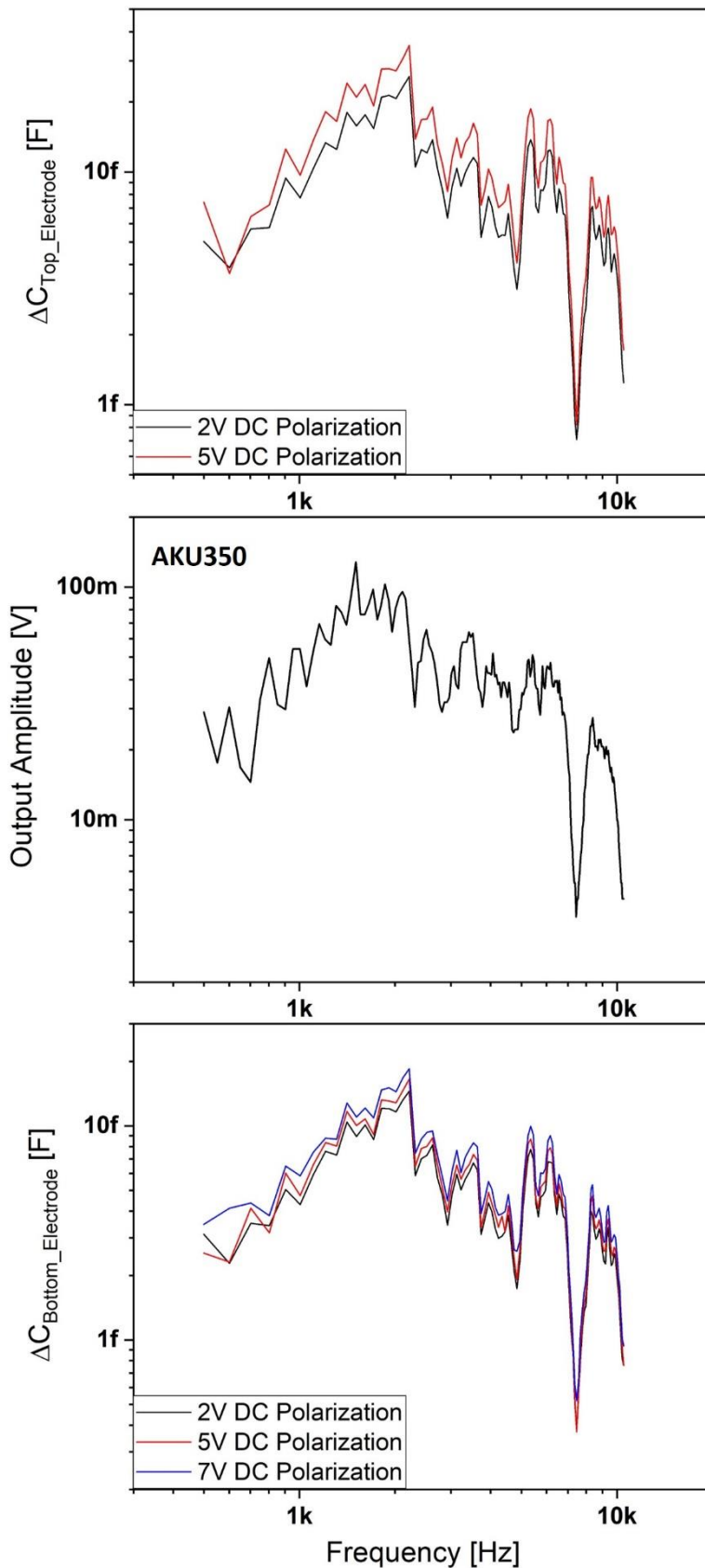
$$U_{meas} = R_{Gain} I_{meas} = R_{Gain} j\omega Q_{meas} , \quad (4.1)$$

where the harmonic approximation is used and  $U_{meas}$ ,  $I_{meas}$  and  $Q_{meas}$  are the measured voltage, current and charges. Recalling that  $Q_{meas} = dC_{meas}U_{pol}$ , this allows retrieving the variation of capacitance by:

$$dC_{meas} = \frac{U_{meas}}{R_{Gain}j\omega U_{pol}}. \quad (4.2)$$

**Figure 4.15** shows the measured variation of capacitance at different polarization amplitudes from the top and bottom electrodes of device R6C3, as well as the measured response of the reference **MEMS** microphone. The difference between the signals of the two counter electrodes is directly apparent as the measured signal of the top electrode is nearly double that of the bottom electrode. For example, at 5.2 kHz and a polarization of 5 V, the total variation of capacitance of the top counter electrode is equal to 17 fF, while the variation of capacitance of the bottom counter electrode is measured at 8.3 fF. Furthermore, the highest applicable polarization during the measurement of the top counter electrode is 5 V, as higher values led to the pull-in. This was indicated by a peak in current and the saturation of the current input of the lock-in. Conversely, the highest polarization applied during the measurement of the bottom counter electrode was purposely limited to 7 V so as not to damage the device. These results indicate that only one half of the bottom counter electrode is connected for this device. In fact, as in this design the piston is connected to two movable electrodes, each movable electrode is sandwiched between two counter electrodes. The top and bottom counter electrodes are therefore each separated into two electrically connected halves, one on each side of the piston. This explains why the measured signal of the top counter electrode is nearly double that of the bottom one: considering the movable electrode for which the bottom counter electrode is disconnected, the applied electrostatic forces are no longer balanced, which explains the low pull-in voltage during the measurement of the top counter electrode. Thus, despite the applied 7 V, the pull-in also takes place at 5 V during the measurement of the bottom counter electrode. Yet, it does not lead to the saturation of lock-in's current input due to the disconnection of half of the counter electrode.

The sound pressure applied on the microphone can be calculated from the output of the reference microphone that has a sensitivity of  $-38 \pm 1$  dBV. At 5.2 kHz, the output is equal to 53 mV, meaning that the pressure is equal to  $4.2 \pm 0.5$  Pa. The sensitivity of the tested device can then be calculated from the addition of the previously given values of variation of capacitance for each counter electrode, giving a value of  $6 \pm 0.7$  fF/Pa. This value is higher than the theoretical value of the sensitivity of 4 fF/Pa, which was expected given the lower resonance frequency and stiffness. **Table 4.1** summarizes the performance measurements of device R6C3. We also note the low quality factor measured at resonance. The quality factors of all measured devices are much lower than expected, between 5 and 15, which indicates the presence of a higher dissipation. As it shall be discussed in the next section of this chapter, this dissipation is due to issues with the hermeticity of the cavities.



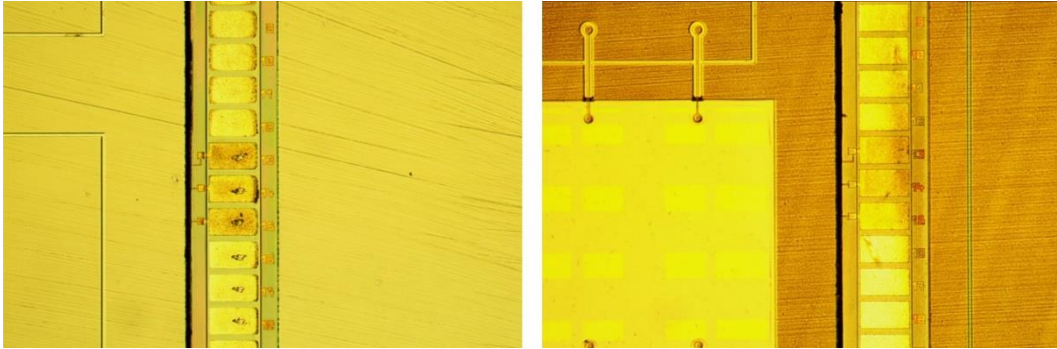
**Figure 4.15: Measured variation of capacitance at the top and bottom electrodes of device D6C3 under acoustic actuation and at different polarization amplitudes. The measured output of the reference microphone is represented in the middle graph.**

	$Sense_{\Delta C} [F/Pa]$	$F_0 [kHz]$	$Q$
<i>Theoretical value</i>	$4 \cdot 10^{-15}$	33	$> 100$
<i>Experimental value</i>	$(6 \pm 0.7) \cdot 10^{-15}$	19	7

**Table 4.1:** Theoretical and experimental values of the performance parameters of device R6C3 on ws1.

## 4.2. Second fabrication batch

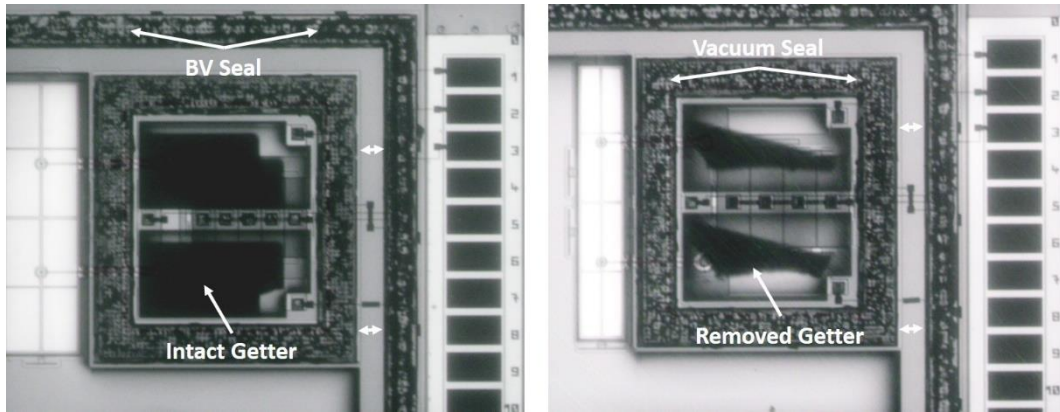
For the second fabrication batch, the problem of the released contact pads was corrected by removing the identifiers of the mask used for the second **DRIE** step. The two obtained wafer stacks, **ws3** and **ws4**, displayed no damage to their contact pads (**Figure 4.16**), proving that the source of the problem was in fact the mask identifiers. A less adhesive tape was also used during the sawing of the wafers to reveal the contact pads, which left most of the piston connections to the **AVATRAMs** intact. This was optically visible on the entire wafer stacks.



**Figure 4.16:** Optical microscopy images of the contact pads on **ws3**. The same results were observed on **ws4**.

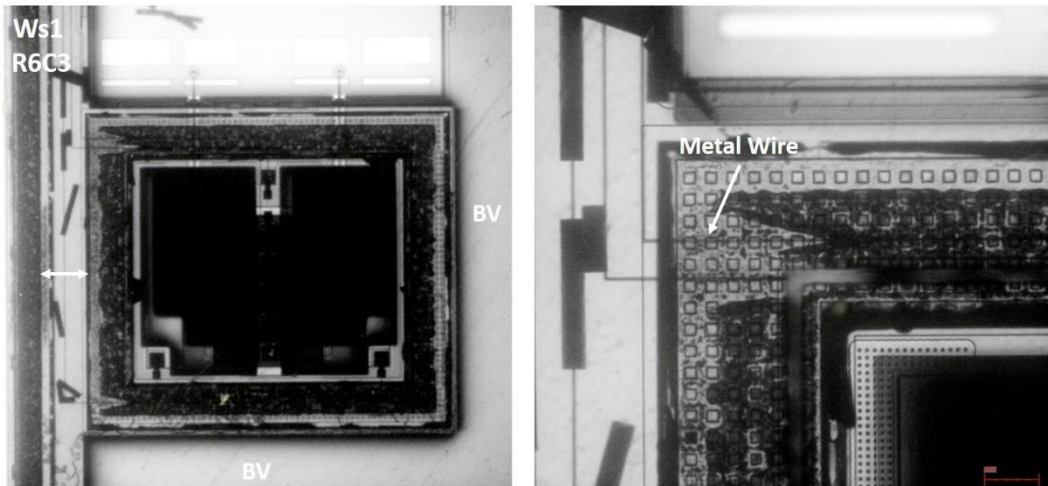
However, as promising as these fabrication results were, the experimental results did not meet the expectations. After following the same testing protocol of automated capacitance and acoustic measurements, the yields of both wafers were similar to those previously obtained for **ws1** and **ws2**. Taking into consideration the fact that the mechanical workings of the designs were validated on the wafer stacks of the first fabrication batch, this indicated the presence of underlying fabrication problems.

In search of these problems, the wafers were studied under an infrared microscope, which allows the observation of structures hidden inside the cavities since silicon is transparent at infrared wavelengths. A problem with the getter layer inside the cavities was directly noticeable. This layer is an alloy of different metals, and is therefore opaque under infrared light. However, as it can be seen in **Figure 4.17**, on a large number of devices on both wafers, this layer was either partially or almost completely removed from the bottom of the cavity. Given that the getter is deposited directly on silicon, it could not have been removed due to the release of a  $\text{SiO}_2$  layer. This indicates that this layer has been chemically attacked during the fabrication process.



**Figure 4.17:** Infrared microscopy images of the cavities of devices on ws3 and ws4. The getter layer has been partially or almost completely removed on a large number of devices.

Upon closer inspection of the vacuum seal surrounding the cavities, cone shapes were noticed along the narrow metal wires used to connect the electrodes to the external contact pads. Although, at the time, they were thought to be due to the HF infiltration problem releasing the contacts of the first fabrication batch wafers, the same results were also observed on the devices of **ws1** and **ws2**. For example, on the working R6C3 device on **ws1**, the perimeter of the vacuum seal is transparent, which means that the eutectic mixture of metals formed during the bonding process has been partially removed (**Figure 4.18**). This shows that the problem is due to the second release step: once the pistons are released, the HF vapor infiltrates the **BV** through the surrounding narrow slits and the SiO<sub>2</sub> layer that supports the eutectic mixture on the cap wafer's side is then partially etched, which releases the mixture. This also explains the cone shapes, since a SiO<sub>2</sub> layer also covers the metal wires. In fact, the narrow wires are elements protruding out of the surface of the wafer and do not form a uniform layer.



**Figure 4.18:** Infrared microscopy images of a cavity for the working R6C3 device on ws1. On the right is a zoomed in image of the top left of the vacuum seal showing the release cone motifs.

Consequently, during its deposition, the oxide needs to fill the corners and nooks created by the wires. However, the strong 90° angle of the protruding elements creates an area in which the SiO<sub>2</sub> layer is more susceptible to defects. The resulting

weaker structure of the SiO<sub>2</sub> directly surrounding the wires renders it more easily etched. Therefore, the wires become guides for the HF vapor, which rapidly etches the oxide around the wires, creating the noticeable cone motifs, and possibly reaching the vacuum cavity.

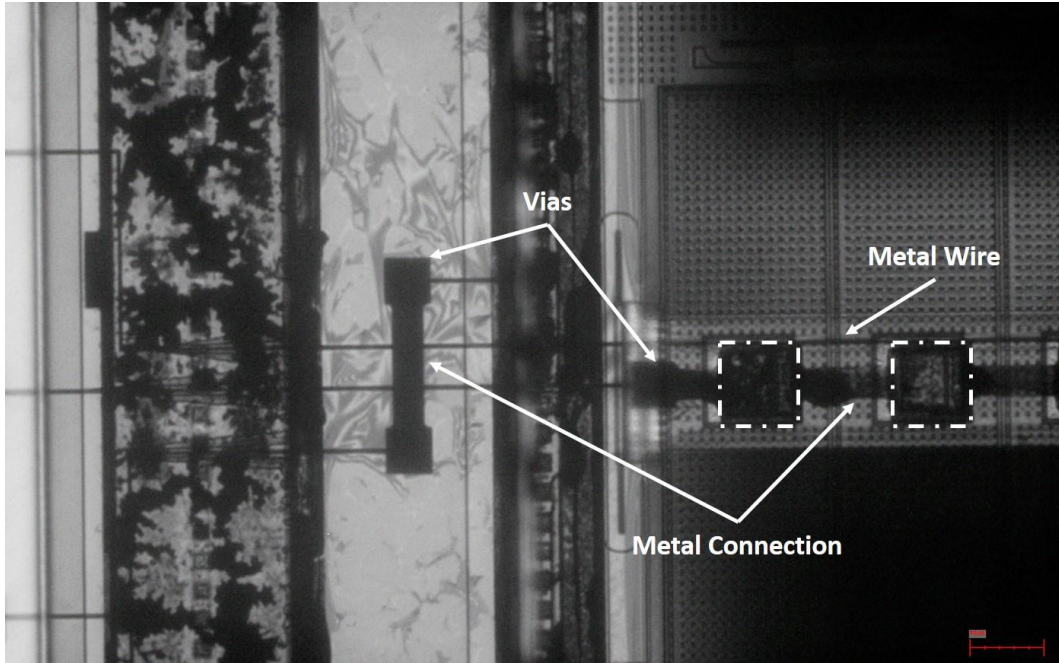
The hypothesis of the HF vapor reaching the cavity is also supported by the observations concerning the partial or complete removal of the getter layer on some devices. For even when the release step is finished, the HF vapor can remain trapped, leading to its condensation inside of the cavities. Although in its gaseous state HF does not react with the getter layer, it does become very corrosive in its liquid form. This would explain the partial or complete removal of the getter. The solution to this problem is therefore to cover the metal wires and avoid exposing them to HF vapor during the second release step. This can be simply done by enlarging the vacuum seals and connecting them to the seal that cordons off the **BV**. Double-headed arrows on **Figure 4.17** and **Figure 4.18** indicate the required distance of enlargement. In this case, the wires would be completely covered by the seals and can pass directly from the microphones' vacuum cavities to the contact pads. By doing so, the wires are not exposed to the **BV** cavity, thereby avoiding the HF vapor of the second release step.

Furthermore, the infrared observations performed on all wafers also revealed a problem with the electrical ohmic contact points of the electrodes. These contact points are formed during the eutectic bonding of the wafers between the Germanium deposited on the **MEMS** part of an electrode and the Aluminum-Silicon (AlSi) alloy of the second conductive layer on the cap wafer. The electrical signals are routed to and from the electrodes through these ohmic contacts. The problem is observable on **Figure 4.19** where the top counter-electrode can be seen sectioned in parts, each part having its own contact point delimited by a dashed rectangle. Belonging to the same electrode, these ohmic contacts are interconnected through a metal connection made from the second conductive layer of the cap wafer. The last contact is connected to a grid of vias to transfer the signal to a narrow metal wire used to connect the electrode to the contact pad outside of the cavity. However, instead of ensuring the electrical connection, the AlSi of the metal connection was consumed during the formation of the eutectic mixture of the contact points. This can be proved by comparing the metal connection between two contacts, and the one between two grids of vias. The former is translucent, after having been consumed by the formation of the eutectic, while the latter is stark black and opaque. What is more, the contact points also appear to be translucent, indicating the lack of metal necessary for a good electrical connection.

This further explains the experimental results and the low yield obtained on all the wafers: the metal connection between the ohmic contacts and the vias was consumed, disconnecting the electrodes and rendering the devices dysfunctional. What is more, the unforeseen consumption of the metal connection is a random process, which explains why some electrical contacts are functional while others are defective. This problem remained previously unnoticed on **ws1** and **ws2** as the low yields were thought to be only due to the other more directly visible fabrication



issues. However, we note that it can be rectified by avoiding the use of the second conductive layer for the interconnection of the ohmic contacts and the connection of the ohmic contacts with the grids of vias. This can be done by surrounding the contacts with vias, and interconnecting them directly with the metal wires of the first conductive layer.



**Figure 4.19: Infrared microscopy image showing the top counter-electrode of a device and its ohmic contact points (dashed rectangles). The contacts are interconnected by a metal connection made from the second conductive layer of the cap wafer. Grids of vias form the link between the contacts and the narrow metal wires, which are made from the cap wafer's first conductive layer and which connect the electrodes to the external contact pads.**

Finally, concerning the low quality factors measured at the resonance of the microphones, the findings of the infrared observation only offer a partial explanation. The infiltration of the HF vapor into the cavities compromises their hermeticity, as it creates opening in the SiO<sub>2</sub>. This, in addition to the detached getter layer, removes any possibility of vacuum within the cavities. We do however add that problems with vacuum and cavity hermeticity were also signaled on other wafers and devices fabricated recently using the same process. These issues might be linked to variabilities in the machinery used during the process, and they are currently under investigation.

In conclusion, even though the M&NEMS process was adapted for this design, all previously discussed mechanical elements, from the AVATRMs to the pistons and the electrodes, were successfully fabricated, and the workings of the mechanical structures were validated. Thus, despite all the encountered problems, the first fabrication batches were successful in giving a first proof of concept of the new microphone design, with a correct acoustic and mechanical response. The remaining problems highlighted after the second fabrication batch have all been corrected, and the fabrication of the new devices is currently underway. The correction of contact problems and issues with the second release step should lead



to a much higher fabrication yield, and a much better overall microphone performance.

# Chapter 5 Concluding remarks

This work presents and validates a new **MEMS** microphone design with the aim of improving overall device performances while maintaining a small device size. Previous endeavors in this respect have failed to reach the sought performance levels. Depending on the chosen transduction mechanism, this was either due to restrictions imposed by the design (capacitive transduction) or due to fundamental noise limitations (piezoelectric transduction). In this new approach, the design of capacitive microphones is entirely changed so that the previously limiting noise sources stemming from viscous damping losses in air are drastically reduced. Instead of the simple condenser design, the new device is separated into a rigid piston harvesting the acoustic pressure in air, connected mechanically to a capacitive transducer encapsulated in a vacuum cavity. An innovative mechanical hinge that transfers the movement of the piston from air to the vacuum cavity ensures the connection between both parts. Theoretically, this separation should significantly improve the performance of the microphone ( $\text{SNR} \geq 75 \text{ dB}(A)$ ) without necessarily increasing its size.

As it is the central element of this new design concept, the air-to-vacuum hinge was first designed to meet the working requirements for the microphone. This hinge was therefore mechanically designed to be robust enough to withstand to the constantly applied atmospheric pressure and to 10 bars of possible pressure overshoot, while remaining flexible enough to fully transfer the mechanical motion. Around this central component, a lumped elements model was then developed, modeling the expected acoustic and mechanical properties of the microphone. These properties are largely dependent on the geometry of the microphone, which is itself determined by what is achievable through the fabrication process. The M&NEMS process, developed to maturity by CEA-Leti, was chosen and adapted for the implementation of this new design because, most importantly, it allows the juxtaposition of encapsulated and exposed elements, crucial for this new concept. Finally, based on this process and on the developed model, multiple microphone structures were designed to meet a wide range of performance levels, thereby exploring the potential of this new concept.

Given that the chosen process was adapted to this new microphone design, several problems were encountered during the fabrication of the first devices. For the first batch of wafers, problems concerning the breaking of the piston connections and the release of the contact pads were noticed, and the wafers exhibited a very low yield of working devices. These problems were adequately solved by taking the

necessary precautions during the fabrication of the second batch of wafers, yet the yield of these wafers still did not increase. This indicated the presence of other underlying problems, the first one being defective electrical connections due to the consumption of the metal necessary for a good ohmic contact during the eutectic bonding step. The second problem was the infiltration of HF vapor into the vacuum cavities along the metal wires used to route the electrical signals to and from the devices. Aside from their subsequent exposure to the external environment, the cavities also trap the HF vapor, which then condensates and attacks the getter layer. For the third batch, the necessary steps have been taken to correct the faulty electrical connections and to avoid any HF infiltration into the cavities. The fabrication of these third iteration wafers is currently underway.

Nevertheless, despite all of the encountered problems, multiple microphones were found to be working. Through electrical, mechanical and acoustical wafer level characterization steps, the devices were sorted, and the working devices were selected. The in-depth study of the working devices proved correct microphone operation, giving a clear first proof of concept of the air-to-vacuum transmission hinge and of the new microphone design. The tests also proved the viability of more exploratory devices, such as the aeroacoustic microphone design, exhibiting a resonance frequency well beyond the audible range.

In conclusion, the present work sets the foundations upon which all future developments of this new microphone concept can be constructed. Following the corrections that were made, the awaited microphones of the third fabrication batch should further validate this new design, and allow for more in-depth testing of all performance levels. As is the case of any new sensor, the current design can also be further improved upon and refined. Concerning the fabrication process, other than the previously discussed process adaptation steps, the replacement of the contact pads by through silicon vias in the bulk-Si of the device wafer can be envisioned. This would remove the need for the risky sawing step to reveal the contact pads, and avoid the required metal wires connecting the electrodes in the cavities to the external pads. As for the design, it can be possibly improved by studying other dissipation phenomena, such as thermo-acoustic and thermo-elastic dissipation at the sensor level, which may become important sources of additional noise if ultra-high performance levels are sought after. Nonetheless, with this first proof of concept, this new design paves the way for future ultra-high performance **MEMS** microphones.

# Appendices

## *Appendix A. Main microphone specifications*

In the following, the main specifications used to determine the performance level of **MEMS** microphones are briefly explained.

### **Sensitivity**

The sensitivity is generally defined as the electrical output of the **MEMS** microphone at a given acoustic pressure. It is measured at a 1 *kHz* sinusoidal input signal with a sound pressure of  $P = 1 \text{ Pa}$ . This standard reference measurement signal can also be expressed in terms of Sound Pressure Level (**SPL**) in decibels (**dB**):  $20 \log_{10}(P/P_0) = 94 \text{ dB}_{SPL}$ ; where  $P_0 = 20 \mu\text{Pa}$  is the threshold of hearing. For analog microphones, the sensitivity is usually expressed in *mV/Pa* or in *dBV/Pa* in reference to 1 *V*. As for digital microphones, it is expressed in *dBFS* in reference to the digital full scale.

### **Noise and Signal-to-Noise Ratio (SNR)**

The signal-to-noise ratio is the ratio of a given intended input signal to the amount of residual noise at the output of the microphone. It is a general indicator of the quality of a microphone's signal, as the lower the **SNR** is, the higher the noise level, which deteriorates the quality of the microphone's output. Similarly to the sensitivity, the **SNR** is usually measured using the standard reference measurement signal at 94 *dB<sub>SPL</sub>* and 1 *kHz*. The measurement is performed in an anechoic environment to avoid any sources of noise external to the microphone. Expressed in A-weighted decibels (**dB(A)**), the **SNR** is typically measured by A-weighting (standard IEC 61672:2003) and integrating the sensor noise over a 20 *kHz* bandwidth to take into account the variations of the human ear's sound sensitivity at different frequencies.

The noise of the microphone stems from both the **MEMS** sensor and the signal amplifying electronic circuit. It is measured as the signal generated at the output of the microphone in an anechoic environment and under no external acoustic excitation. However, the noise is commonly discussed in terms of Equivalent Input Noise (**EIN**), an imagined acoustic noise source at the input of the microphone. The **EIN** is expressed in *dB<sub>spl</sub>* and can be calculated from the microphone's **SNR**:

$$EIN = 94 \text{ dB} - SNR$$

## Total Harmonic Distortion (THD) and Acoustic Overload Point (AOP)

Sources of nonlinearity and consequent signal distortion are an inherent aspect of any real sensor. In the case of microphones, the distortion results in harmonics of the measured signal frequencies. The Total Harmonic Distortion (**THD**) is therefore the ratio of the power of signal harmonics to the power of the fundamental frequency when the microphone is excited by a sign wave. When the noise at the output of the microphone is also considered, the distortion can be expressed in **THD+N**:

$$THD + N = \frac{\sum Power(Harmonics) + Power(Noise)}{Power(Fundamental)}$$

The Acoustic Overload Point (**AOP**) is defined as the sound pressure level at which the THD exceeds 10% for very high sound pressure levels. It is therefore measured at high sound pressure levels with a 1 kHz sinusoidal signal. With the **EIN**, the **AOP** defines the Dynamic Range (**DR**) of the microphone:

$$DR (dB) = AOP - EIN$$

## Frequency Response and Bandwidth (BW)

The frequency response describes the variation of the microphone's sensitivity over the audible frequency spectrum. It represents the transfer function of the device, which acts as a high pass filter for low frequencies, and as a second order resonant system for higher frequencies. Moreover, the bandwidth (**BW**) of the microphone is the frequency range for which the microphone's response is flat, limited by the points at which it reaches a value 3 dB below the reference output

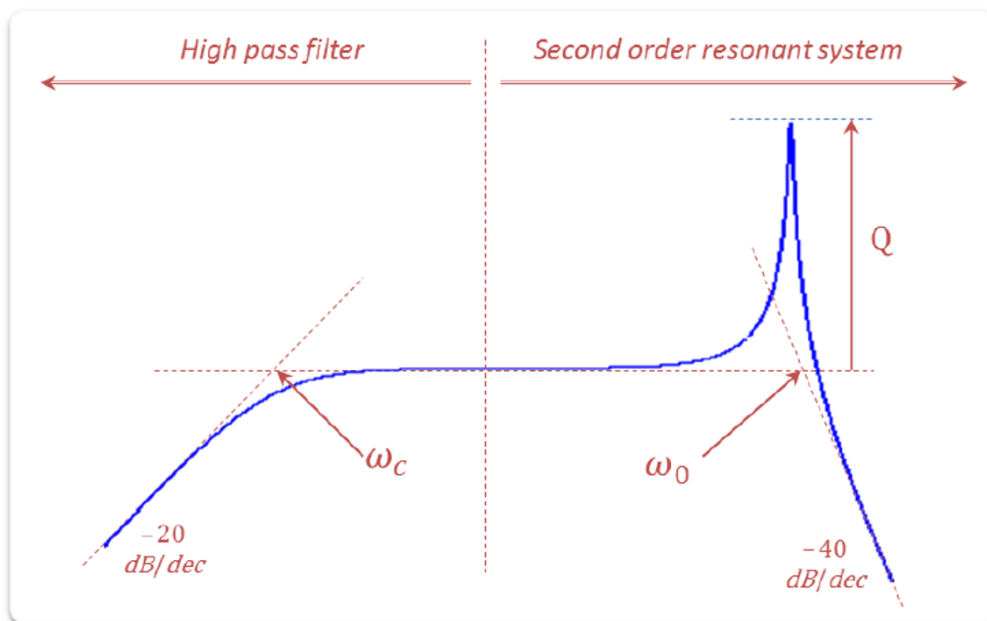


Figure A.1: Example of a microphone's frequency response showing the BW delimited by the cut-off frequency  $\omega_c$  and the resonance frequency  $\omega_0$  of the device.

level at 1 *kHz*. The lower limit is thus defined by the cut-off frequency  $\omega_c$ , below which the roll-off is first order at 20 *dB/decade*. The upper limit of the **BW** is defined by the resonance frequency  $\omega_0$ , beyond which the roll-off is second order at 40 *dB/decade*.

## *Appendix B. Acoustic impedance of small rectangular cavities*

Targeting high microphone performances imposes the reduction of all noise sources within the device. Some dissipation phenomena, usually considered as negligible, can then become dominant and have therefore to be taken into account if an accurate model of the device is to be achieved. Thermal dissipation within the Back Volume is a prime example of such a phenomenon, generally overlooked in the **MEMS** microphones' design process: the usual approximation of a non-dissipative cavity (adiabatic approximation) becomes inaccurate when small cavities are considered.

In this appendix, the acoustic impedance of small and shallow parallelepiped cavities is studied considering thermal dissipation effects. The dimensions of the considered cavities are significantly smaller than the wavelength  $\lambda_0$  of the acoustic wave:  $\lambda_0 \ll \sqrt[3]{V_c}$ ,  $V_c$  being the volume of the cavity.

### 1. Preliminary considerations

The thermo-viscous acoustic behavior of ideal gases is governed by the Full Linearized Navier-Stokes (FLNS) equations, which are the fundamental conservation principles for mass (1), momentum (2), and energy (3) [82], [83] linearized under the assumption of small fluctuations around the equilibrium state. The gas is described in terms of particle velocity  $v$ , acoustic pressure  $p$ , temperature  $\tau$  and density  $\rho$ , fluctuating around the static state of the medium defined by the static pressure  $P_0$ , average temperature  $T_0$ , density at rest  $\rho_0$  and heat capacity at constant pressure  $c_P$ .

$$\begin{aligned} \frac{\partial \rho}{\partial t} + \rho_0 \nabla \cdot v &= 0 & 1 \\ \rho_0 \frac{\partial v}{\partial t} &= b - \nabla p + \nabla \cdot \bar{\bar{\sigma}}_v & 2 \\ \rho_0 c_P \frac{\partial \tau}{\partial t} - \frac{\partial p}{\partial t} &= h - \nabla \cdot q . & 3 \end{aligned}$$

In these equations,  $b$  is the external body force per unit volume,  $\bar{\bar{\sigma}}_v$  the stress tensor describing the viscous effects,  $h$  the heat source and  $q$  the heat flux established between the particles by thermal conduction. The heat flux is given by Fourier's law, with  $\kappa$  the thermal conductivity of the gas:

$$q = -\kappa \nabla \tau . \quad 4$$

Furthermore, under normal conditions of pressure and temperature, air can be assumed to behave as an ideal gas. Therefore, the variables defining its static state verify the following state equation:

$$P_0 = \rho_0 r T_0 , \quad 5$$

where  $r = R/M_{air}$  is the specific constant of the air,  $R$  being the universal gas constant and  $M_{air}$  the molecular mass of air. This equation is assumed to still hold for small fluctuations around the static state of the medium. It can be used to express the mass conservation law (1) in terms of fluctuations of pressure and temperature as follows:

$$\frac{1}{P_0} \frac{\partial p}{\partial t} - \frac{1}{T_0} \frac{\partial \tau}{\partial t} = -\nabla \cdot v . \quad 6$$

### Momentum conservation law

Since the wavelength of the acoustic wave is considered to be much larger than the dimensions of the cavity, it can be safely assumed that the pressure field is spatially uniform within the cavity, and presents no spatial variations at the vicinity of the walls. It can therefore be concluded that the pressure field is only time dependent, and that the viscosity effects are insignificant, rendering all terms of the momentum conservation law (2) negligible.

### Mass conservation law

The mass conservation law is applied to the air in the cavity by integrating equation (6) over the cavity volume:

$$\iiint_{V_c} \left( \frac{1}{P_0} \frac{\partial p}{\partial t} - \frac{1}{T_0} \frac{\partial \tau}{\partial t} \right) dV = \iiint_{V_c} (-\nabla \cdot v) dV . \quad 7$$

Since the divergence of the velocity vector  $\nabla \cdot v$  is the rate of volume expansion, the right hand side of the equation is the temporal variation of the total volume of air:

$$\iiint_{V_c} (-\nabla \cdot v) dV = -\frac{\partial \delta V}{\partial t} .$$

Moreover, as the pressure field is constant over the entire volume of the cavity, equation (7) can be rewritten as follows:

$$\frac{V_c}{P_0} \frac{\partial p}{\partial t} - \frac{1}{T_0} \iiint_{V_c} \left( \frac{\partial \tau}{\partial t} \right) dV = -\frac{\partial \delta V}{\partial t} . \quad 8$$

Finally, by considering the mean variation of temperature within the cavity  $\bar{\tau}$ , the equation can be further simplified to:

$$\frac{V_c}{P_0} \frac{\partial p}{\partial t} - \frac{V_c}{T_0} \frac{\partial \bar{\tau}}{\partial t} = -\frac{\partial \delta V}{\partial t} . \quad 9$$

which, under the harmonic approximation leads to the following form:

$$\frac{p}{P_0} - \frac{\bar{\tau}}{T_0} = -\frac{\delta V}{V_c} . \quad 10$$



## Energy conservation law

Assuming the absence of any heat source within the cavity, the energy conservation law ( 3) under the harmonic approximation is written:

$$i\omega\rho_0c_p\tau - i\omega p - \kappa\Delta\tau = 0 , \quad 11$$

This equation describes the heat diffusion in the cavity, a process that starts at the boundaries then penetrates within the medium. The penetration depth is defined by the thickness  $\delta_h$  of what is commonly referred to as thermal boundary layers. These layers represent the region of the medium in which thermal dissipation is dominant, i.e. the parts of the air in the cavity that are dissipating their thermal energy. The

diffusion can thus be characterized by a complex wavenumber  $k_h = \sqrt{\frac{-i\omega\rho_0c_p}{\kappa}} = (1 + i)/\delta_h$ , with  $\delta_h = \sqrt{2\kappa/\rho_0c_p\omega}$ :

$$\Delta\tau + k_h^2\tau + \frac{i\omega}{\kappa}p = 0 . \quad 12$$

## Cavity Impedance

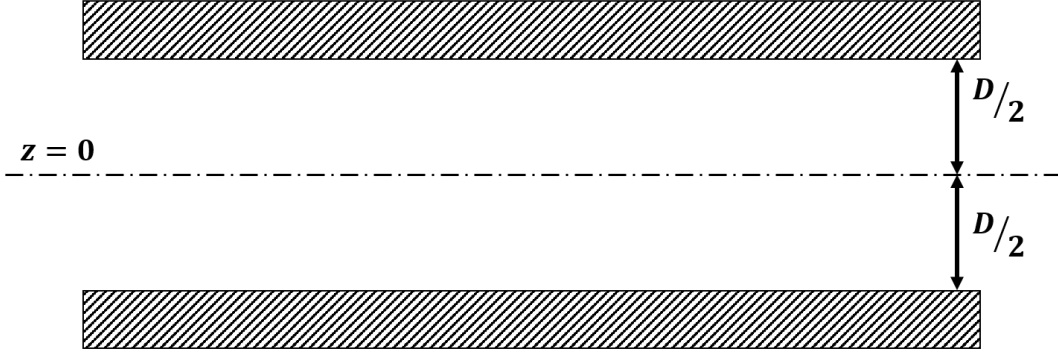
The acoustic impedance of the cavity is defined as the ratio of the variation of pressure to the flow rate  $w$  of air into the enclosure. As the flow rate into the cavity is equivalent to the opposite of the temporal variations of the total volume of air, the cavity impedance is given as:

$$Z = \frac{p}{w} = -\frac{p}{\frac{\partial\delta V}{\partial t}} . \quad 13$$

The relation between the pressure and the rate of volume variation can be obtained from the equation given by the mass conservation law (9). However, it is first necessary to solve the equation of thermal equilibrium ( 12), to express the remaining unknown  $\tau$  as a function of the pressure.

## 2. Two parallel plates approximation (1D model)

The considered cavity is parallelepiped in shape, with a depth  $D$  much smaller than its other dimensions. In this case, it can be assumed that the thermal dissipation at the shorter sides of the cavity is negligible, and the enclosure can be equated to one formed by two parallel infinite plates (**Figure B.2**) [84]. Furthermore, the cavity is usually made of materials that have a much higher heat capacity and thermal conductivity than air, such as metals or semiconductors. The boundaries of the cavity can therefore be considered as isothermal.



**Figure B.2: Schematic of a cavity with a depth  $D$  in the two parallel infinite plates approximation.**

The equation of thermal equilibrium can be more conveniently rewritten as

$$\Delta\tau + k_h^2\left(\tau - \frac{T_0(\gamma-1)}{P_0\gamma}p\right) = 0. \quad 14$$

where  $\gamma = c_p/c_v$ , and equation (5) and Mayer's relation are used to make the transformation. The general solution of this equation is of the following form, where  $A_1$  and  $A_2$  are constants:

$$\tau = A_1 e^{ik_h z} + A_2 e^{-ik_h z} + \frac{T_0(\gamma-1)}{P_0\gamma}p$$

Applying isothermal boundary conditions for  $z = \pm D/2$  we find:

$$\tau = \frac{T_0(\gamma-1)}{P_0\gamma}p \left[ 1 - \frac{\cos(k_h z)}{\cos(k_h D/2)} \right]. \quad 15$$

To find the average variation of temperature in the cavity, the result is averaged over  $z = \pm D/2$ :

$$\bar{\tau} = \frac{T_0(\gamma-1)}{P_0\gamma}p \left[ 1 - \frac{\tan(k_h D/2)}{k_h D/2} \right]. \quad 16$$

Injecting now the expression of  $\bar{\tau}$  into equation (10) we find:

$$\frac{\delta V}{V_0} = \frac{P_1}{P_0} \left[ \frac{(\gamma-1)}{\gamma} \left( 1 - \frac{\tan(k_h D/2)}{k_h D/2} \right) - 1 \right],$$

leading to the following cavity impedance, where  $C_a = \frac{V_c}{\gamma P_0}$  is the adiabatic compliance:

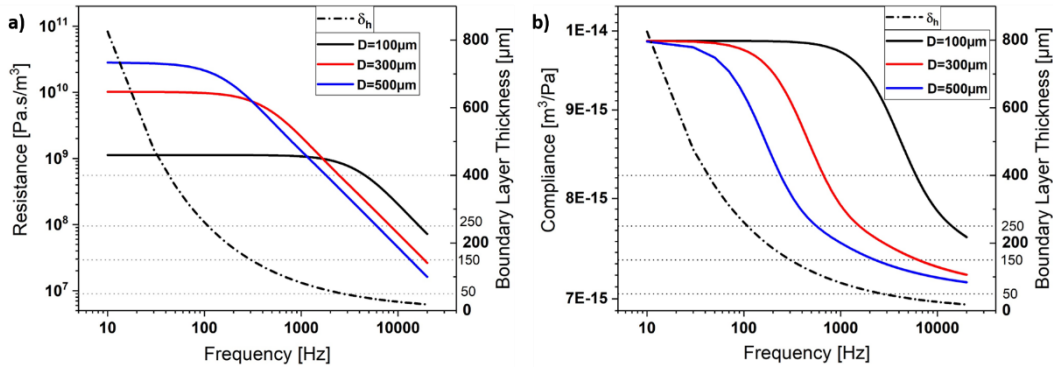
$$Z_c = \frac{1}{i\omega C_a \left[ 1 + (\gamma-1) \left( \frac{\tan(k_h D/2)}{k_h D/2} \right) \right]}. \quad 17$$

Unlike the impedance obtained under the adiabatic approximation ( $Z_a = 1/i\omega C_a$ ), the resulting cavity impedance is a complex number, with both real and imaginary parts. Noting that  $k_h$  is a complex factor, it is not possible to analytically separate the impedance into a real part  $R_c$ , displaying the resistive effects due to thermal dissipation, and a capacitive part  $C_c$  indicating the acoustic compliance of the

enclosure. This can only be achieved numerically. What is more, the cavity's resistance and compliance are not constant and vary as functions of the frequency.

$$Z_c(\omega) = R_c(\omega) + \frac{1}{i\omega C_c(\omega)}$$

**Figure B.3** shows the variations of a  $1\text{mm}^3$  cavity's resistance and compliance, for different cavity depths. Concerning the resistance of the cavity, we note the presence of two regimes: a saturation regime for low frequencies, and a decrease regime for higher frequencies. These two regimes are best understood when the thickness of the boundary layers is considered. As it can be seen in **Figure B.3.a**, for a cavity depth of  $100\ \mu\text{m}$ , the saturation regime spans to around  $3\ \text{kHz}$ . Along this frequency range, the thickness of the boundary layers is greater than half of the cavity depth. This means that, below  $3\ \text{kHz}$ , the cavity is entirely filled with the boundary layers. The thermal dissipation is therefore at its maximum: any variation of temperature is directly dissipated in the cavity walls and the entire cavity is under isothermal conditions. When the thickness of the boundary layers becomes smaller than half of the cavity height, the regime changes, and the resistance decreases proportionally to  $f^{-3/2}$ . This regime change is also seen in the cavity's compliance as shown by **Figure B.3.b**. For low frequencies, the compliance plateaus at around its isothermal value ( $C = V_c/P_0$ ) since the cavity is filled by the thermal boundary layers. Once the layers become smaller than the cavity height, the compliance starts decreasing and converging towards its adiabatic value ( $C_a = V_c/\gamma P_0$ ). Thus, we conclude that the impedance of the cavity passes through two regimes: an isothermal saturation regime at low frequencies, and a decreasing regime for higher frequencies.



**Figure B.3:** Variations of a  $1\text{mm}^3$  cavity's resistance (a) and compliance (b) in the two parallel plates approximation as a function of the frequency.

### 3. ‘Big’ small cavity approximation

By considering the thickness of the boundary layers and the 1D model, a satisfying explanation can be given to the low frequency saturation regime of the cavity's impedance. However, due to the complexity of the terms in the impedance, this model is inadequate for a deeper study of the high frequency regime. This regime is characterized by the strong decrease in the thickness of the thermal

boundary layers. The impedance of the cavity can then be studied by considering that, despite being ‘small’, the cavity remains ‘big’ compared to the thickness of the layers:  $\delta_h \ll \sqrt[3]{V_c}$ . This means that thermal dissipation only affects elements right next the boundaries, while the other elements remain unaffected.

Bruneau has provided a solution for the impedance of the cavity within these considerations, showing that, in the absence of any heat sources, the pressure within the cavity is equal to [85]:

$$p = \frac{-\gamma P_0 \delta V}{V_c} \frac{1}{\left[ 1 + \frac{(1-i)S}{\sqrt{2}} \frac{S}{V_c} (\gamma-1) \sqrt{\frac{\lambda}{\rho_0 c_p \omega}} \right]}, \quad 18$$

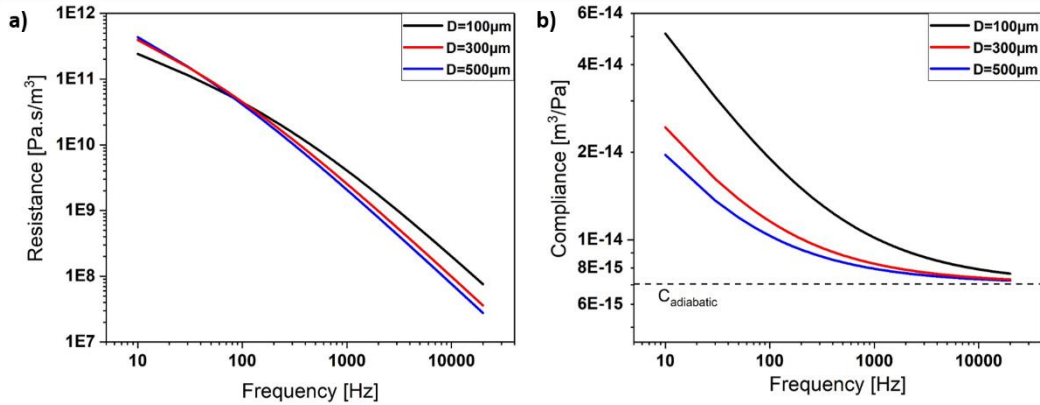
where  $S$  is the inner surface of the cavity. By defining  $\eta_0 = \frac{S}{V} (\gamma - 1) \sqrt{\frac{\lambda}{2\rho_0 c_p}}$ , a simplified expression of the cavity impedance can be obtained:

$$Z_{bsc} = \frac{1}{i\omega C_a} \frac{1}{[1+(1-i)\eta_0/\sqrt{\omega}]} = R_{bsc}(\omega) + \frac{1}{i\omega C_{bsc}(\omega)}. \quad 19$$

This is a simpler expression than the one given by the 1D model, and it can be easily separated into real (resistive) and imaginary (compliant) parts:

$$R_{bsc} = \frac{\eta_0}{C_a(\omega^{3/2} + 2\eta_0^2\sqrt{\omega} + 2\eta_0\omega)} \quad \text{and} \quad C_{bsc} = \frac{C_a(1 + 2\eta_0^2/\omega + 2\eta_0/\sqrt{\omega})}{(1 + \eta_0/\sqrt{\omega})}$$

It can now be clearly seen that the decrease of the resistance, proportional to  $f^{-3/2}$  at high frequency, and the increased compliance at low frequencies, result directly from the thermal dissipation effects and the thickness of the thermal boundary layers ( $\propto \omega^{-1/2}$ ). Furthermore, the resistance and the compliance only have one regime, which was expected under this approximation, as, no matter the frequency, the cavity is never entirely filled with the thermal boundary layers. This is evidenced in **Figure B.4**: for a  $1 \text{ mm}^3$  cavity, the resistance and the compliance keep increasing for lower frequencies, never reaching a plateau regime.



**Figure B.4:** Variation of a  $1 \text{ mm}^3$  cavity's resistance (a) and compliance (b) in the ‘big’ small cavity approximation as a function of the frequency.

## 4. Numerical model

As we have previously shown, finding the cavity impedance requires finding the average temperature variation in the enclosure's volume. This can also be done by numerically solving the thermal equilibrium equation while applying the correct boundary conditions. Unlike the two previous approximations, this approach gives the exact numerical value of the cavity impedance without any approximations. However, it can prove time consuming depending the required level of preciseness. In the following, the Comsol mathematics module solver has been used to implement and solve the thermal equilibrium equation onto different cavity sizes.

From the equation of thermal equilibrium ( 14), it can be concluded that the temperature fluctuations within the cavity can have a maximum value of  $\frac{T_0(\gamma-1)}{P_0\gamma}p$  and a minimum possible value of 0 (at the isothermal boundaries). Therefore, the solutions of the equation can have the following simplified form:

$$T_1 = \varphi_T \cdot T_a$$

In which  $\varphi_T$  is the solution of the following Partial Differential Equation (PDE):

$$\Delta[\varphi_T - 1] - \beta^2[\varphi_T - 1] = 0 . \quad 20$$

$\varphi_T$  greatly simplifies the numerical solution of the problem, as it directly leads to the cavity impedance which can be written:

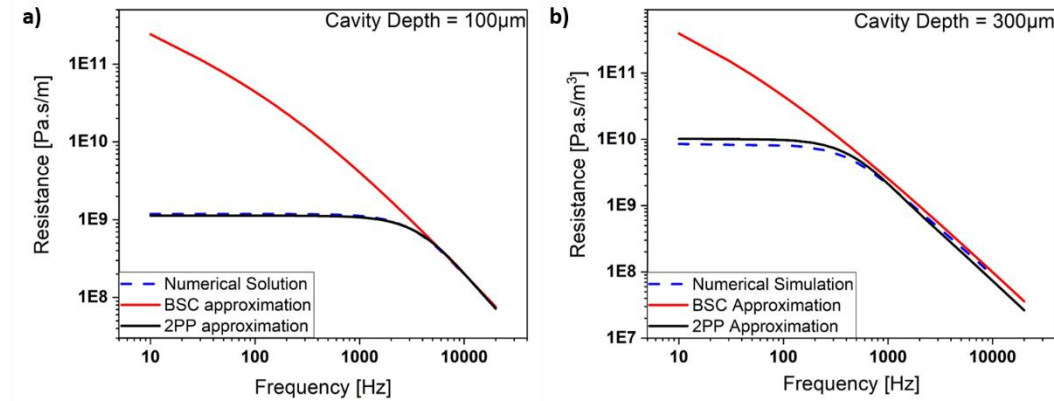
$$Z = \frac{1}{i\omega C_a} \frac{1}{\gamma - (\gamma - 1) \frac{\overline{T_1}}{T_a}} = \frac{1}{i\omega C_a} \frac{1}{\gamma - (\gamma - 1)\varphi_T}$$

Thus, we can numerically find the volume average of the  $\varphi_T$  function, and then directly calculate the resulting cavity impedance, without having to take into account the pressure fluctuations. This was done by solving the PDE (20) in the following weak form:

$$- \int_V \nabla(\delta\varphi_T) \cdot \nabla\varphi_T dV - \beta^2 \int_V (\delta\varphi_T) \cdot \varphi_T dV + \int_V (\delta\varphi_T) \cdot \beta^2 dV = 0$$

where  $\delta\varphi_T$  is the test function. Dirichlet boundary conditions were applied at the cavity's isothermal walls, and  $\overline{\varphi_T}$  was calculated for several cavity sizes and depths. As it can be seen in **Figure B.5**, the numerically calculated impedance agrees very well with the two parallel plates hypothesis for a small ( $1 \text{ mm}^3$ ) and very shallow ( $100 \mu\text{m}$  in depth) cavity. However, as soon as the cavity height increases ( $300 \mu\text{m}$ ), we find a difference between the two solutions. This discrepancy is due to the fact that the numerical solution takes into account the dissipation and the thickness of the thermal boundary layers at the edges of the cavity. When considered, the added boundary layers should lead to cavity saturation at a higher frequency (boundary layers closing in from all sides). This explains why the numerically calculated resistance reaches its plateau or saturation regime at a higher

frequency than in the 1D model. We should note that, all hypotheses converge at high frequencies, with a lower resistance for the 1D model due to the lack of dissipation at the sides.



**Figure B.5: Comparison between the numerical solution and the analytical approaches for  $1 \text{ mm}^3$  cavities with depths of  $100 \text{ }\mu\text{m}$  (left) and  $300 \text{ }\mu\text{m}$  (right).**

## 5. Conclusion

When thermal dissipation effects are considered, the impedance of a small cavity exhibits a dissipative and resistive real part in addition to the compliant imaginary part. The obtained resistance and compliance both depend on the geometry and the size of the cavity, and are functions of the frequency. For finding the impedance of the cavity, the choice of approach and approximation greatly depends on the considered cavity's dimensions.

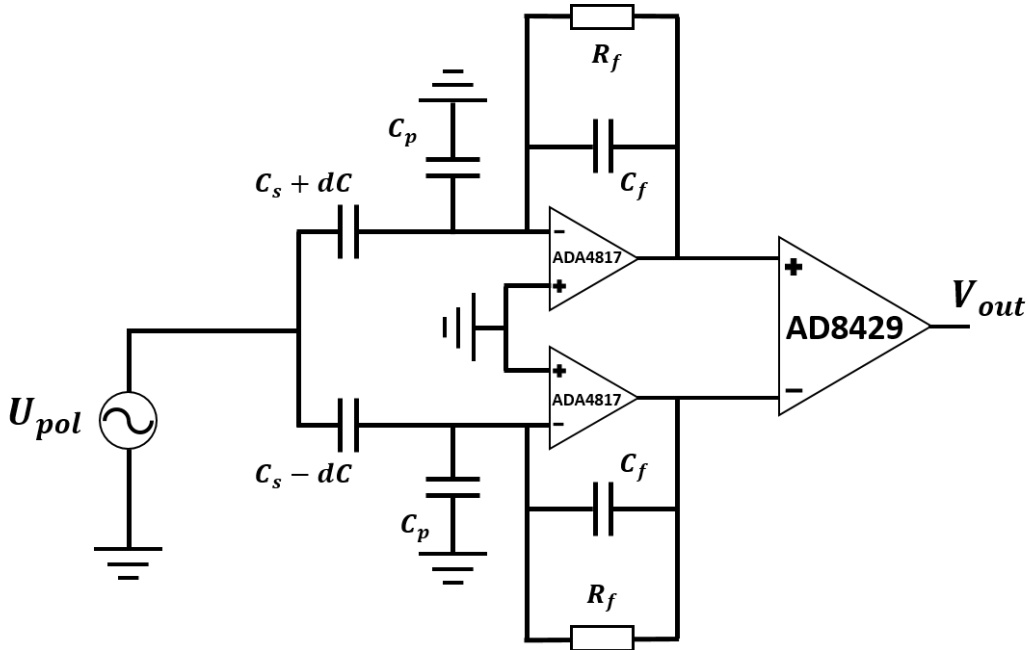
On one hand, even though it does not take into account the dissipation at the cavity's side walls, the 1D model does give an exact solution and is suitable for small and shallow cavities. However, the impedance given by this approach cannot be analytically separated into the resistive and compliant parts, which makes it more difficult to integrate into lumped elements models. On the other hand, the 'big' small cavity approximation is only suitable for big and deep cavities for which the thickness of the boundary layers quickly becomes smaller than the cavity depth. However, these two approaches remain approximations, giving an approximate model, which does not greatly differ from reality. Nevertheless, for exact calculations, the numerical approach remains the most reliable.

## Appendix C. Electronic Readout Circuit

In this appendix, the electronic readout circuit, based on which the microphones are designed, is presented and its noise and performance are briefly discussed. The considered circuit is a charge to voltage converter with a differential readout architecture, required for the differential operation of the microphones. As it can be seen in **Figure C.6**, the equal sensor capacitances  $C_{s1}$  and  $C_{s2}$  are polarized by a polarization voltage  $U_{pol}$  modulated at a frequency  $\omega_m$ . The charge variation  $dC$  of each signal capacitance is first amplified by a separate charge amplifier, composed of an operational amplifier (OPA) with a feedback capacitance  $C_f$  and resistance  $R_f$ . Then, an Instrumentation Amplifier (INA) performs the difference between the outputs of each branch. For an INA gain  $G_{INA}$ , if ideal circuit operation is considered and both branches of the circuit are symmetrical, the output is shown to be equal to:

$$V_{out} = G_{INA} U_{pol} \frac{2dC}{C_f}, \quad 21$$

where  $dC$  is the differential variation of capacitance.



**Figure C.6: Schematic of the electronic circuit considered during the design process.**

In order to study the performance of the circuit, it is important to consider the noise contributions of all of its elements, starting with the charge amplification stage. The input-referred voltage noise of the charge amplifier is shown to be equal to:

$$S_{CA}^2(j\omega) = S_v^2 \left( 1 + \frac{C_p + C_s}{C_f} \right)^2 + \left[ S_i^2 + \left( \frac{S_R}{R_f} \right)^2 \right] \frac{1}{(j\omega C_f)^2},$$

where  $C_p$  is the parasitic capacitance parallel to  $C_s$ . The noise is the sum of three contributions:

- $S_v$ , the input-referred voltage noise of the OPA, amplified by the noise gain of the amplifier. The effect of this contribution can be minimized by reducing the parasitic capacitance and choosing an OPA with a low input-referred voltage noise.
- $S_i$ , the input current noise of the OPA integrated into the feedback capacitance, which can be reduced by working at high frequency and by choosing an OPA with a low input current noise.
- $S_R = \sqrt{4k_bTR_f}$ , the thermal noise of the feedback resistance filtered by the feedback capacitance. The contribution of this term can be decreased by choosing a large feedback resistance and by working at high frequency.

Taking into account the noise contributions of both charge amplifier branches as well as the input-referred voltage noise of the INA  $S_{INA}$ , the total noise of the electronic circuit is found:

$$S_{out}^2 = G_{INA}^2 [2S_{CA}^2 + S_{INA}^2] . \quad 22$$

Thus, to reduce the total noise of the circuit, the choice was made to work at high frequency with a polarization voltage modulated at 100 kHz, far beyond the operational bandwidth of the microphones. The considered OPAs are model ADA4817 amplifiers from Analog Devices, which exhibit a good tradeoff between input-referred voltage noise at  $4 \text{ nV}/\sqrt{\text{Hz}}$  and input current noise at  $2.5 \text{ fA}/\sqrt{\text{Hz}}$  [86]. The considered INA is model AD8429 with an input noise of  $1.6 \text{ nV}/\sqrt{\text{Hz}}$  for a gain of 100 [87]. As for the values of the feedback resistance and capacitance, the best performance in terms of noise was found for values of  $2 \text{ G}\Omega$  and  $1 \text{ pF}$ , while the parasitic capacitances are estimated at  $3 \text{ pF}$ .

With the obtained circuit noise, the **SNR** of the electronic circuit can be written as:

$$SNR_{elec} = \frac{U_{pol} \frac{\Delta C}{C_f}}{\sqrt{\int_{BW} (2S_{CA}^2 + S_{INA}^2) \cdot \sqrt{2}}}, \quad 23$$

in which the circuit noise is integrated over the bandwidth of operation **BW**, and the demodulation loss is taken into account with the  $\sqrt{2}$  factor. It can be concluded from this expression that, for a set polarization voltage, the variation of capacitance can be increased to increase the **SNR** of the device and make sure that the electronic noise does not limit the performance of the microphone. In other words, increasing the signal of the **MEMS** sensor masks the effect of the circuit's noise.

From a design point of view, it is more convenient to consider the dynamic range **DR** of the device, given by the expression of  $SNR_{elec}$  for the highest microphone signal, i.e. the maximum variation of capacitance. Replacing  $dC$  in **equation (23)** by its linear expression given in **equation (3.16)**, the **DR** is written:



$$DR = \frac{2U_{pol} \frac{C_s}{C_f} \tilde{z}_{e_n}}{\sqrt{2S_{CA}^2 + S_{INA}^2 \cdot \sqrt{2} \cdot \sqrt{BW}}}, \quad 24$$

where  $\tilde{z}_{e_n}$  is the normalized maximal gap variation. It is thus apparent that, with the considered circuit and for a set polarization voltage, the **DR** of the device is only determined by the signal capacitance and the displacement of the electrode, which have a direct impact on the size of the device and on the design of the mechanical structure.

# Bibliography

- [1] J. Eargle, *The microphone book*. Oxford: Focal Press, 2004.
- [2] E. C. Wentz, ‘Telephone-Transmitter’, US 1333744, Mar. 1920.
- [3] M. T. Du Moncel, ‘Condensateur employé comme transmetteur (p.286)’, *La Lumière Electrique*, no. 16, Apr. 16, 1881.
- [4] E. C. Wentz, ‘A Condenser Transmitter as a Uniformly Sensitive Instrument for the Absolute Measurement of Sound Intensity’, *Physical Review*, vol. 10, no. 1, pp. 39–63, Jul. 1917, doi: 10.1103/PhysRev.10.39.
- [5] G. M. Sessler and J. E. West, ‘Electrostatic Transducer’, US 3118979, Jan. 1964.
- [6] G. M. Sessler and J. E. West, ‘Self-Biased Condenser Microphone with High Capacitance’, *The Journal of the Acoustical Society of America*, vol. 34, no. 11, 1962, doi: 10.1121/1.1909130.
- [7] G. W. Elko and K. P. Harney, ‘A History of Consumer Microphones: The Electret Condenser Microphone Meets Micro-Electro-Mechanical-Systems’, *Acoustics Today*, vol. 5, no. 2, p. 4, 2009, doi: 10.1121/1.3182845.
- [8] K. E. Petersen, ‘Silicon as a mechanical material’, *Proceedings of the IEEE*, vol. 70, no. 5, pp. 420–457, May 1982, doi: 10.1109/PROC.1982.12331.
- [9] M. Royer, M. A. Wurm, S. Aadland, and M. Glenn, ‘ZnO on Si integrated acoustic sensor’, *Sensors and Actuators*, p. 6, 1983.
- [10] D. Hohm and R. Gerhard-Multhaupt, ‘Silicon-dioxide electret transducer’, *The Journal of the Acoustical Society of America*, vol. 75, no. 4, pp. 1297–1298, Apr. 1984, doi: 10.1121/1.390738.
- [11] S. Bouwstra *et al.*, ‘Silicon microphones - a Danish perspective’, *Journal of Micromechanics and Microengineering*, vol. 8, no. 2, pp. 64–68, Jun. 1998, doi: 10.1088/0960-1317/8/2/005.
- [12] J. Bouchaud, ‘Disruptions in the MEMS microphones industry - IHS Markit’. 2017.
- [13] G. Girardin, R. Fraux, and J. Pedersen, ‘Acoustic MEMS and Audio solutions - Yole développement’. 2017.
- [14] J. Czarny, ‘Conception, fabrication et caractérisation d’un microphone MEMS’, Institut National des Sciences Appliquées de Lyon, 2015.
- [15] P. R. Scheeper, A. G. H. van der Donk, W. Olthuis, and P. Bergveld, ‘A review of silicon microphones’, *Sensors and Actuators A: Physical*, vol. 44, no. 1, pp. 1–11, Jul. 1994, doi: 10.1016/0924-4247(94)00790-X.
- [16] S. D. Senturia, *Microsystem Design*. Springer Science & Business Media, 2001.
- [17] D. Hohm and R. Gerhard-Multhaupt, ‘Silicon-dioxide electret transducer’, *The Journal of the Acoustical Society of America*, vol. 75, no. 4, pp. 1297–1298, Apr. 1984, doi: 10.1121/1.390738.
- [18] A. J. Sprekels, R. A. Groothengel, A. J. Verloop, and P. Bergveld, ‘Development of an electret microphone in silicon’, *Sensors and Actuators*,

- vol. 17, no. 3–4, pp. 509–512, May 1989, doi: 10.1016/0250-6874(89)80038-1.
- [19] D. Hohm and G. Hess, ‘A subminiature condenser microphone with silicon nitride membrane and silicon back plate’, *The Journal of the Acoustical Society of America*, vol. 85, no. 1, pp. 476–480, Jan. 1989, doi: 10.1121/1.397699.
- [20] P. R. Scheeper, W. Olthuis, and P. Bergveld, ‘Fabrication of a subminiature silicon condenser microphone using the sacrificial layer technique.’, in *Proceedings Transducers '91*, San Francisco, CA, USA, Jun. 1991, pp. 408–411.
- [21] W. Kühnel and G. Hess, ‘Micromachined subminiature condenser microphones in silicon’, *Sensors and Actuators A: Physical*, vol. 32, no. 1–3, pp. 560–564, Apr. 1992, doi: 10.1016/0924-4247(92)80044-4.
- [22] J. Bergqvist, F. Rudolf, J. Maisano, F. Parodi, and M. Rossi, ‘A silicon condenser microphone with a highly perforated backplate’, in *Proceedings Transducers '91*, San Francisco, CA, USA, Jun. 1991, pp. 266–269.
- [23] J. Bergqvist, ‘Finite-element modelling and characterization of a silicon condenser microphone with a highly perforated backplate’, *Sensors and Actuators A: Physical*, vol. 39, no. 3, pp. 191–200, Dec. 1993, doi: 10.1016/0924-4247(93)80219-7.
- [24] P. R. Scheeper, W. Olthuis, and P. Bergveld, ‘Improvement of the performance of microphones with a silicon nitride diaphragm and backplate’, *Sensors and Actuators A: Physical*, vol. 40, no. 3, pp. 179–186, Mar. 1994, doi: 10.1016/0924-4247(94)87003-9.
- [25] S. T. Cho, K. Najafi, and K. D. Wise, ‘Internal stress compensation and scaling in ultrasensitive silicon pressure sensors’, *IEEE Transactions on Electron Devices*, vol. 39, no. 4, pp. 836–842, Apr. 1992, doi: 10.1109/16.127473.
- [26] A. Torkkeli, O. Rusanen, J. Saarilahti, H. Seppä, H. Sipola, and J. Hietanen, ‘Capacitive microphone with low-stress polysilicon membrane and high-stress polysilicon backplate’, *Sensors and Actuators A: Physical*, vol. 85, no. 1–3, pp. 116–123, Aug. 2000, doi: 10.1016/S0924-4247(00)00336-8.
- [27] P. Horwath, A. Erlebach, R. Kohler, and H. Kuck, ‘Miniature Condenser Microphone With A Thin Silicon Membrane Fabricated On Simox Substrate’, in *Proceedings of the International Solid-State Sensors and Actuators Conference - TRANSDUCERS '95*, Stockholm, Sweden, 1995, vol. 2, pp. 696–699, doi: 10.1109/SENSOR.1995.721927.
- [28] M. Ying, Q. Zou, and S. Yi, ‘Finite-element analysis of silicon condenser microphones with corrugated diaphragms’, *Finite Elements in Analysis and Design*, vol. 30, no. 1–2, pp. 163–173, Jul. 1998, doi: 10.1016/S0168-874X(98)00031-6.
- [29] W. J. Wang, R. M. Lin, Q. B. Zou, and X. X. Li, ‘Modeling and characterization of a silicon condenser microphone’, *Journal of Micromechanics and Microengineering*, vol. 14, no. 3, pp. 403–409, Mar. 2004, doi: 10.1088/0960-1317/14/3/013.
- [30] Yafan Zhang and K. D. Wise, ‘Performance of nonplanar silicon diaphragms under large deflections’, *Journal of Microelectromechanical Systems*, vol. 3, no. 2, pp. 59–68, Jun. 1994, doi: 10.1109/84.294322.
- [31] X. Li, R. Lin, H. Kek, J. Miao, and Q. Zou, ‘Sensitivity-improved silicon condenser microphone with a novel single deeply corrugated diaphragm’,

- Sensors and Actuators A: Physical*, vol. 92, no. 1–3, pp. 257–262, Aug. 2001, doi: 10.1016/S0924-4247(01)00582-9.
- [32] P. R. Scheeper, W. Olthuis, and P. Bergveld, ‘The design, fabrication, and testing of corrugated silicon nitride diaphragms’, *Journal of Microelectromechanical Systems*, vol. 3, no. 1, pp. 36–42, Mar. 1994, doi: 10.1109/84.285722.
- [33] S. B. Sedaghat and B. A. Ganji, ‘A novel MEMS capacitive microphone using spring-type diaphragm’, *Microsystem Technologies*, vol. 25, no. 1, pp. 217–224, Jan. 2019, doi: 10.1007/s00542-018-3951-x.
- [34] Chan, Lai, M. Wu, Wang, and W. Fang, ‘Design and Implementation of a Capacitive-type Microphone with Rigid Diaphragm and Flexible Spring Using the Two Poly Silicon Micromachining Processes’, *IEEE Sensors Journal*, 2011, doi: 10.1109/JSEN.2011.2121060.
- [35] A. Kovacs and A. Stoffel, ‘Fabrication of single-chip polysilicon condenser structures for microphone applications’, *Journal of Micromechanics and Microengineering*, vol. 5, no. 2, pp. 86–90, Jun. 1995, doi: 10.1088/0960-1317/5/2/007.
- [36] A. Kovács and A. Stoffel, ‘Mechanical analysis of polycrystalline and single-crystalline silicon microstructures’, *Sensors and Actuators A: Physical*, vol. 42, no. 1–3, pp. 672–679, Apr. 1994, doi: 10.1016/0924-4247(94)80073-1.
- [37] M. Fu, A. Dehe, and R. Lerch, ‘Analytical analysis and finite element simulation of advanced membranes for silicon microphones’, *IEEE Sensors Journal*, vol. 5, no. 5, pp. 857–863, Oct. 2005, doi: 10.1109/JSEN.2004.841449.
- [38] A. Dehe, M. Wurzer, M. Fuldner, and U. Krumbein, ‘Design of a poly silicon MEMS microphone for high signal-to-noise ratio’, in *2013 Proceedings of the European Solid-State Device Research Conference (ESSDERC)*, Bucharest, Romania, Sep. 2013, pp. 292–295, doi: 10.1109/ESSDERC.2013.6818876.
- [39] P. Malcovati and A. Baschiroto, ‘The Evolution of Integrated Interfaces for MEMS Microphones’, *Micromachines*, vol. 9, no. 7, p. 323, Jun. 2018, doi: 10.3390/mi9070323.
- [40] H. B. Callen and T. A. Welton, ‘Irreversibility and Generalized Noise’, *Physical Review*, vol. 83, no. 1, pp. 34–40, Jul. 1951, doi: 10.1103/PhysRev.83.34.
- [41] T. B. Gabrielson, ‘Mechanical-thermal noise in micromachined acoustic and vibration sensors’, *IEEE Transactions on Electron Devices*, vol. 40, no. 5, pp. 903–909, May 1993, doi: 10.1109/16.210197.
- [42] Z. Škvor, ‘On the acoustical resistance due to viscous losses in the air gap of electrostatic transducers’, *Acta Acustica united with Acustica*, vol. 19, no. 5, 1967.
- [43] M. Fuldner and A. Dehe, ‘Challenges of high SNR (Signal-to-Noise) Silicon micromachined microphones.’, presented at the 19th International Congress on Acoustics, Madrid, Spain, Sep. 2007.
- [44] J. Bay, O. Hansen, and S. Bouwstra, ‘Design of a silicon microphone with differential read-out of a sealed double parallel-plate capacitor’, *Sensors and Actuators*, pp. 232–236, 1996.
- [45] J. Bay, O. Hansen, and S. Bouwstra, ‘Micromachined double backplate differential capacitive microphone’, *Journal of Micromechanics and*

- Microengineering*, vol. 9, no. 1, pp. 30–33, Mar. 1999, doi: 10.1088/0960-1317/9/1/003.
- [46] P. Rombach, M. MuÈllenborn, U. Klein, and K. Rasmussen, ‘The first low voltage, low noise differential silicon microphone, technology development and measurement results’, p. 6, 2002.
- [47] D. T. Martin, J. Liu, K. Kadirvel, R. M. Fox, M. Sheplak, and T. Nishida, ‘A Micromachined Dual-Backplate Capacitive Microphone for Aeroacoustic Measurements’, *Journal of Microelectromechanical Systems*, vol. 16, no. 6, pp. 1289–1302, Dec. 2007, doi: 10.1109/JMEMS.2007.909234.
- [48] D. T. Martin, ‘Design, Fabrication and Characterization of a MEMS Dual-Backplate Capacitive Microphone’, University of Florida, 2007.
- [49] M. Fùldner and A. Dehé, ‘Dual Back Plate Silicon MEMS Microphone: Balancing High Performance!’, p. 3, 2015.
- [50] B.-H. Kim and H.-S. Lee, ‘Acoustical-Thermal Noise in a Capacitive MEMS Microphone’, *IEEE Sensors Journal*, vol. 15, no. 12, pp. 6853–6860, Dec. 2015, doi: 10.1109/JSEN.2015.2464372.
- [51] C.-I. Chang, S.-C. Lo, C. Wang, Y.-C. Sun, and W. Fang, ‘Novel in-plane gap closing CMOS-MEMS microphone with no back-plate’, in *2014 IEEE 27th International Conference on Micro Electro Mechanical Systems (MEMS)*, San Francisco, CA, USA, Jan. 2014, pp. 136–139, doi: 10.1109/MEMSYS.2014.6765592.
- [52] S.-C. Lo *et al.*, ‘Development of a no-back-plate SOI MEMS condenser microphone’, in *2015 Transducers - 2015 18th International Conference on Solid-State Sensors, Actuators and Microsystems (TRANSDUCERS)*, Anchorage, AK, USA, Jun. 2015, pp. 1085–1088, doi: 10.1109/TRANSDUCERS.2015.7181115.
- [53] S.-C. Lo, J.-J. Wang, M. Wu, and W. Fang, ‘Sensitivity improvement of no-back-plate MEMS microphone using polysilicon trench-refilled process’, in *2017 19th International Conference on Solid-State Sensors, Actuators and Microsystems (TRANSDUCERS)*, Kaohsiung, Jun. 2017, pp. 1171–1174, doi: 10.1109/TRANSDUCERS.2017.7994262.
- [54] W.-J. Mao, C.-L. Cheng, S.-C. Lo, Y.-S. Chen, and W. Fang, ‘Design and implementation of a CMOS-MEMS microphone without the back-plate’, in *2017 19th International Conference on Solid-State Sensors, Actuators and Microsystems (TRANSDUCERS)*, Kaohsiung, Jun. 2017, pp. 1037–1040, doi: 10.1109/TRANSDUCERS.2017.7994229.
- [55] J. Manz, G. Bosetti, A. Dehe, and G. Schrag, ‘A novel silicon “star-comb” microphone concept for enhanced signal-to-noise-ratio: Modeling, design and first prototype’, in *2017 19th International Conference on Solid-State Sensors, Actuators and Microsystems (TRANSDUCERS)*, Kaohsiung, Jun. 2017, pp. 67–70, doi: 10.1109/TRANSDUCERS.2017.7993989.
- [56] G. Bosetti, J. Manz, A. Dehé, U. Krumbein, and G. Schrag, ‘Modeling and physical analysis of an out-of-plane capacitive MEMS transducer with dynamically coupled electrodes’, *Microsystem Technologies*, Mar. 2019, doi: 10.1007/s00542-018-04290-2.
- [57] R. P. Ried, Eun Sok Kim, D. M. Hong, and R. S. Muller, ‘Piezoelectric microphone with on-chip CMOS circuits’, *Journal of Microelectromechanical Systems*, vol. 2, no. 3, pp. 111–120, Sep. 1993, doi: 10.1109/84.260255.

- [58] Eun Sok Kim and R. S. Muller, 'IC-Processed piezoelectric microphone', *IEEE Electron Device Letters*, vol. 8, no. 10, pp. 467–468, Oct. 1987, doi: 10.1109/EDL.1987.26696.
- [59] T.-L. Ren, L.-T. Zhang, L.-T. Liu, and Z.-J. Li, 'Design of a new PZT based microphone and microspeaker', *Integrated Ferroelectrics*, vol. 41, no. 1–4, pp. 101–106, Jan. 2001, doi: 10.1080/10584580108012812.
- [60] G. M. Sessler, 'Acoustic Sensors', *Sensors and Actuators A: Physical*, vol. 26, Mar. 1991, doi: 10.1016/0924-4247(91)87011-Q.
- [61] R. Littrell, 'High Performance Piezoelectric MEMS Microphones', University of Michigan, 2010.
- [62] R. Littrell and K. Grosh, 'Modeling and Characterization of Cantilever-Based MEMS Piezoelectric Sensors and Actuators', *Journal of Microelectromechanical Systems*, vol. 21, no. 2, pp. 406–413, Apr. 2012, doi: 10.1109/JMEMS.2011.2174419.
- [63] R. Littrell and K. Grosh, 'Noise minimization in micromachined piezoelectric microphones', Montreal, Canada, 2013, pp. 030041–030041, doi: 10.1121/1.4799674.
- [64] 'Vesper - VM1010 - Datasheet' . .
- [65] F. A. Levinzon, 'Fundamental Noise Limit of Piezoelectric Accelerometer', *IEEE Sensors Journal*, vol. 4, no. 1, pp. 108–111, Feb. 2004, doi: 10.1109/JSEN.2003.820366.
- [66] M. Ahmad, 'A Simple Scheme for Loss Angle Measurement of a Capacitor', *IEEE Transactions on Energy Conversion*, vol. 19, no. 1, pp. 228–229, Mar. 2004, doi: 10.1109/TEC.2003.822328.
- [67] Y. Seo, D. Corona, and N. A. Hall, 'On the theoretical maximum achievable signal-to-noise ratio (SNR) of piezoelectric microphones', *Sensors and Actuators A: Physical*, vol. 264, pp. 341–346, Sep. 2017, doi: 10.1016/j.sna.2017.04.001.
- [68] R. Littrell and K. Grosh, 'Noise minimization in micromachined piezoelectric microphones', Montreal, Canada, 2013, pp. 030041–030041, doi: 10.1121/1.4799674.
- [69] M. Akiyama, K. Umeda, A. Honda, and T. Nagase, 'Influence of scandium concentration on power generation figure of merit of scandium aluminum nitride thin films', *Applied Physics Letters*, vol. 102, no. 2, p. 021915, Jan. 2013, doi: 10.1063/1.4788728.
- [70] S. Fichtner *et al.*, 'Identifying and overcoming the interface originating c-axis instability in highly Sc enhanced AlN for piezoelectric micro-electromechanical systems', *Journal of Applied Physics*, vol. 122, no. 3, p. 035301, Jul. 2017, doi: 10.1063/1.4993908.
- [71] 'Knowles - SPM0687LR5H-1 - Datsheet' . .
- [72] 'TDK InvenSense - ICS-40730 microphone - Datasheet' . .
- [73] 'Infineon - IM69D130 microphone - Datasheet' . .
- [74] A. Dehe and R. Helm, 'SENSOR STRUCTURE FOR SENSING PRESSURE WAVES AND AMBIENT PRESSURE', US 9670059 B2, 2017.
- [75] J. Reinmuth, V. Rajaraman, D. Meisel, and B. Gehl, 'MICROPHONE WITH ENCAPSULATED MOVING ELECTRODE', US 2018/0352341 A1, 2018.
- [76] M. Knecht, 'New Capacitive MEMS Design Boosts Audio Pickup Quality', *EE Times Europe*, Feb. 2019.

- [77] L. Joet, 'DISPOSITIF DE TRANSMISSION D'UN MOUVEMENT ET D'UNE FORCE ENTRE DEUX ZONES ISOLEES L'UNE DE L'AUTRE', FR3059659\_B1, 2019.
- [78] S. P. Timoshenko and S. Woinowsky-Krieger, *Theory of plates and shells*. McGraw-hill, 1959.
- [79] M. J. Madou, *Fundamentals of Microfabrication: the science of miniaturization*, Second Edition. CRC Press, 2002.
- [80] C. Acar and A. Shkel, *MEMS vibratory gyroscopes: structural approaches to improve robustness*. Springer Science & Business Media, 2008.
- [81] 'Akustica - AKU250 microphone - Datasheet' . .
- [82] T. Verdot, E. Redon, K. Ege, J. Czarny, C. Guianvarc'h, and J.-L. Guyader, 'Microphone with Planar Nano-Gauge Detection: Fluid-Structure Coupling Including Thermoviscous Effects', *Acta Acustica united with Acustica*, vol. 102, no. 3, pp. 517–529, May 2016, doi: 10.3813/AAA.918969.
- [83] M. Nijhof, 'Viscothermal wave propagation', PhD, University of Twente, Enschede, The Netherlands, 2010.
- [84] F. B. Daniels, 'Acoustical Impedance of Enclosures', *The Journal of the Acoustical Society of America*, vol. 19, no. 4, pp. 569–571, Jul. 1947, doi: 10.1121/1.1916522.
- [85] M. Bruneau, *Fundamentals of acoustics*. London ; Newport Beach, CA: ISTE Ltd, 2006.
- [86] 'Analog Devices - ADA4817 - Datasheet' . .
- [87] 'Analog Devices - AD8429 - Datasheet' . .

# *List of acronyms*

<b>AI</b>	Artificial Intelligence
<b>AOP</b>	Acoustic Overload Point
<b>AVATRAM</b>	Air-to-Vacuum Transmission Mechanism
<b>BOX</b>	Buried Oxide
<b>BV</b>	Back Volume
<b>BW</b>	Bandwidth
<b>CMP</b>	Chemical Mechanical Planarization
<b>DR</b>	Dynamic Range
<b>DRIE</b>	Deep Reactive Ion Etching
<b>ECM</b>	Electret Condenser Microphone
<b>EIN</b>	Equivalent Input Noise
<b>FEM</b>	Finite Elements Model
<b>IOT</b>	Internet Of Things
<b>MEMS</b>	Micro-Electromechanical System
<b>OPS</b>	Out-of-Plane Spring
<b>ROEC</b>	Readout Electronic Circuit
<b>SNR</b>	Signal-to-Noise Ratio
<b>SOI</b>	Silicon On Insulator
<b>SPL</b>	Sound Pressure Level
<b>THD</b>	Total Harmonic Distortion



# Résumé

## Chapitre 1 : Introduction

Récemment, les microphones **MEMS** (microsystèmes électromécaniques) sont devenus des composants essentiels dans un large éventail d'appareils électroniques grand public. La demande de microphones à hautes performances a été propulsée d'une part par la nécessité d'améliorer des champs d'applications existants, comme la prise de voix pour les appels téléphoniques, et d'autre part par le développement de nouvelles applications, comme l'adoption massive des systèmes de reconnaissance vocale. Cette demande constante de meilleures performances a poussé l'optimisation de la technologie actuelle à ses limites, vu que la majorité des microphones **MEMS** du commerce est basée sur des variantes de design d'un simple condensateur : une membrane déformable, face à une contre-électrode trouée et fixe, et posée sur une cavité maintenue à pression atmosphérique communément appelée Back Volume (**BV**). Dans ce design, la transduction capacitive est effectuée à pression ambiante, ce qui inévitablement mène à des amortissements de compression et à une résistance acoustique à cause de la présence de la contre-électrode. Ces pertes visqueuses deviennent les sources prépondérantes de bruit, limitant le rapport signal sur bruit (**SNR**) du microphone. Représentatif du niveau de performance global, le **SNR** des microphones basés sur ce design ne peut alors être amélioré qu'au prix d'une plus grande taille de puce et de **BV**. Bien que d'autres changements et améliorations de design aient été proposés, les efforts pour améliorer le **SNR** sans augmenter la taille du composant n'ont pas abouti. Par ailleurs, les designs basés sur la transduction piézoélectrique semblent prometteurs comme alternative, puisqu'ils ne requièrent pas de contre-électrode. Cependant, l'amélioration de leur performance se trouve rapidement limitée par les pertes intrinsèques des matériaux piézoélectriques actuellement disponibles.

Pour réduire les pertes visqueuses et améliorer le niveau de performances des microphones **MEMS** capacitifs, le présent travail de recherche propose une nouvelle approche qui consiste à séparer la contre-électrode de la membrane et à effectuer la transduction dans le vide. Avec ce nouveau design, le capteur est divisé en deux parties : un piston rigide qui récolte la pression acoustique dans l'air, connecté mécaniquement à un transducteur capacitif encapsulé dans une cavité sous vide. Cette séparation mène à une réduction drastique des sources de bruits acoustiques tout en permettant une grande densité capacitive, ce qui améliore nettement le **SNR** du microphone sans nécessairement augmenter sa taille. Une charnière innovante (air-to-vacuum hinge), capable de transférer un déplacement mécanique entre deux atmosphères distinctes, assure la connexion mécanique entre les éléments tout en maintenant l'étanchéité de la cavité sous vide (**Figure 1**). Dans

cette étude, la charnière mécanique est d'abord dimensionnée pour qu'elle soit suffisamment robuste pour soutenir les effets de la pression atmosphérique et de potentiels pics de pression, tout en restant suffisamment flexible afin de transférer le mouvement mécanique. Un modèle analytique du microphone est ensuite développé, détaillant son fonctionnement théorique, et les niveaux de performances atteignables et les limitations en termes de taille sont discutés. Les designs des microphones finaux sont basés sur le cadre théorique du modèle analytique et prennent en compte les dimensions critiques déterminées par le processus de fabrication à deux wafers. Enfin, les résultats de la fabrication des microphones sont étudiés, et les composants sont caractérisés électriquement et acoustiquement sur wafer.

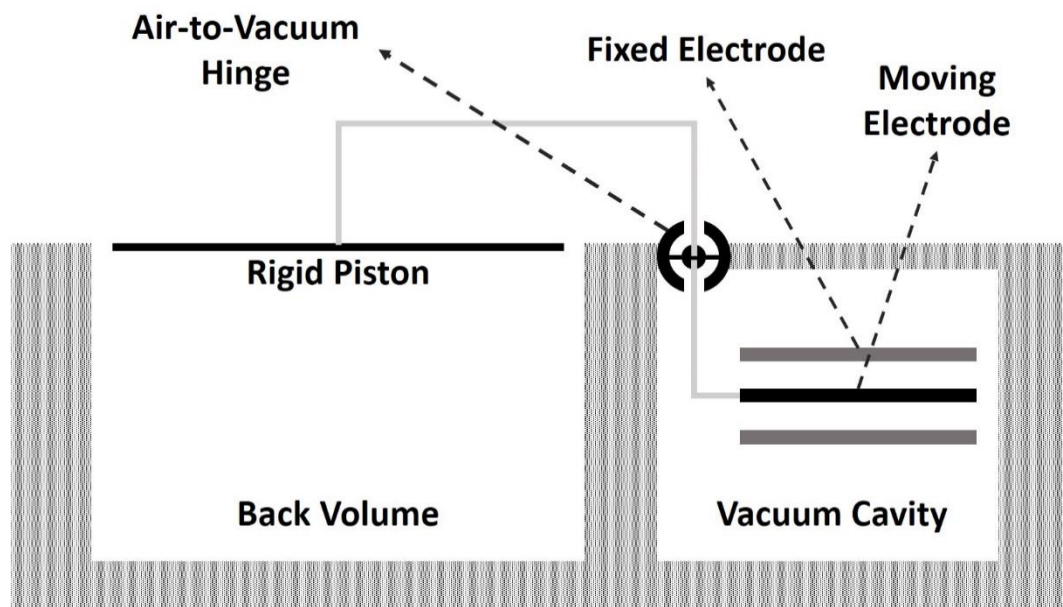
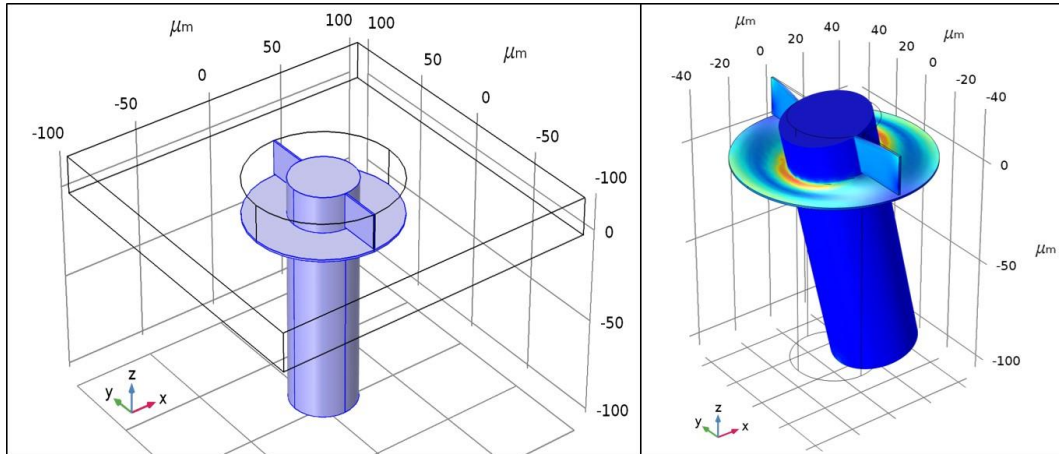


Figure 1: Schéma simplifié du nouveau concept de microphone à détection capacitive dans le vide.

## Chapitre 2 : Modèle du microphone

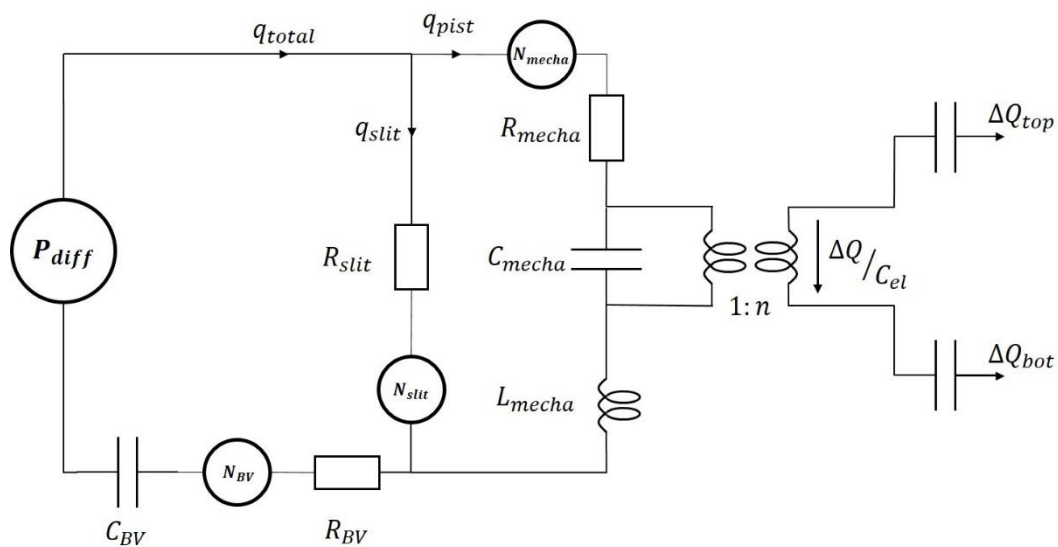
La transmission de la force d'une atmosphère à l'autre, l'idée centrale autour de laquelle est bâti ce nouveau concept de microphone, impose des besoins exigeants et contradictoires au design de la charnière. Cette dernière est alors conçue de telle sorte qu'elle assure l'étanchéité de la cavité, qu'elle soit suffisamment robuste pour soutenir les effets de la pression ambiante et de potentiels pics de pression, tout en restant suffisamment flexible pour transférer le mouvement mécanique. Pour répondre à ces exigences, la charnière est composée d'un pilier cylindrique et rigide, placé entre l'air ambiant et la cavité sous vide. Une plaque mince encercle le pilier et forme un joint étanche et flexible entre les deux atmosphères. Enfin, du côté de la cavité, le pilier est tenu par deux barres de torsion. D'une part, leur épaisseur fournit une grande raideur en flexion, réduisant drastiquement le déplacement hors-plan du pilier. D'autre part, leur petite largeur offre une faible raideur en torsion, ce qui permet de transférer la force par la rotation

du pilier, malgré la limitation de son mouvement hors-plan. Une première étude basée sur la théorie des plaques de Timoshenko permet de définir les critères de robustesse de la charnière. Ensuite, la symétrie de la structure permet l'élaboration d'un simple modèle mécanique donnant la raideur totale de la structure. A partir de ce modèle, les différentes parties de l'articulation sont alors dimensionnées par une série de modélisations par éléments finis, de manière à ce que la charnière réponde à toutes les exigences initiales (**Figure 2**).



**Figure 2: Schéma 3D de la charnière (gauche), et modèle à éléments finis montrant la déformation de la structure en rotation (droite).**

Une fois le design de la charnière défini, un modèle à constantes localisées peut être développé, afin de décrire le fonctionnement et les propriétés du microphone. Le modèle, dont le circuit équivalent est représenté dans la **figure 3**, permet d'évaluer tous les paramètres de performance principaux du microphone : la sensibilité, fréquence de coupure, la fréquence de résonance, et le bruit. Trois sources principales de bruits sont alors identifiées dans le système :  $N_{slit}$  due à la résistance des événements tout autour du périmètre du piston,  $N_{mecha}$  due à la résistance visqueuse



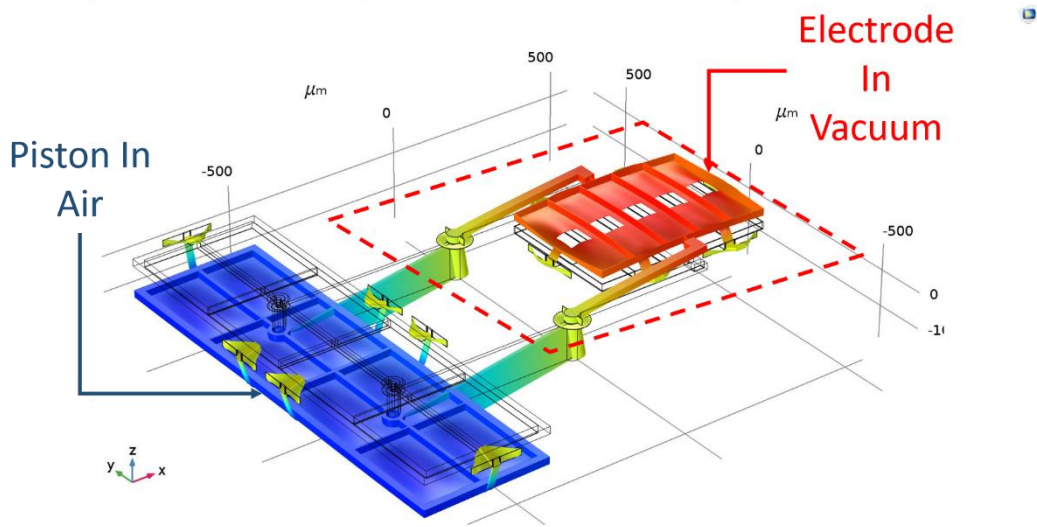
**Figure 3: Circuit équivalent du modèle à constantes localisées du microphone.**

causé par le mouvement du piston, et  $N_{BV}$  due à la dissipation thermique sur les parois du **BV**. En prenant en compte les géométries et dimensions permises par le processus de fabrication, l'étude des sources de bruits montre qu'un **SNR** acoustique au-delà de  $75 \text{ dB}(A)$  est atteignable, prouvant l'intérêt de ce nouveau concept.

### Chapitre 3 : Design et fabrication du microphone

Le processus de fabrication choisi pour ce microphone est le Process M&NEMS, développé à maturité et effectué par le CEA-Leti. Ce processus à deux wafers permet la présence de différentes couches relativement fines et épaisses dans le même composant, offrant une grande flexibilité en terme de design. De plus, il rend possible la juxtaposition de parties encapsulées et d'autres parties exposées à l'air ambiant, crucial pour ce nouveau concept. Ajoutant qu'elle partage de grandes similarités avec des processus industriels bien connus, cette méthode de fabrication présente tous les éléments nécessaires pour réaliser ce nouveau microphone et atteindre les objectifs fixés en termes d'industrialisation potentielle.

Par ailleurs, le processus de fabrication non seulement définit les possibilités de conception pour les différents éléments du dispositif, mais affecte également plusieurs paramètres de performance du microphone en fixant les géométries et dimensions permises. Avec ces limites, certains degrés de liberté mineurs sont supprimés et la chaîne reliant tous les paramètres de performance de l'appareil peut être démêlée. Etant donné que le but principal de ce nouveau concept de microphone est d'améliorer les performances, une méthode de design axée sur les niveaux de performance a été développée et adoptée. Cette méthode consiste à déterminer d'abord les niveaux de performances visés, à partir desquels un premier dimensionnement grossier des différentes parties peut être défini. Chaque partie de la structure est ensuite séparément dimensionnée. Enfin, les différentes parties sont assemblées, et la réponse mécanique de la structure finale est simulée pour s'assurer qu'elle est correcte. Plusieurs variantes de designs ont été conçues, afin d'explorer le potentiel de ce nouveau concept. La **figure 4** montre un exemple de design dans lequel le piston, connecté à deux charnières, a un mouvement strictement hors plan. Les charnières transmettent alors ce déplacement à une électrode dans le vide qui bouge entre deux contre-électrodes, assurant une lecture différentielle. Comme pour le piston, le mouvement de l'électrode est aussi strictement hors plan.

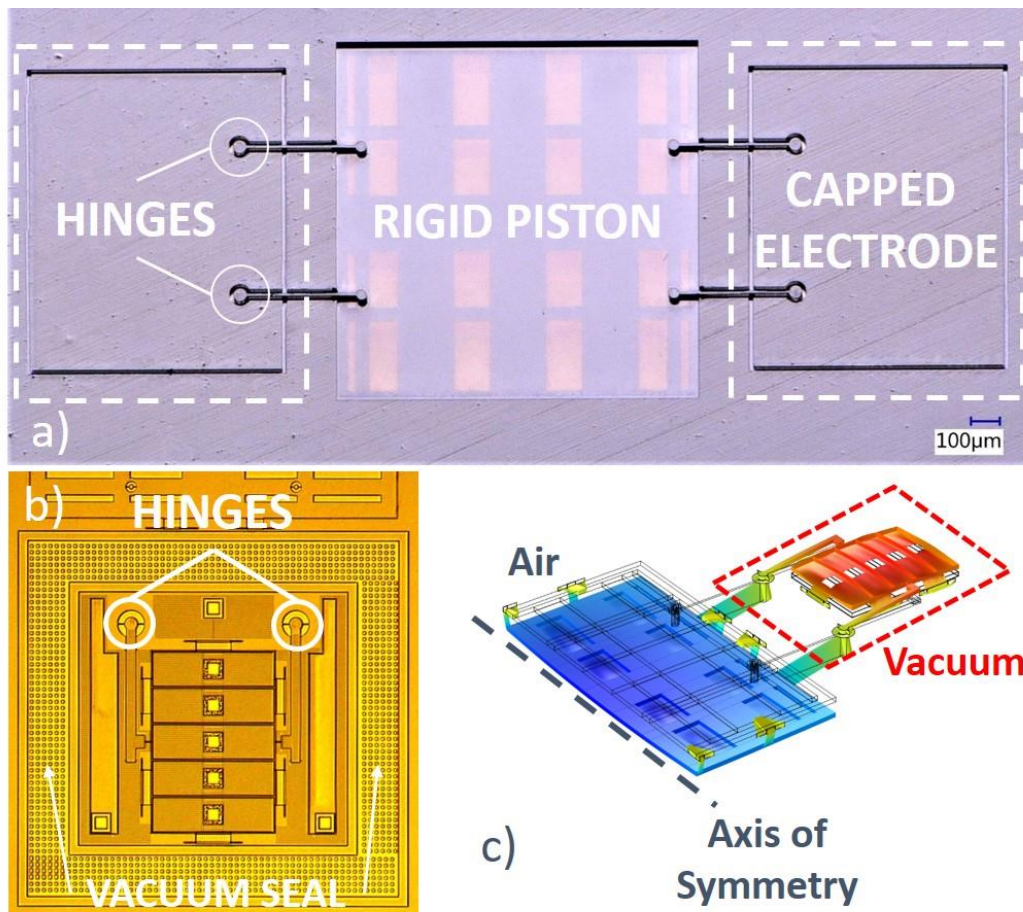


**Figure 4: Résultat d'une simulation montrant le déplacement attendu des pièces mobiles de la structure mécanique d'un design de microphone.**

## Chapitre 4 : Résultats et discussion

Les microphones ont été fabriqués avec succès, malgré plusieurs problèmes rencontrés durant la fabrication. Ces problèmes et leurs causes ont été analysés et corrigés, et de nouvelles plaques sont actuellement en cours de fabrication avec les corrections apportées. Ensuite, pour caractériser les 693 microphones sur chaque wafer, une série de tests automatiques (électriques et acoustiques) a d'abord été effectuée. Ces premiers tests permettent de trier les composants afin de retrouver les meilleurs candidats pour des tests approfondis. La **figure 5** présente un exemple de microphone réalisé, pour lequel le piston rigide est placé au centre. Quatre charnières transmettent le mouvement hors-plan du piston à deux électrodes latérales encapsulées dans des cavités sous vide différentes. Chaque électrode a aussi un mouvement strictement hors-plan et bouge entre deux contre-électrodes pour la lecture différentielle.

Pour tester sa réponse, le microphone a été polarisé par une tension DC tandis qu'un haut-parleur placé devant le wafer était balayé en fréquence dans la plage audible. En même temps, le déplacement hors-plan du piston a été mesuré par

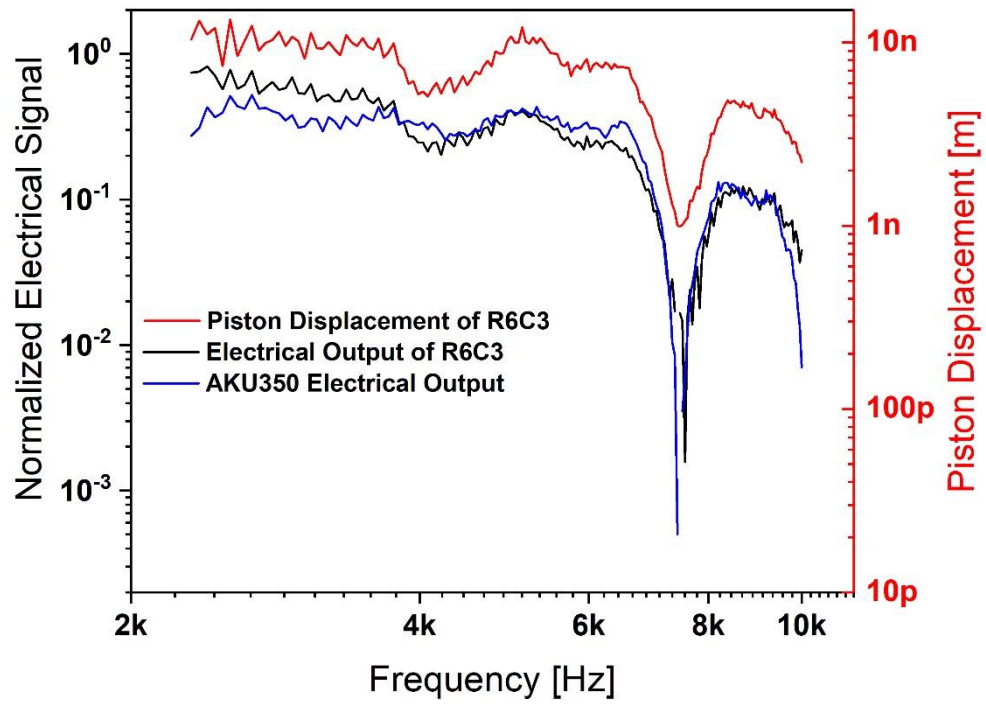


**Figure 5: Images de microscopie optique du côté air (a) et d'une électrode non encapsulée (b). Résultat d'une simulation montrant le déplacement attendu des pièces mobiles de la structure mécanique (c). L'échelle de la déformation a été augmentée et seule la moitié de la structure symétrique est représentée pour plus de clarté.**

interférométrie laser, alors que la sortie différentielle du microphone était démodulée à la fréquence d'actionnement. Malgré le fait que la fonction de transfert du haut-parleur ne soit pas plate, mis en évidence par la réponse d'un microphone du commerce, les résultats prouvent le bon fonctionnement du microphone : le signal électrique est en très bon accord avec la réponse du microphone du commerce et suit exactement le mouvement du piston en fonction de la fréquence acoustique (**Figure 6**). Avec une sensibilité mesurée à  $6 \pm 0.5 fF/Pa$ , ces premiers résultats sont extrêmement prometteurs, marquant une première preuve de concept de ce nouveau design de microphone.

Pour conclure, cette étude présente le développement et l'implémentation d'un nouveau concept de microphones MEMS avec pour but l'amélioration des niveaux de performance. Suite au développement des modèles analytiques et numériques, les premiers tests sur les microphones prouvent la viabilité de ce nouveau design. Avec cette première preuve de concept, ce design ouvre la voie aux microphones MEMS à ultra-hautes performances.





**Figure 6:** Graph montrant le signal électrique et le déplacement du piston d'un nouveau microphone ainsi que le signal de sortie d'un microphone du commerce sous la même excitation acoustique. Les signaux électriques sont normalisés car l'AKU350 possède un circuit électronique d'amplification interne.





**Titre :** Design d'un microphone MEMS basé sur une nouvelle architecture.....

**Mots clés :** Microphone, MEMS, Capacitif, Vide

**Résumé :** Pour réduire les pertes visqueuses et améliorer le niveau de performances des microphones MEMS capacitifs, le présent travail de recherche propose une nouvelle approche qui consiste à séparer la contre-électrode de la membrane et à effectuer la transduction dans le vide. Avec ce nouveau design, le capteur est divisé en deux parties : un piston rigide qui récolte la pression acoustique dans l'air, connecté mécaniquement à un transducteur capacitif encapsulé dans une cavité sous vide. Cette séparation mène à une réduction drastique des sources de bruits acoustiques tout en permettant une grande densité capacitive, ce qui améliore nettement le SNR du microphone sans nécessairement augmenter sa taille. La connexion mécanique entre les éléments est assurée par une charnière innovante, capable de transférer un déplacement mécanique entre deux atmosphères distinctes. Dans cette étude, la charnière mécanique est d'abord dimensionnée pour qu'elle soit suffisamment robuste pour soutenir les effets de la pression atmosphérique et de potentiels pics de pression, tout en restant suffisamment flexible afin de transférer le mouvement mécanique

Un modèle analytique du microphone est ensuite développé, détaillant son fonctionnement théorique, et les niveaux de performances atteignables et les limitations en termes de taille sont discutés. Les designs des microphones finaux sont basés sur le cadre théorique du modèle analytique tout en prenant en compte les dimensions critiques déterminées par le processus de fabrication à deux wafers. La fabrication de ces microphones a été réalisée avec succès, et les problèmes rencontrés ont été analysés et corrigés. De plus, les premiers résultats expérimentaux sur wafer prouvent la viabilité de ce nouveau concept. Le transfert du mouvement du piston dans l'air au transducteur encapsulé a été démontré, et la réponse acoustique des microphones a été mesurée avec succès avec une sensibilité qui atteint  $6 \pm 0.5 \text{ fF/Pa}$ . Avec cette première preuve de concept, ce nouveau design ouvre la voie aux microphones MEMS à ultra-hautes performances.

**Title :** Design of a MEMS microphone based on a new device architecture.....

**Keywords :** Microphone, MEMS, Capacitive, Vacuum

**Abstract :** This present work proposes a new approach for reducing the viscous damping losses, and improving the performance of capacitive MEMS microphones, by separating the backplate from the membrane and performing the transduction in vacuum. In this new design, the device is separated into two parts: a rigid piston that harvests the acoustic sound pressure in air, mechanically connected to a capacitive transducer encapsulated in a vacuum cavity. This separation drastically reduces the acoustic noise sources in the device and allows a high capacitive density, which significantly improves the SNR of the microphone without necessarily increasing its size. The connection between both elements is ensured by an innovative mechanical hinge, capable of transferring a mechanical motion between two separate atmospheres. In this study, the mechanical hinge is first designed to be robust enough to withstand the effects of atmospheric pressure and

possible high pressure overshoots, while remaining. An analytical model of the microphone is then developed, detailing the theory of operation of the device, and the achievable performance levels and size limitations are discussed. The final devices are designed based on the theoretical framework of the analytical model, taking into account the critical dimensions set by the two-wafer fabrication process. These devices have been successfully fabricated, and the encountered fabrication problems have been analyzed and corrected. Furthermore, the first wafer-level experimental results prove the viability of this new device concept. The transfer of the force from the piston in air to the encapsulated transducer was proven, and the acoustic response of the devices was successfully measured with a sensitivity reaching  $6 \pm 0.5 \text{ fF/Pa}$ . With this first proof of concept, this new design paves the way for ultra-high performance MEMS microphones.